Title	Visualization and quantification of HIV associated lipodystrophy from magnetic resonance images
Authors(s)	O'Sullivan, Tadhg
Publication date	2012
Publisher	University College Dublin. School of Medicine and Medical Science
Link to online version	http://dissertations.umi.com/ucd:10052
Item record/more information	http://hdl.handle.net/10197/6838

Visualization and Quantification of HIV Associated Lipodystrophy from Magnetic Resonance Images

Tadhg O'Sullivan, B.A., B.Sc.

The thesis is submitted to University College Dublin in fulfilment of the requirements for the degree of Doctor of Philosophy in the College of Health Sciences

School of Medicine and Medical Sciences

Head of School: Prof. William Powderly

Principal Supervisor: Dr. Louise Rainford

January 2012

Abstract

Purpose

This research aimed at developing a software tool for the purposes of quantifying and visualizing HIV-associated lipodystrophy from full body magnetic resonance imaging (MRI) datasets. The primary goal for developing the software tool was to create and compare the results gathered from MRI to those from the current gold standard, dual-energy X-ray absorptiometry (DEXA). A software based solution for this purpose is proposed and a full evaluation with the intention of future clinical use is presented. The additional aim of volume visualization in order to assess the external morphological effects of HIV-associated lipodystrophy is also presented.

Methods

The data gathered for this study involved a cohort of HIV positive cases (n = 8) which were recruited in order to be scanned by both Dual Energy X-ray Absorptiometry (DEXA) and MRI techniques to facilitate comparison between the two modalities.

The accurate identification and segmentation of adipose tissue from MRI datasets was identified as one the key components of this piece of research. A fully automatic segmentation algorithm was implemented for this purpose. Quantification of segmented adipose tissue and surface based volume visualization were implemented as the primary features of the software tool.

The fully automatic segmentation algorithm was investigated in regards to accuracy and performance. In order to evaluate the clinical relevance of the results of segmentation, a comparison of the results to those of the current gold standard (DEXA) was performed. Clinical feedback regarding the usefulness of the software tool in a clinical setting is also presented.

Visualization of adipose distribution and external morphology from full body data were also identified as an important component of this project. A surface based volume

visualization technique was implemented in order to allow users to view a patient's external morphology. Application of a heat map to the surface in order to intuitively visualize the distribution of adipose tissue was also implemented.

Results

The findings of this study indicate that the results gathered by the software tool developed compared well to those of the current gold standard. A strong correlation between the results of the two modalities was found with a correlation coefficient r of 0.68 and significance level of $p < 0.0001$ with a very small 95% confidence interval. A reasonable level of agreement between the modalities was also recorded, the mean difference in fat measurements between the two was 5.62%. A panel of MR experts, Radiology (n = 2), MSc MRI Radiography Specialists (n = 3), PhD Medical Imaging MRI Specialists (n = 2) evaluated the segmentation technique used and it was found to be accurate and, due to the fact it was automatic, its results were 100% reproducible.

Conclusions

In this study the segmentation, quantification and visualization of adipose tissue from full body MRI dataset in place of the current gold standards was targeted and investigated.
A proof of concept software tool was developed for this purpose and was evaluated for accuracy and clinical relevance. The findings presented provide the evidence base that an appropriate tool was developed and could be used with MRI as an alternative to DEXA examination.

STATEMENT OF ORIGINAL AUTHORSHIP

I hereby certify that the submitted work is my own work, was completed while registered as a candidate for the degree stated on the Title Page, and I have not obtained a degree elsewhere on the basis of the research presented in this submitted work.

Signed: _____

Tadhg O'Sullivan

Acknowledgements

Primarily, I would like to extend my thanks and gratitude to my supervisors, Dr. Louise Rainford and Dr. John Ryan, for their invaluable knowledge, guidance and support during the course of this work. I would also like to extend my thanks to the rest of my colleagues in the Diagnostic Imaging department in UCD.

I would specifically like to thank Owen Grogan, Barry Denby, Dr. Gergely Zombori, Brian Macarthy and Dr. Ben Donlon for their help during this study.

I gratefully acknowledge funding from both the UCD School of Medicine and Medical Science and Science Foundation Ireland.

Finally, thank you to my friends and family for supporting me over the last three and a half years.

Contents

Figures

Tables

Related Work by Author

2011 Oct	**Visualization in Medicine and Life Sciences II, Springer Book**
Book Chapter:	"Automatic Segmentation and Visualization from Magnetic Resonance Datasets"
2011 Aug	**MIPS Annual Conference, Dublin, Ireland**
Plenary talk:	"An Evaluation of Automatic Segmentation of Adipose Tissue from Full Body Magnetic Resonance Datasets"
2010 Jul	**Visualization in Medicine and Life Sciences 2010, Bremerhaven, Germany**
Plenary talk:	"Visualization and Quantification of HIV-associated Lipodystrophy"
2009 Dec	**RSNA Annual Conference, Chicago, USA**
Digital poster:	"Automatic Segmentation and Visualization from Magnetic Resonance Datasets"
2009 Jun	**Biological Imaging Symposium, UCD School of Medicine, Dublin, Ireland**
Plenary talk:	"Segmentation of Magnetic Resonance Images"

Glossary

mmol: Millimole. The mole is a unit of measurement used in chemistry to express amounts of a chemical substance, defined as an amount of a substance that contains as many elementary entities (e.g., atoms, molecules, ions, electrons).

Isosurface: An isosurface is a surface mesh made of polygons that is drawn in the volume

Pixel: A single unit of a 2D image, typically represented by colour/intensity (usually three values, red, green and blue) and transparency information.

Polygon: A closed plane shape with three or more sides

Sagittal Plane: This describes the plane that is perpendicular to the coronal plane and cuts the body straight down the middle.

Transverse Plane: this plane is parallel to the xz axis.

Voxel: A single unit of a volume, the 3D version of the 2D pixel

Coronal Plane: Also called the frontal plane, is a vertical plane which divides the body into ventral and dorsal.

1 Introduction

1.1 Motivation

The introduction of highly active antiretroviral treatments (HAART) for HIV, while leading to a reduction of mortality levels among patients, has also been associated with an increase in long-term side effects such as HIV-associated Lipodystrophy (HIVLD) [1]. HIVLD is characterised by peripheral lipoatrophy, central adiposity, dyslipidaemia, insulin resistance and an increased risk of premature cardiovascular disease. Besides affecting the quality of life of patients, specifically patient morale due to unwanted changes in their external morphology, HIVLD can also affect adherence to the treatment of HIV. This can in turn lead to increased rates of virological resistance and disease progression [2].

At present, the imaging modality most commonly used to assess the distribution of adipose tissue within the body is Dual Energy X-ray Absorptiometry (DEXA). There are two primary limitations associated with this modality. Namely that DEXA produces 2D images from whole body scans from which an estimate of peripheral fat can be calculated and it cannot give specific information regarding central fat, which is associated with insulin resistance and diabetes. The second limitation is the availability and variety of DEXA. At present there is one research centre (dedicated to HIV patients) with a DEXA in Dublin, Ireland, compared with the availability of 40 Magnetic Resonance Imaging (MRI) scanners in numerous medical establishments. DEXA scanners are available across hospitals nationally but these are not used for the specific purpose of adipose tissue quantification. Patients attending with other medical issues such as for osteoporosis diagnosis have the potential to reduce the standardisation of HIV patient imaging protocols across centres which can be further affected as different vendors use different methods to quantify fat [3].

This research, which took place between September 2008 and January 2012, aims to enhance patient management through the development of a clinically validated software tool which can accurately segment, quantify and visualise HIVLD from MRI datasets.

1.2 Objectives

The overall objective of this research was to develop a software tool for use in the assessment of patients presenting with/ or at risk of developing HIV-associated lipodystrophy.

In order to achieve this, a number of objectives were identified:

- *Implementation of an optimal soft-tissue segmentation algorithm for magnetic resonance imaging datasets specific to this disease model.*
- *Enhanced volume and iso-surface visualisation techniques relevant to the imaging of the side-effects of anti-retroviral treatment.*
- *Development of clinically-relevant metrics to quantify lipodystrophy specific to HIV anti-retroviral treatment.*
- *Validation of segmentation and visualisation techniques used in the software tool.*
- *Validation of the software tool in comparison to the current standard, DEXA.*

1.3 Novel Contributions

The culmination of this research led to a number of novel contributions:

- *The software tool as a whole is a novel contribution, offering users a fast, automatic and accurate method of quantifying adipose tissue from full body MRI datasets.*
- *The data gathered through this research has shown that MRI can be used in the same manner as DEXA for the purposes of monitoring HIV-associated lipodystrphy without the use of ionizing radiation.*
- *The 3D visualization has presented the distribution of adipose tissue throughout the body in an intuitive and novel manner.*

1.4 Summary of Chapters

This thesis is divided into chapters and their contents are now summarised:

Chapter 2 – Background covers the medical and technological principles relevant to this piece of research. These include an overview of HIV-associated lipodystrophy, medical imaging modalities, and image processing/segmentation and data visualisation techniques.

Chapter 3 – Application describes the graphical user interface (GUI) developed for this research. Focusing on the technologies used to develop the GUI, its relevant features and functionality.

Chapter 4 – Image Processing details the steps taken and algorithms used to process the MRI data (particularly intensity inhomogeneity correction and contrast enhancement). Describes in detail the segmentation algorithms applied to said data and process of quantifying the segmentation results.

Chapter 5 – Visualisation covers the technologies and algorithms used to visualise the data and the quantification results.

Chapter 6 – Clinical Trials and Evaluation describes the evaluation techniques which were used during the validation stage of this research. Additionally, the ethical considerations associated with the clinical trials are covered in this chapter.

Chapter 7 – Results details the results acquired from the evaluations employed and discusses their impact with respect to the aims of this piece of research.

Chapter 8 – Discussion of findings in Relation to Previous Studies details the findings of this study with regards to related studies. **Clinical Limitations** details the limitations associated with patient scanning and the resulting datasets discovered during the study period. **Conclusions and Future Work** finalises the findings of this piece of research and looks at its possible future applications and improvements.

1.5 Contributors and Collaborators

This research was made possible with the aid of the following contributors and collaborators; Science Foundation Ireland, University College Dublin, The Mater Misericordiae University Hospital and the Catherine McAuley Centre.

2 Background

2.1 HIV Associated Lipodystrophy

The human immunodeficiency virus (HIV) has a major impact upon a persons' health affecting millions of individuals worldwide. In 2007 the Joint United Nations Programme on HIV/AIDS (UNAIDS) reported that an estimated 33 million people were living with HIV [4]. Since the introduction of highly active antiretroviral treatments (HAART) in 1996 there has been a substantial decrease in the morbidity and mortality rates of HIV-infected patients [5]. HAART, which is now the standard treatment for HIV infection, involves the use of a combination of antiretroviral drugs with the aim of suppressing the replication of a virus within host cells. Antiretroviral drugs, such as nucleoside reverse transcriptase inhibitors (NRTI) or Protease inhibitors (PIs), attempt to interrupt specific stages of the life-cycle of a retrovirus [6, 7]. In the majority of cases, antiretroviral drugs will inhibit the activity of certain enzymes which are needed by a retrovirus in order for it to successfully replicate [8]. While it is without question that HIV-infected patients have benefitted from the use of HAART, there are also a number of adverse effects associated with this form of treatment.

In 1997 one such adverse effect was reported by the United States Food and Drug Administration (FDA). The FDA stated that a small number of HIV-infected patients, who were currently prescribed Protease Inhibitors, were presenting with hyperglycemia and type 2 diabetes [9]. Over the next few years there were increased reports of HIV-infected patients presenting with maldistribution of adipose tissue. The condition, known as lipodystrophy, is characterized by central adiposity, dorsocervical fat accumulation (also known as the 'Buffalo Hump'), and peripheral fat wasting (see Figure 2-1).

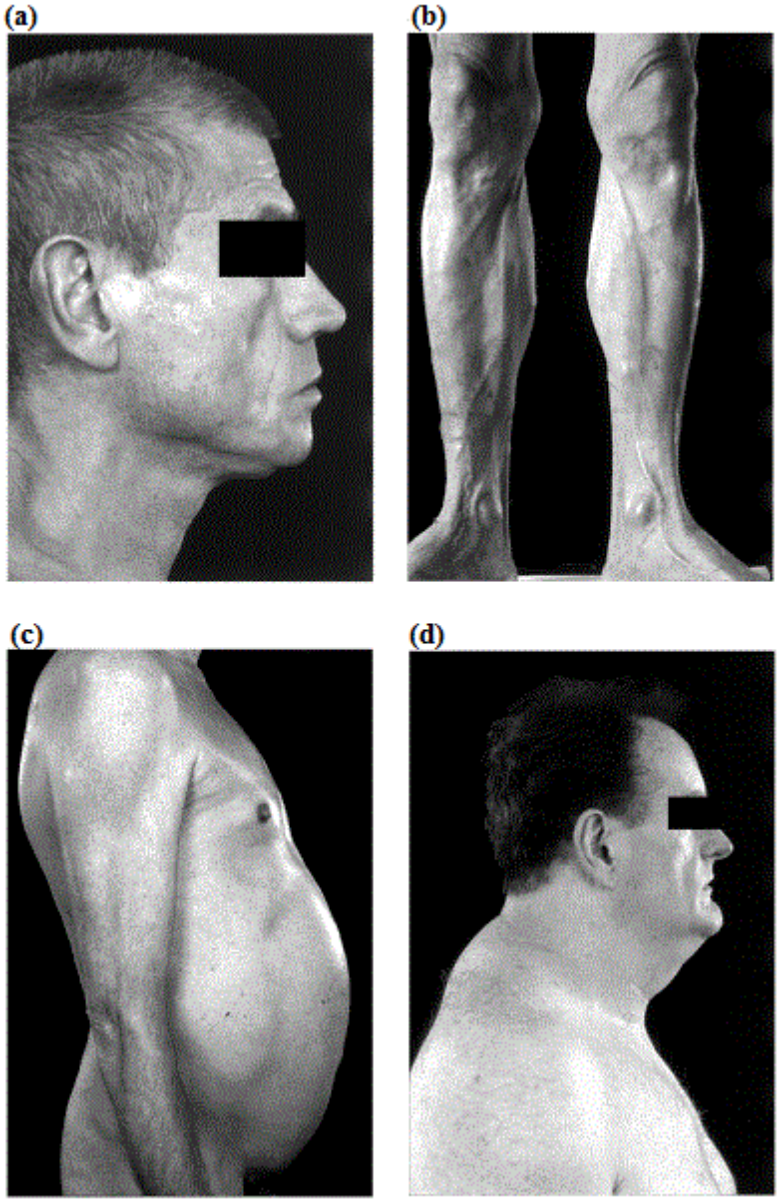

Figure 2-1 *Physical Characteristics of HIV-associated Lipodystrophy (a) facial lipoatrophy with loss of subcutaneous adipose tissue (SAT), (b) limb lipoatrophy showing loss of SAT from the limbs, (c) visceral fat accumulation evident in the abdomens and (d) fat accumulation in the dorsocervical region (upper back) also referred to as 'buffalo hump'* [10].

Besides the overt physical manifestations caused by the syndrome, there have also been a number of underlying medical conditions associated with HIV-associated lipodystrophy and the use of HAART. Dyslipidaemia, the presence of an abnormal amount of lipids found in the blood, at certain levels has been strongly correlated with an increased risk of cardiovascular

disease. It has been found that 32-54% of HIV patients receiving HAART have total cholesterol levels being greater than 6.2 mmol per litre (recommended levels should be below 3.3618 mmol) and that 16-22% present with high density lipoprotein cholesterol levels less than 0.9 mmol per litre (recommended levels should be greater then 1.0344 mmol). The exact cause of these unsafe lipid levels is not certain but there is evidence which suggests a direct link between dyslipidaemia and the use of protease inhibitors, HIV infection and lipodystrophy [11].

The development of insulin resistance has also identified in patients using HAART and presenting with HIV-associated lipodystrophy. It is believed that, along with the use of protease inhibitors, the increase of visceral adipose tissue (VAT) in the abdomen and dorsocervical region and the decrease in subcutaneous adipose tissue (SAT) caused by peripheral fat wasting both correlate with insulin resistance. Insulin resistance causes an increase in blood sugar levels and can eventually lead to patients developing type 2 diabetes [10] [12].

The increased risk of premature cardiovascular disease is a primary concern with individuals presenting with HIV-associated lipodystrophy. Both insulin resistance and dyslipidaemia greatly increase the risk of a patient developing cardiovascular disease [12, 13]. While HAART has been strongly correlated with the onset of HIV-associated lipodystrophy and the underlying medical conditions associated with it, there are also a number of other factors which play an important role. A patient's age, sex and the duration of HIV infection have also been linked to the incidence of HIV-associated lipodystrophy [12].

Studies have found that more than 50% of patients receiving HAART will develop lipodystrophy [14]. The numerous medial conditions associated with lipodystrophy are becoming problematic with respect to successful patient management for many HIV-infected patients using antiretroviral drug treatments. The development of tools to accurately visualize and quantify the body's adipose tissue would aid clinicians in accurate monitoring of the condition so patient management decisions can be based upon quantifiable fat level depositions.

2.1.1 Previous Work

To date, only one study has been found which strongly relates to this piece of research. The paper, "*Comparison of DXA and MRI-measured adipose tissue depots in HIV-infected and*

control subjects", was published in The American Journal of Clinical Nutrition in October of 2008 and made available online through PubMed Central [15] on August 16th 2011. The study compared DEXA and MRI measurements of leg, arm, trunk and total of fat in HIV+ and control subjects. A cohort of 877 HIV+ cases and 260 control cases was gathered from 16 HIV or infectious disease clinics in the United States. The researchers used a third party software tool (TomoVision's sliceOmatic) to segment the MRI datasets. Specifics as to how the segmentation was performed or the accuracy of the segmentation were not presented in the study. The findings of the study indicated a strong correlation between DEXA and MRI measurements of fat but that there were also important biases with the two modalities. The primary biases were that DEXA generally estimates higher amounts of fat in the limbs then MRI and that as patient weight increases the difference in measurements between DEXA and MRI also increase. The main conclusion of the study is that, with the appropriate guidelines, DEXA is an adequate modality for measuring fat and that DEXA and MRI measurements of fat can vary depending upon certain circumstances [16]. A number of notable differences in the methodologies and aims between the study described and the current research study were identified. Average patient weight, slice axis of MRI datasets, segmentation techniques and the use, or lack thereof, of volume visualization were all significantly different in the previous research. Past research was a national study aimed at comparing the use of DEXA and MRI in quantification of fat whilst this study was principally aimed at developing a proof of concept software tool, fully automated in design for quantification and visualization of adipose tissue from MRI. It is important to note therefore that the clinical validation of the software involved a small patient cohort in comparison to the research by Scherzer et al. More detail as to some of the differences between the two studies are discussed in Chapter 8.

2.2 Imaging Modalities

To date the two most common imaging modalities used for the diagnosis and monitoring of HIV-associated lipodystrophy are Dual energy X-ray absorptiometry (DEXA) and Computed tomography (CT).

2.2.1 Dual Energy X-ray Absorptiometry

Dual energy X-ray absorptiometry (DEXA) is an imaging modality which was initially used for the detection of osteoporosis by measuring bone density (at specific sites within the body, e.g. lumbar spine or hip). As the technology associated with the modality has advanced it has also become widely used to perform whole body scans and can be used to obtain estimates of three separate body components. These components consist of bone mineral density (BMD), fat mass (adipose tissue) and fat-free mass (lean tissue). The primary components of a DEXA scanner are the detector, the X-ray tube and the K-edge filter. The tube and filter generate X-rays at two separate energy peaks. Different body components will attenuate the individual X-rays to different degrees. This allows the software system in a DEXA machine to differentiate between bone mineral and soft tissue and to then further differentiate the soft tissue to fat mass and fat-free mass. This is achieved due to the fact that the initial energy of each of the X-rays is known and the resulting energy levels after attenuation is collected by the detector. Previous studies have determined the level of attenuation of various tissues within the body and by using this information equations can be applied to estimate the amount of fat and fat-free mass for each pixel associated with the scan [3].

One of the interesting features of DEXA whole body scans is that the software provides the user with a very detailed description of the distribution of the three body components throughout the body. Separation of different regions (such as the arms, legs, trunk, pelvis, etc…) is achieved by a number of 'cut lines' which are drawn over the full body scan (see Figure 2-2). The position of each cut line can be changed by the user before calculating the body composition but this is not generally needed. Due to guidelines on patient position when scanning and certain features developed for the machines, the cut lines will usually be in the correct locations. A more detailed description of the body composition results provided by DEXA machines can be found in section 4.7.

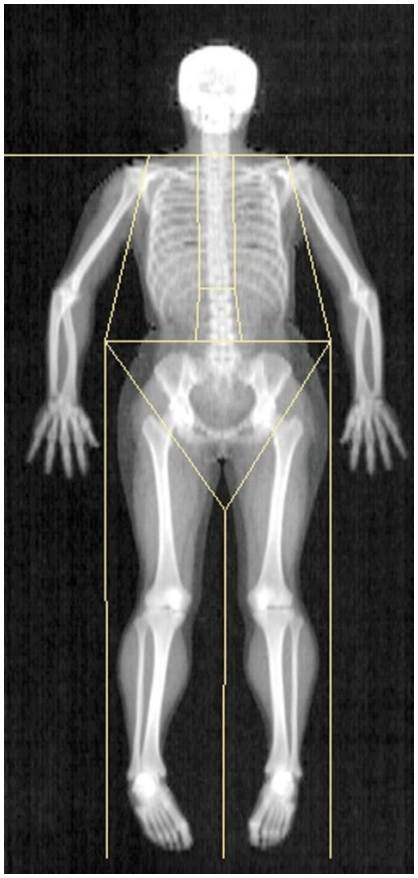

Figure 2-2 *An Example of a DEXA scan*

Two of the primary concerns related to the use of DEXA are its reproducibility and radiation dose [3] [17] [18]. Two specific issues arise with reproducibility in regards to DEXA. Firstly, it has been found that the body composition results can differ between DEXA manufacturers [3]. The difference in results has generally been attributed to different edge detection methods (detection of soft tissue near bone), differences in dual energy production or differences in the calibration for bone (i.e. whether the device includes or excludes intraosseous fat as part of bone). The reproducibility of an individual machine has been found to be quite accurate over the short-term. For whole body composition scans a coefficient of variation for determining full body mass was found to be less than 0.2% and that of whole body fat to be between 2-3%. Testing for long term reproducibility with patients is not feasible due to possible changes in body composition over time [19]. Radiation dose is the second concern related to the use of DEXA and can vary depending on the make or model of the machine used. A number of studies have taken place investigating the dose levels associated with DEXA and have found that the effective

dose from a scan can range between 1 and 20 µSv. With specific regards to this piece of research, which looks at the use of whole body scans, the average dose received by an adult (based on a phantom with a height of 174.0 cm and weight of 71.1 kg) the effective dose can range between 4.2 and 13.3 µSv. These values may be considered low when compared to natural background radiation (7 µSv) or a chest X-ray (20 µSv) but nonetheless should still be taken into consideration especially with regards to research where one may wish to perform imaging of individual patients over an extended period of time [17] [18]. As with any imaging modality, if radiation dose can be avoided it should be. This is one of the primary reasons for investigating whether Magnetic Resonance Imaging may be a valid alternative to DEXA with regards to the diagnosis and monitoring of HIV-associated Lipodystrophy.

2.2.2 Computed Tomography

The introduction of Computed Tomography (CT) by Godfrey Hounsfield (in 1968) was the first time that objects could be represented in a volumetric (3D) form and, in the field of medical imaging, is considered a major milestone. CT uses an emitter/detector system which rotates around an object acquiring a series of individual X-ray images (see [19]) which are used to create one volume dataset. There are a number of advantages when using CT compared to conventional X-ray or DEXA. One of the primary advantages, especially for diagnostic purposes, of CT is the ability to display the depth or location of anatomical structures within the object which has been scanned. CT is also up to two magnitudes more sensitive then X-ray creating images with much greater contrast between tissue types. This is especially important when trying to differentiate VAT and SAT from other tissues and organs within an image [20]. As stated previously with regards to the radiation dose associated with DEXA, if an alternative imaging modality which does not expose a patient to radiation is available and can provide the necessary information required then it should be the modality of choice. This is especially important if a patient will be required to undergo scanning over an extended period of time (i.e. monitoring the progression of a disease or for the purposes of research).

2.2.3 Magnetic Resonance Imaging

The imaging modality used for this research is magnetic resonance imaging (MRI). MRI is a clinical imaging tool which can trace its routes back to the discovery of the Nuclear Magnetic Resonance (NMR) phenomenon in the 1920's and 1930's. The NMR phenomenon showed that when certain atomic nuclei are placed within a magnetic field they will interact with said magnetic field. The affected nuclei are then exposed to radio waves of a particular frequency (the Larmor frequency). After this stimulation the nuclei will then release absorbed energy in the form of a radio signal and return to their original state. In the 1940's instruments for the measurement of this phenomenon where developed by Felix Bloch and Edward Purcell. Methods for creating tomographic images from the NMR phenomena were developed in the 1970's and by the 1980's MRI was established as core clinical tool for the diagnosis and monitoring of a number of medical conditions [21] [22].

MRI datasets were selected as the imaging modality most suitable for a quantification study investigating lipodystrophy rather than more conventional methods such as Dual energy X-ray absorptiometry (DEXA) or Computed tomography (CT). Firstly, the lack of ionizing radiation exposure with MRI is a particular advantage, especially if one wishes to acquire multiple datasets over an extended period of time. Secondly, MRI has shown to produce datasets with superior contrast between tissues in comparison with other imaging modalities. This increased contrast is especially noticeable with VAT and SAT [23, 24].

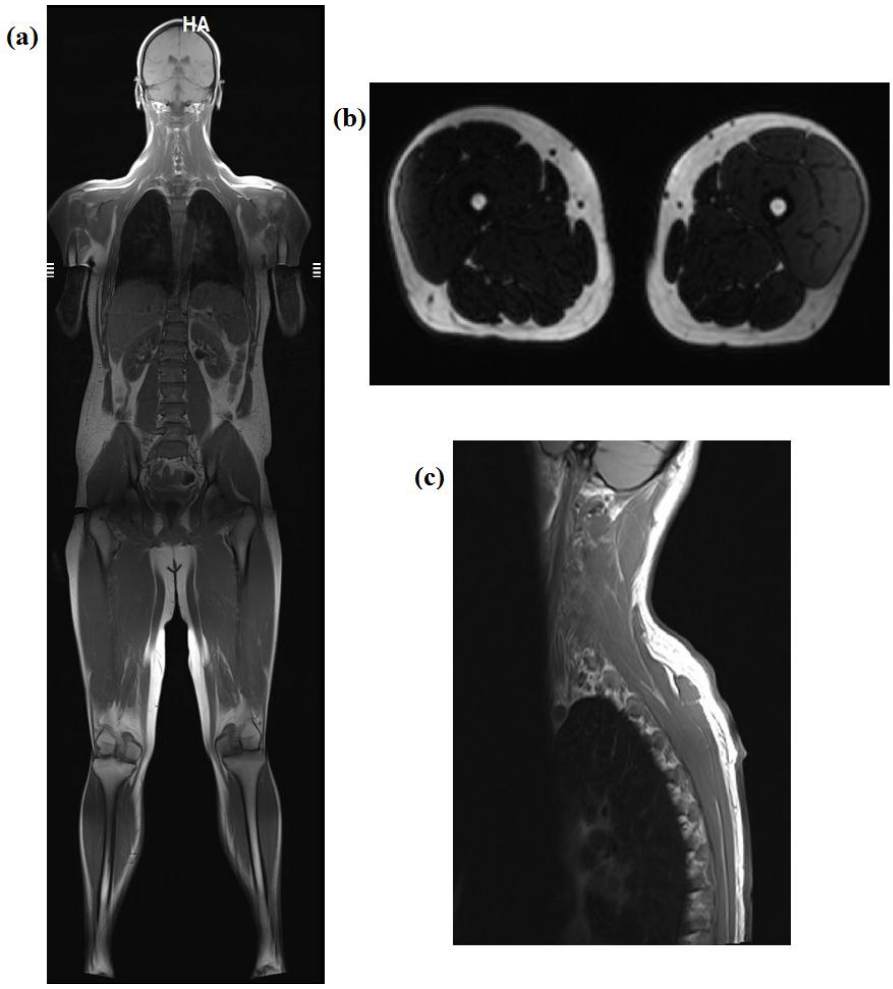

Figure 2-3 *2D T_1 weighted MRI axes examples: (a) Full body coronal scan. (b) Transverse scan of the upper leg. (c) Sagittal scan of the upper back*

2.2.3.1 Noise and Intensity Inhomogeneity

In order to accurately segment and quantify magnetic resonance imaging (MRI) data one must first deal with two inherent artefacts related to the acquisition process. To a human observer, noise is the most noticeable of these artefacts in MRI. Noise is generally modelled as having either a Rician distribution if there is a low signal-to-noise ratio (SNR) or a Gaussian distribution [25]. Rician noise is generally removed using wavelet-domain filtering while additive Gaussian noise can, in most cases, be easily detected and removed from the data using topological methods. In some cases, noise can also be removed by simple thresholding. This is due to the

fact that noise can have very low intensity values in comparison with objects of interest in an image. The generally accepted model for an acquired MRI image is:

$$v(x) = u(x) \times b(x) + n(x)$$

Where *v(x)* is the acquired image and *u(x)* is the optimal image free of intensity inhomogeneity and noise. The intensity inhomogeneity *b(x)* has a multiplicative effect over the image and the noise *n(x)* has an additive effect [26].

Intensity inhomogeneity (also known as the bias field or intensity nonuniformity) is a less noticeable artefact associated with MRI. Intensity inhomogeneity can be caused by a number of factors such as patient position within the MRI scanner, certain tissues which may be more or less susceptible to the magnetic frequency of the scanner or an inhomogeneity of the sensitivity of the radio frequency receiving and emitting coils. This artefact is generally perceived to be a smooth variation of signal intensities across an image. This can lead to homogenous tissues having widely varying intensities based on their location within the image (see Figure 2-4). While intensity inhomogeneity does not generally hamper visual diagnosis it does have a significant impact on automated image analysis methods, such as segmentation and visualization [26].

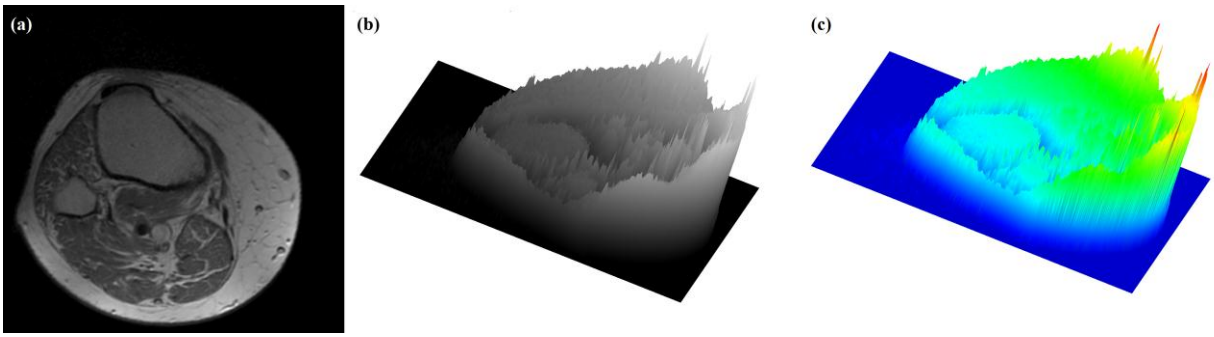

Figure 2-4 *Image inhomogeneity*

The effect of image inhomogeneity; (a) the original greyscale image, (b) a 3D heightmap of the data and (c) the same data with a RGB transfer function applied to it. The variation of intensities of adipose tissue (the highest intensity tissue in the greyscale image) can clearly be seen in all three images.

Numerous methods for the correction of intensity inhomogeneity and noise reduction in MRI have been proposed in the past [27]. Although accurate, many of these methods suffer from a high computational cost and a certain amount of human interaction. In subsequent sections the methods used in this work for fast automatic intensity inhomogeneity correction and noise reduction will be discussed.

2.2.3.2 Slice Gap and Slice Thickness

Two features of MRI which can effect both tissue segmentation and volume reconstruction are slice gap and slice thickness. Slice gap, measured in millimetres, is the distance between each slice within a volume. Slice thickness, also measured in millimetres, is the amount of tissue scanned in each individual slice. Both slice gap and thickness can negatively affect the accuracy of 3D segmentation (especially region growing algorithms). This is primarily due to the fact that the position of part of an object in one slice may not align with the rest of the object in adjacent slices. Slice thickness can also cause issues with regards to segmentation (especially intensity based segmentation methods in 2D). The chance of partial volume effect, a single voxel having a mixture of a number of different tissue intensities, increases as the slice thickness increases [28]. This can greatly decrease the accuracy of any segmentation technique which relies on tissue intensity values as one of its parameters. Slice gap and thickness must also be taken into account when rendering a number of slices from a MRI dataset in 3D. In order to represent the data correctly one must scale the data by the slice gap and thickness [29].

2.2.3.3 Scan Time

An important issue to take into account when acquiring MRI datasets is the time taken to complete scans versus the quality of the data. This is especially relevant in the case of full body datasets. The size of the slice gap and thickness will have an impact on the overall resolution and quality of a dataset. A balance with respect to diagnostic efficacy must be reached in the formation of imaging protocols for all imaging modalities. This was accounted for in the discussion of protocols in this study with MRI experts when preparing for ethical approval submission. Which axis is chosen for a MRI scan has a profound effect on the time needed to complete the scan. Issues such as claustrophobia will also often arise with patients undergoing

MRI scanning and therefore the general wellbeing of patients must be taken into consideration when deciding scanning protocols whilst ensuring the protocols are fit the for purpose at hand.

2.2.3.4 Magnetic Resonance Imaging and Adipose Quantification

Magnetic resonance imaging has been established as an effective modality for the quantification of adipose tissue. A number of studies have been performed in order to assess the accuracy and precision of MRI as a tool for quantifying total and regional adipose tissue. In order to compare MRI measurements against a 'Gold Standard', a common method of such comparison is against dissection of human cadavers. The measurements gathered by MRI of the cadavers are compared with direct weighing if adipose tissue from the dissected cadavers. Results have indicated a strong correlation between the two measurements with a mean difference between the two of 0.076kg (with a 95% confidence interval between 0.005kg and 0.247kg). These finding have justified the use of MRI for the purposes of adipose quantification and in recent years, there has been an increase in the use of MRI for such purposes [30-32].

2.3 Image Segmentation

Segmentation is the process of separating image data into structures which have a relevance to the task at hand. There are a number of different methods used to segment data and it is generally the task at hand and the type of data which determines which method to employ. Manual and semiautomatic segmentation methods can be challenging and time consuming with datasets of a significant size. It is for this reason that a number of automatic segmentation methods are commonly used in order to delineate structures of interest. There are four primary requirements to consider when choosing a segmentation technique:

- **Accuracy.** In order to be clinically useful, the results of data segmentation must be accurate. Validation studies can be used to gauge the level of accuracy and these will be discussed in further detail in chapter 6.

- **Robustness.** Robustness is an important aspect to consider when applying a segmentation technique. Any technique used should be able to work for a number of different cases. These cases could be patient position, image resolution, patient size, etc.

- **Reproducibility.** Closely related to accuracy, the results of an accurate segmentation on a specific dataset must be reproducible if applied to said dataset again. This is one of the reasons why semi-automatic and automatic segmentation techniques are generally favoured over manual segmentation.

- **Speed.** The time taken to successfully segment a dataset is important to take into account. While the results of a specific technique may be superior to others in some cases the length of time taken to complete the technique may not be feasible. The ever-increasing computational power available to users may alleviate this concern in some cases but this is often offset by the increase in resolution and size of datasets as imaging technology also evolves.

While these requirements must all be considered when choosing which segmentation techniques to apply to a dataset, the situational context must also be taken into account. For example, reproducibility may be the dominant requirement when monitoring the progression of a disease over time or, in situations where time is an issue such as in an operating room, speed might be considered more important [20].

2.3.1 Segmentation Techniques

The most common image segmentation techniques can generally be separated into five distinct categories: manual segmentation, thresholding methods, classifiers, region growing methods and clustering methods. In this section we provide a brief overview of these categories. More specialized methods such as atlas-guided approaches (which require previously known information about the data in question, such as the general location of certain anatomical structures) are not covered in this section due to their relevance.

Manual segmentation generally involves a user drawing directly on a slice of radiological data in order to outline a structure of interest. While this technique is robust it does suffer from a number of limitations. As stated previously, as a dataset increases in size, the ability to manually delineate structures of interest becomes less and less feasible due to the time required. Reproducibility is also a concern with manual segmentation. Although these limitations are associated with this segmentation technique, it is still widely used in many areas. This can be

due to a number of reasons such as datasets where contrast is simply too low or where the amount of noise is too great to apply other methods [20, 33].

Thresholding involves the selection of an intensity value (the threshold) from an image in order to create a binary partitioning of the intensities within said image. Once the intensities have been separated into two separate classes (consisting of those above the threshold and all others) then the image has been segmented. Although thresholding is a simple technique to implement and often used as an initial step in many image processing frameworks, it does suffer from a number of limitations. Its sensitivity to noise and intensity inhomogeneity (which, as mentioned in section 2.2.3.1, are inherent artefacts in MRI) making it unsuitable as a standalone segmentation technique [34-36].

Classifiers are pattern recognition techniques which aim to partition image data into specific classes. These techniques are considered to be supervised segmentation methods due to the fact that they require manually derived training data before they can be used to segment new data. One of the simplest examples of a classifier is the nearest neighbour classifier. This method partitions each pixel from a dataset into the same training data class with the closest intensity. One of the primary limitations of classifiers, especially when dealing with medical data, is the manual interaction needed to create the training data. Creating individual training sets for a large number of datasets would, in most cases, be far too time consuming to justify their use. While using a single training set in such a situation would likely lead to inaccurate segmentation due to the physiological and anatomical differences between various subjects [35].

Region growing techniques aim to segment an image region which is connected. The criteria which defines whether a region is connected is usually based on edges within the image and/or pixel intensities within the region. Region growing requires a user to pick a seed point (a pixel within the region of interest) and, in its simplest form, the technique then segments all surrounding pixels which fit the predefined criteria. For example, one possible criteria may be to extract all pixels connected to the seed until an edge is reached (a point where the intensities of the pixels being checked are substantially higher or lower then those within the region). Generally, region growing techniques are not used alone but as a stage in a set of image processing operations. This is primarily due to the limitations associated with this segmentation

technique. For example, the partial volume effect (an artefact associates with MRI) can lead to separate regions being connected and therefore incorrectly segmented [35, 37].

Clustering algorithms are known to be unsupervised segmentation methods due to the fact that they essentially function as classifiers without the need for previously defined training data. To compensate for this, clustering algorithms iterate between segmenting the image and determining the characteristic properties of each class within the data. These algorithms essentially train themselves as they progress. Three of the most common clustering algorithms used for image segmentation are the K-means algorithm, the fuzzy c-means algorithm and the expectation-maximization (EM) algorithm. Although they do not require training data, clustering algorithms do require some initial parameters in order to perform effectively. The number of classes and the initial cluster centroids are the most common parameters needed to initialize a clustering algorithm. As with most segmentation techniques, clustering algorithms do suffer limitations with regards to sensitivity to noise and intensity inhomogeneity. [35, 38, 39]

In-depth detail regarding the segmentation technique used in this piece of research can be found in section 4.6.

2.4 Quantification

Once a dataset has been successfully segmented, quantification of the tissue of interest is generally not a complex task. The general method of quantification used with MRI data is to establish the total number of pixels within a slice of data which consist of all tissues and structures present in the scan. This value is then divided through by the total number of pixels which represent the segmentation results and the result is multiplied by 100 to give a percentage of the segmented tissue within the current slice (see Figure 2-5). Once a percentage value is known for each slice of data within a volume, it can then be used to give more descriptive information regarding the distribution of the tissue of interest, such as the regional percentages of distribution (e.g. arms, legs, trunk, etc…).

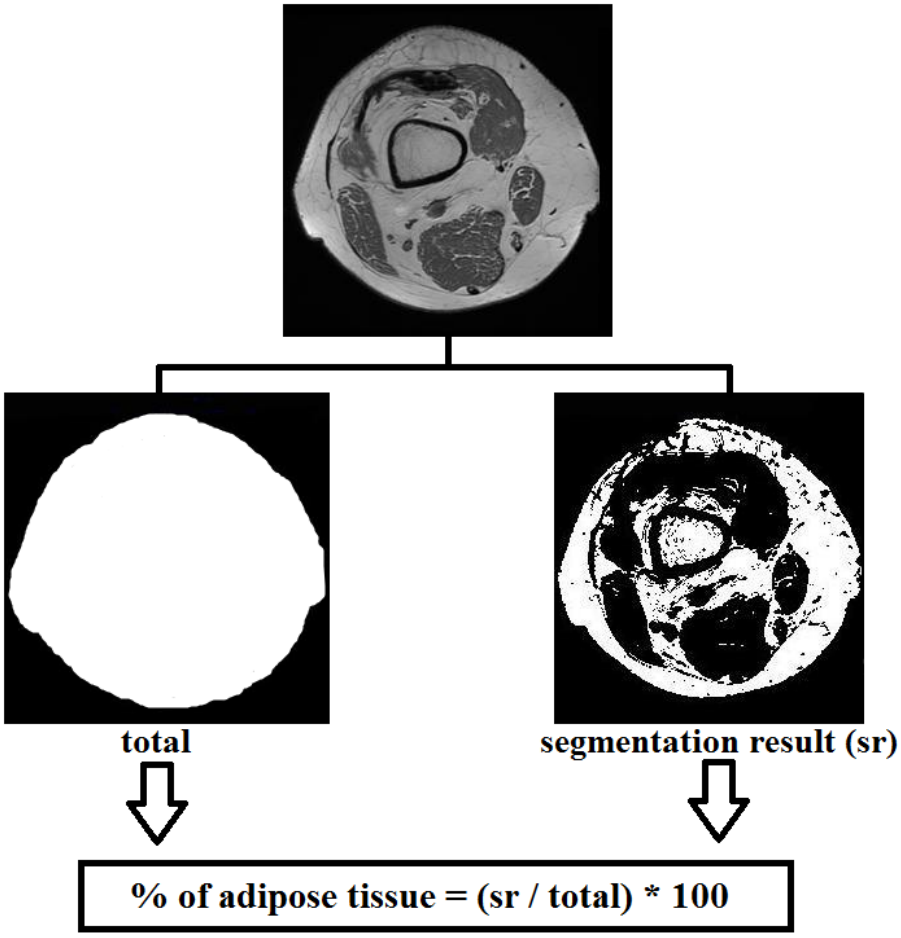

Figure 2-5 *Adipose tissue quantification*

The ability to discern the regional distribution of adipose tissue is of particular importance with regards to this piece of research due to the fact that this is the way in which DEXA provides results for body composition (as described in section 2.2.1). Greater detail as to how the adipose tissue quantification is performed and how the results are used can be found in section 4.7.

2.5 Visualization

For the purposes of this research, visualization focuses primarily on the representation of volumetric data. Volumetric data (in this case medical volumetric data) is described as a stack of aligned images/slices whose position is adjacent in the z axis and which are of the same resolution. The primary goals of volume visualization are to represent data within an entire volume in a manner that is both accurate and displays said data in as simple and intuitive way.

There are a number of different scientific data visualization techniques but with regards to medical data the two primary methods used are indirect volume visualization and direct volume visualization [20].

2.5.1 Indirect Volume Visualization

The aim of indirect volume visualization is to focus on and extract a subset of information from within a large dataset and represent it visually. One of the most commonly used indirect volume visualization techniques is surface-based volume rendering. Due to the fact that structures of interest within a volumetric dataset are typically differentiated from surrounding structures by a boundary (generally a significant change in pixel intensities from one structure to the next) one can then visually represent these structures by rendering there boundaries in 3D. The resulting rendered object is a 3d surface known as an isosurface or 3d contour. In order to define which structures are to be rendered, an isovalue must be chosen. An isovalue is treated the same as a threshold value, in that all values within a volumetric dataset below the isovalue are outside the isosurface and all values larger are inside [20].

One of the most commonly used algorithms for representing an isosurface is the marching cubes algorithm (first published in 1987 at SIGGRAPH [40]). In order to create the isosurface the algorithm ‘marches’ through a volumetric dataset and at each step takes the surrounding eight pixel intensities to create a voxel (a cube where each vertex represents one of the values of the eight pixel intensities). These eight intensities are then used to calculate the position and number of polygons to be rendered within each cube. There are 256 possible polygonal configurations which can be represented by 15 unique configurations (see Figure 2-6, all 15, when reflected and rotated make up the total 256 configurations).

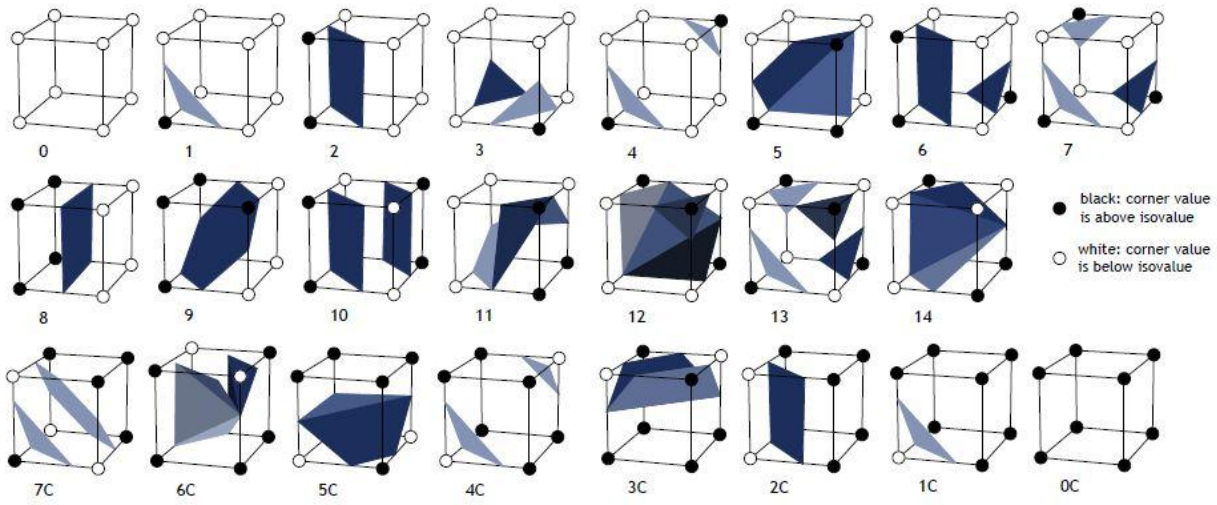

Figure 2-6 *The 15 Unique Marching Cube Cases. Image Courtesy of G. Johansson and H. Carr[41]*

Once all the voxels have been processed the isosurface can be rendered as polygonal mesh (see Figure 2-7).

Figure 2-7 *Surface Rendering*

Example of surface rendering using the marching cubes algorithm. 8 bit CT volume of a lobster with dimensions of 301 x 324 x 56. An isovalue of 35 was used.

The presence of artefacts such as holes, the diamond artefact (where individual triangles become clearly visible) or staircasing artefact are well known issues with the algorithm and there a number of solutions available for dealing with them (such as the introduction of complimentary cases for the original 15). One of the artefacts of particular interest regarding the marching cubes algorithm and this piece of research is the staircasing artefact. This artefact commonly appears when rendering an isosurface of segmented data. Due to the binary nature of segmented data (where the segmented area generally consists of high values and other areas consist of zero values) the normals (see chapter 5 for more detail regarding normal generation and 3D object shading) for each polygon which makes up the isosurface can become distorted leading to a surface which is not smooth [20].

More details regarding the use of the marching cubes algorithm with regards to this piece of research can be found in chapter 5.

2.5.2 Direct Volume Visualization

Unlike indirect volume visualization, direct volume visualization aims to represent a volumetric dataset directly without generating a meta, or intermediate, representation (such as a polygonal based isosurface) of said dataset. This means that direct volume visualization, commonly known as volume rendering, can convey much more information then surface based rendering methods, displaying not only the surface but also underlying structures (see Figure 2-8). While this is a distinct advantage over other rendering methods, there is an increased cost in algorithmic complexity and therefore the decrease in performance (the time taken to render an object) associated with volume rendering [42]. There are a number of ways to optimise and accelerate volume rendering algorithms such as using graphics processor unit (GPU) based rendering but this technique of visualizing volumetric data is heavily dependent on the quality of the hardware it can access (as the quality of a GPU increases so does the performance of the rendering).

Figure 2-8 *Example of volume rendering using ray casting. 8 bit CT volume of a lobster with dimensions of 301 x 324 x 56.*

One of the most commonly used direct volume visualization algorithms is volume ray casting. The algorithm computes a 2D image from a 3D volume. The following steps describe the volume ray casting algorithm [43]:

For every pixel of the 2D image area, a ray is cast (shot) from the camera through the volume (see 1 of Figure 2-9). The equation for the ray is defined by the start point (the camera or eye) and the direction.

1. The volume of interest is enclosed within a bounding primitive (usually a cuboid but can vary depending on the dimension of the volume). A check to see whether the ray intersects with said primitive is performed. If the ray does intersect then the algorithm travels along the ray and samples within the volume are collected at either regular or adaptive intervals (see 2 of Figure 2-9).

2. At each sample point along the ray, the surrounding data is interpolated in order to compute the intensity of the current voxel along the rays current position. A transfer function is then used to compute the RGBA value (red, green, blue and alpha values) for said voxel, e.g. the colour and opacity.

3. The algorithm composites the samples along the ray in order to calculate the final RGB value to be placed in the corresponding 2D image pixel (see 4 of Figure 2-9).

4. The process is then repeated for every pixel in the viewing pane in order to complete the image.

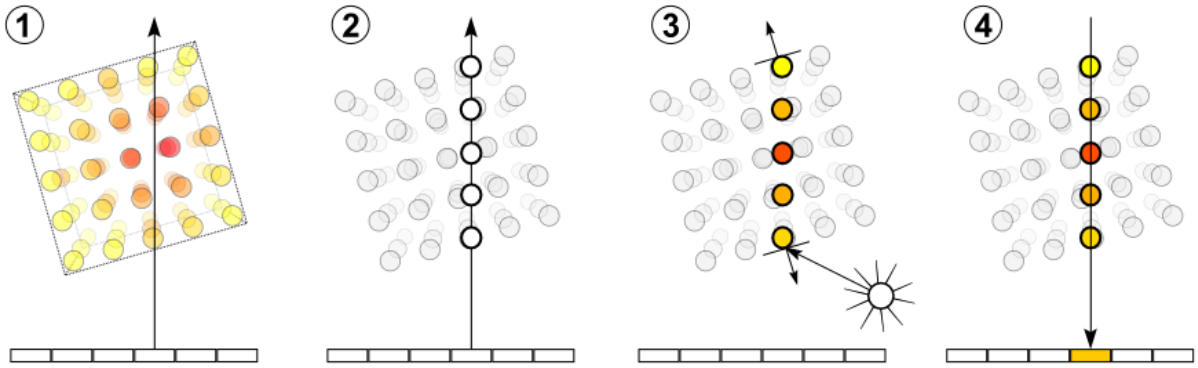

Figure 2-9 *Illustration of Volume Ray Casting [44]*

While volume ray casting does provide much more information regarding the object being rendered, when compared to surface based rendering methods, it is not necessarily the volumetric visualization technique of choice. Two primary considerations must be taken into account. Firstly, the task at hand must be considered and one should determine whether the use of a simpler technique will be sufficient for conveying the necessary information. Secondly, the performance of the algorithm should also be taken into account. What hardware will be available to the users of a software tool should be taken into consideration, especially with such a computationally expensive visualization technique.

More details regarding volume rendering and its relation to this piece of research can be found in chapter 5.

2.6 Imaging Protocol

To fulfil ethical application requirements, any diagnostic imaging undertaken during medical research requires clear and justified imaging protocols. The formulation of protocols allows clinical relevance to be discussed and confirmed amongst experts, ensures the safety of the patient in that the protocols are clinical appropriate and reproducible to facilitate full research analysis of the collected data. In the derivation of the protocols it can be checked that they are suitable for the full testing of the research methodology.

In order to ensure that all pertinent ethical considerations have been considered, that patient safety is ensured and that data collection is reproducible, an imaging protocol is necessary. This is especially important with regards to the development of a software tool which will use said data. It is also important that should an individual wish to test the methodology of a piece of research or improve upon it, that they too would be able to recreate the data used. The following sections give an overview of some of the important specifications defined for both the DEXA and MRI imaging protocols.

2.6.1 DEXA Protocol

Prior to receiving a MRI scan, patients underwent a DEXA examination at a clinical site dedicated to HIV treatment and research. The DEXA machine used was a GE Lunar Prodigy Advance. All patients were images in a supine position on the scanning bed. The maximum dimensions and weights for patients are; 263 x 111 x 128 cm (L * W * H) and 275 kg. Placement of the patient on the scanning bed was described in the operating manual and in the case where a patient is too large to fit in the scanning area then the right lateral side of the body is scanned and the results are reused to estimate the left lateral side. The current scanning protocol used by the dedicated unit was employed for this study and ethical approval for the DEXA imaging was not specifically required as this was normal imaging protocol for those attending patient review. Details of the protocol were included in the Ethical Approval application for reference (see Appendix A).

Calculation of results for body mass composition was performed by the GE software suite provided with the scanner.

2.6.2 MRI Protocol

As stated previously, the modality being investigated for this study is MRI. All imaging of patients took place in a university teaching hospital associated with the dedicated HIV treatment and research centre. All patients were scanned using a Siemens Symphony Tim System [45]. T_1-weighted full body coronal datasets were produced for each patient. T_1-weighted scans were chosen due to the increased contrast they provide between adipose tissue and other tissues present and a coronal scanning axis was chosen due to the fact that it can produce full body datasets faster then the alternative scanning axis (transverse). The following lists some of the important specifications related to the scanning protocol;

- Scanning sequence: Spin echo
- Magnetic field strength: 1.5
- Acquisition type: 2D
- Photometric interpretation: Monochrome
- Slice thickness: 7.69 mm
- Space between slices: 7.69 mm
- Samples per pixel: 1
- Bits allocated: 16
- Bits used: 12

There are two important details regarding the datasets produced for this study which directly affect some of the image processing steps performed on said datasets. The first being, each image produced is in fact three images joined at a specific location (see (a) and (b) in Figure 2-10). The second being that the dimensions for each image differ based on the height of the patient being scanned. How these details affect processing these images is discussed in greater depth in chapter 4.

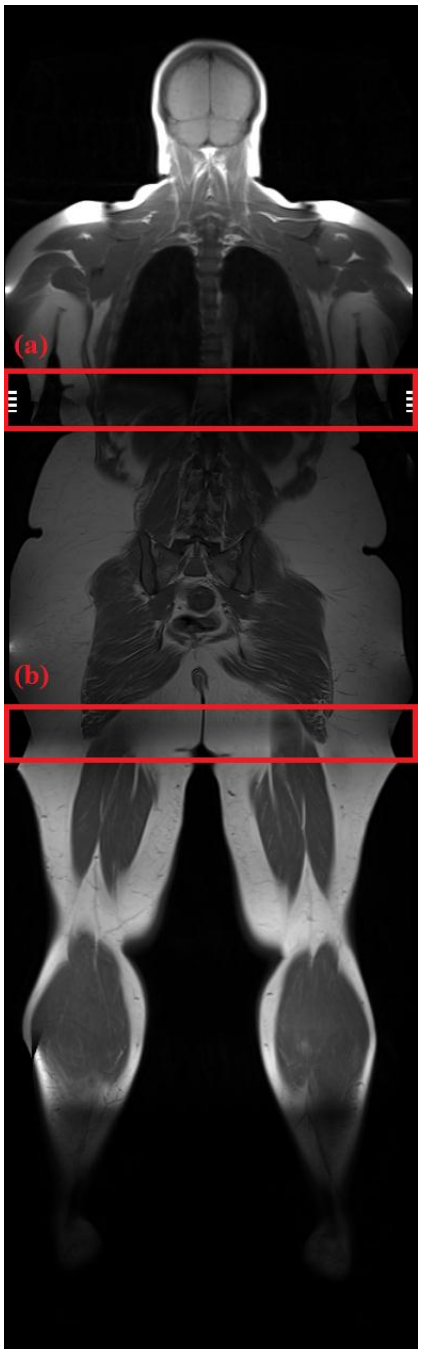

Figure 2-10 *Full Body Scan Image Joins: (a) and (b) show the location where the three images are joined together to create a full body slice.*

2.7 Chapter Summary

This chapter covered the pertinent background materials for this piece of research; HIV-associated lipodystrophy, relevant medical imaging modalities, image segmentation techniques, quantification of tissues, 3D visualization techniques and the imaging protocol used for this research. The following chapter describes the features of the graphical user interface developed for the software tool.

3 Graphical User Interface

The graphical user interface (GUI), from a users perspective, is one of the most important aspects of a software tool. A GUI should provide a user with the necessary functionality they require for the task at hand in an intuitive manner. The following sections describe the key features of the GUI developed for this piece of research.

3.1 QT

QT is a cross-platform application framework which is primarily used for the development of software applications with a GUI. The QT framework offers a wide range of functionality including integrated tools for GUI development and an intuitive application programming interface (API) with a rich C++ class library. Applications developed using QT can be deployed across all major platforms, desktops (OS X, Windows and Linux), mobile and also embedded devices without the need to re-write source code. QT is currently owned and maintained by the Nokia Corporation and has become an increasingly popular choice as a development tool for cross-platform GUI applications [46].

3.2 Graphical User Interface Overview

The first goal of the software tool is to allow the user to load and view a DICOM series. This can be done by either clicking 'Open DICOM series' in the File menu or using the open file icon in the toolbar (see (a) in Figure 3-1). Using a file dialog, the user can then select a folder containing a DICOM series. Once loaded, the GUI then displays each slice from a DICOM series in a 2D viewing pane (see (b) in Figure 3-1). The DICOM viewing pane allows the user to scroll through a DICOM series, zoom in, zoom out, and displays pixel intensities when the mouse hovers over an area of an individual image. The user has the option the display the original unprocessed images from a series, the intensity inhomogeneity and contrast corrected images and the images showing the results of the segmentation process (these will be discussed in greater detail in sections 4.5 and 4.6 respectively). The GUI also has a pane for displaying the 3D visualization (see (c) in Figure 3-1). The 3D pane allows users to manipulate the object

being displayed in a number of ways; to zoom in and out, rotate and drag the object and reset the object to its original position and size. A more in-depth description of the 3D viewing pane, what it can display and its features, is covered in chapter 5.

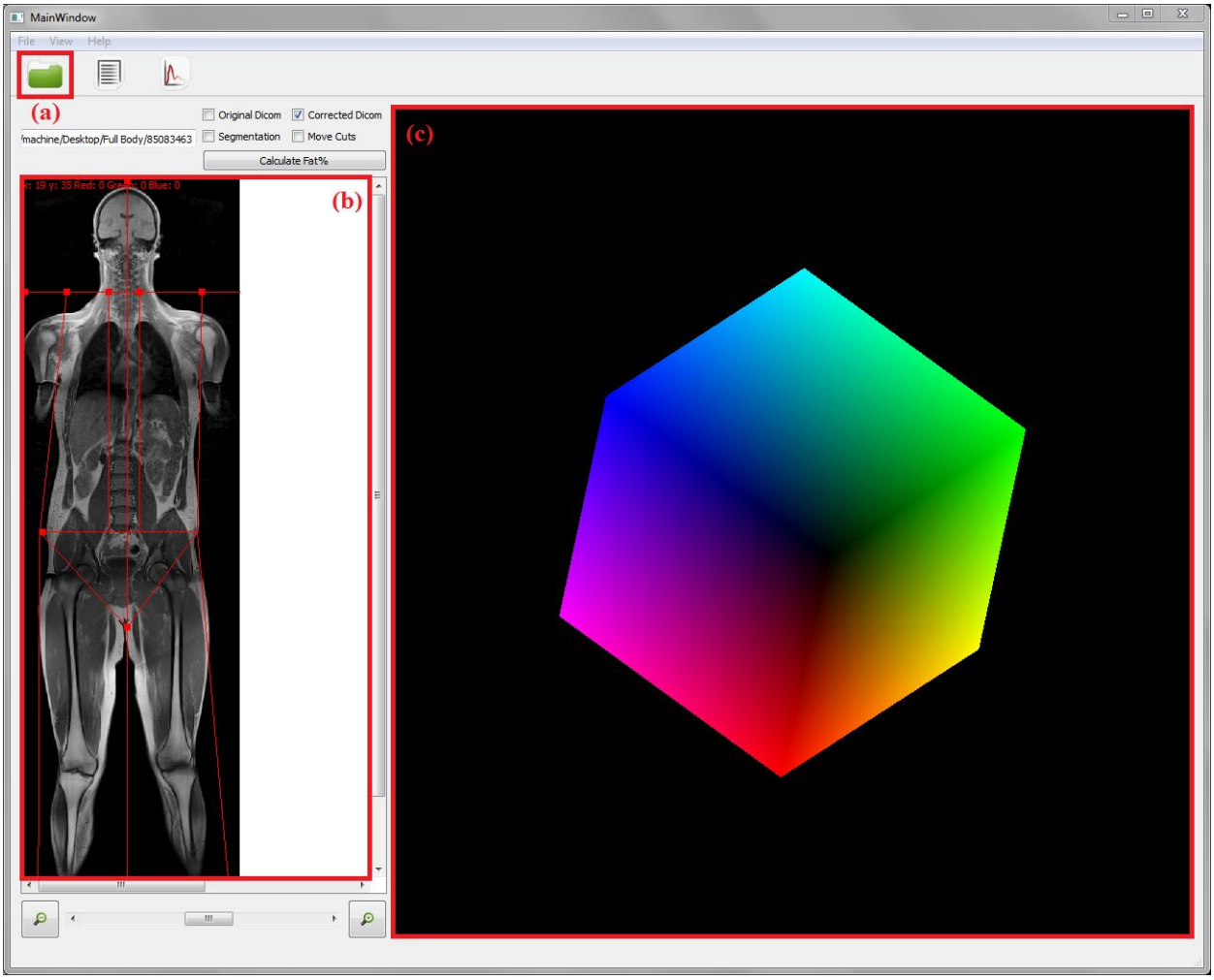

Figure 3-1 *GUI overview image 1; (a) widget to allow user to select and load a DICOM series , (b) 2D DICOM series viewing pane and (c) the 3D viewing pane.*

The GUI also allows users to view the header information from the current DICOM series being displayed. This can be accessed through the View menu or the header icon in the toolbar. The header information is displayed in a dialog in a format which is common to many medical imaging software tools; three columns displaying the tag key, tag label and tag value (see Figure 3-2). Access to information within the header data can be useful for clinicians. A number of values extracted from the header data, such as patient weight or the slice gap defined by the

imaging protocol, are used by this software tool and are discussed in greater detail in a number of the following chapters.

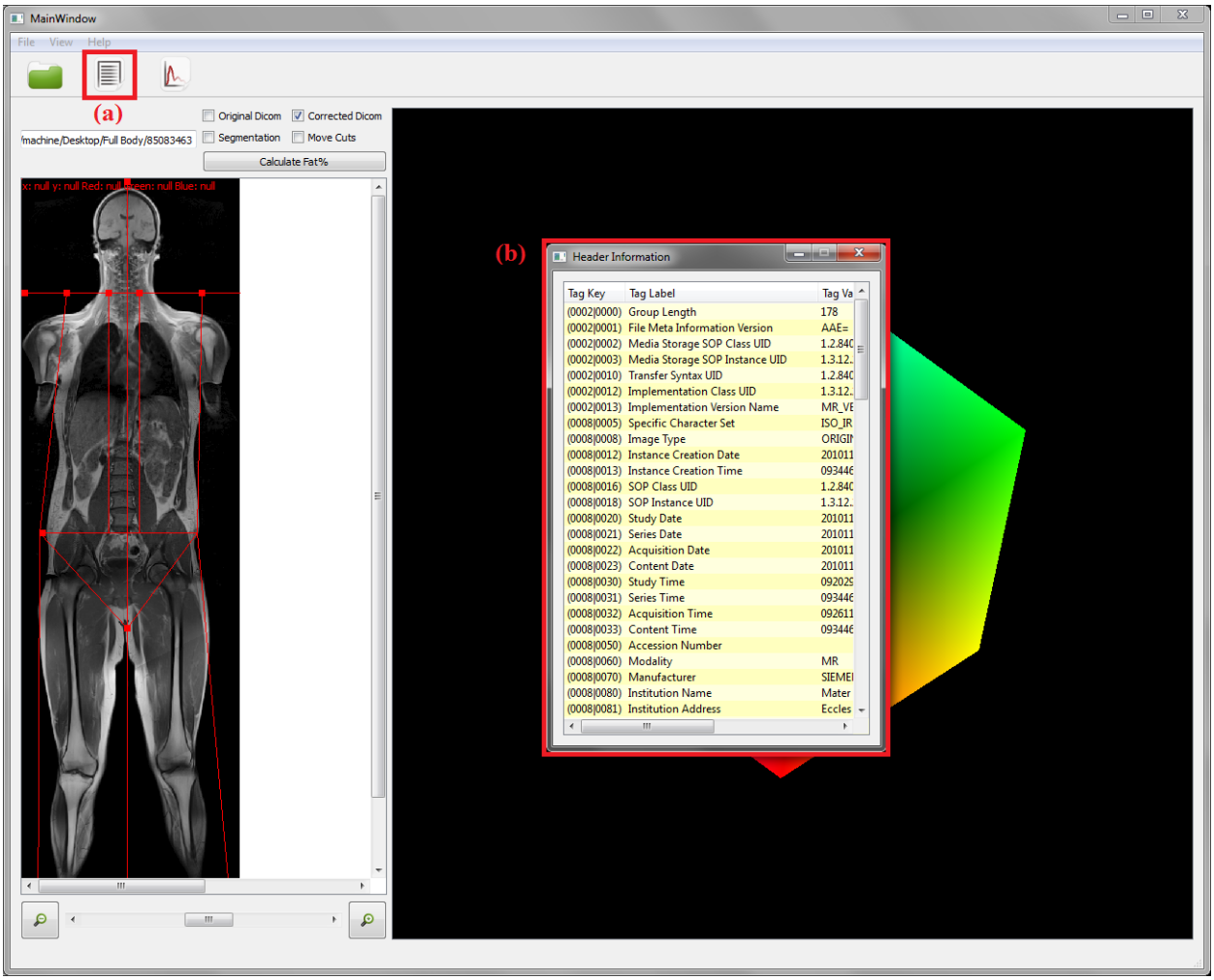

Figure 3-2 *GUI overview image 2; (a) widget to allow user to the display header information regarding the currently loaded DICOM series and (b) the dialog displaying said information.*

The user can also view the individual histograms of each DICOM within a series. As with the header information, the histograms are displayed in a dialog separate from the main GUI. The user can display the histograms of the original unprocessed images or those of the corrected images. They can also overlay the two types of histogram to be able to more clearly see the difference in the distribution of intensity values between the two types of images (see Figure 3-3).

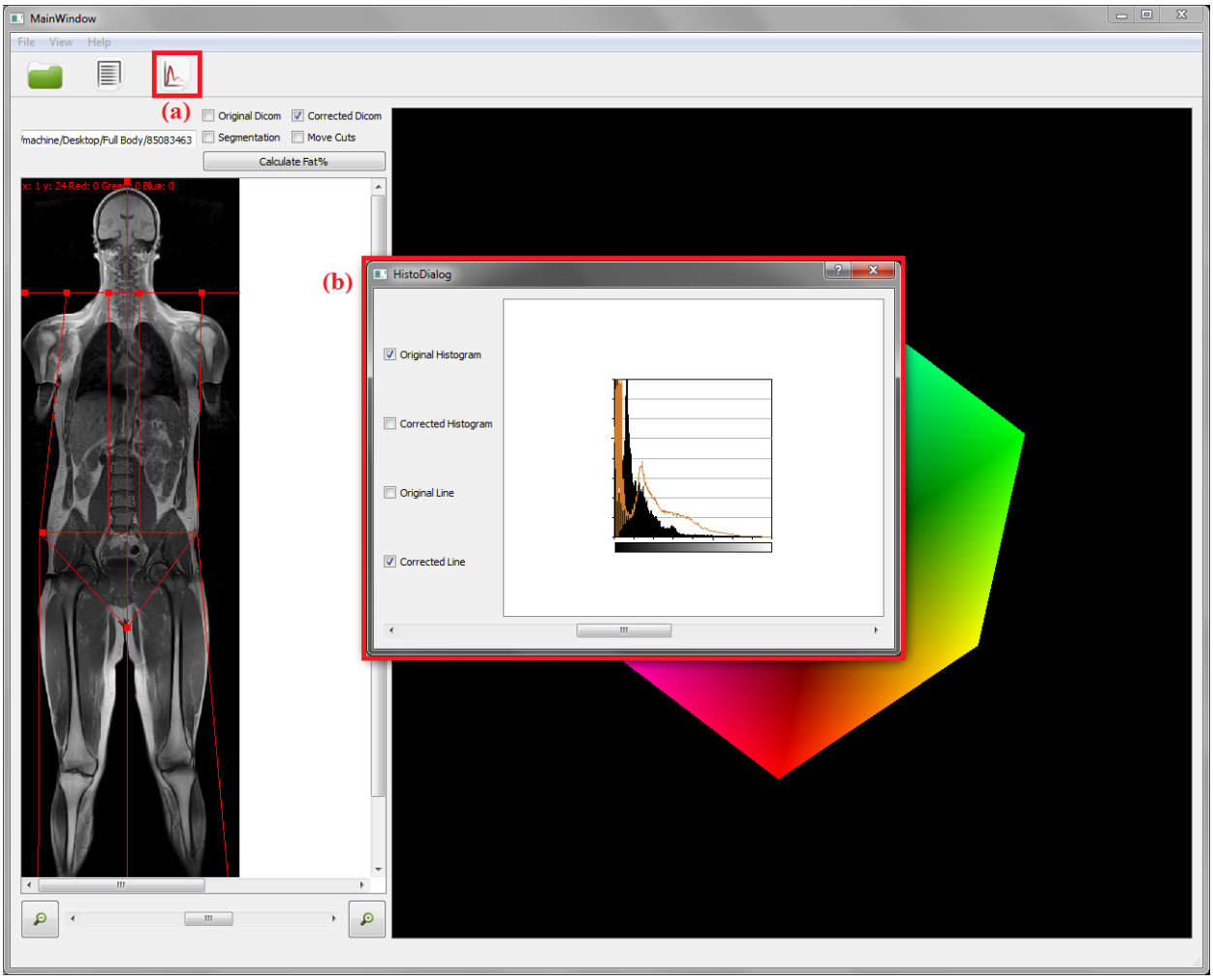

Figure 3-3 *GUI overview image 3; (a) a widget which allows the user to display statistical information regarding each DICOM within a series and (b) the dialog displaying said information.*

One of the final features of the GUI is a dialog which allows users to view the distribution of adipose tissue throughout various parts of a patient's body (see Figure 3-4). The dialog displays a both the percentage of and an approximate count, in grams, of adipose tissue in each region of the body (such as the left leg). It also displays the fat to mass ratios for specific area of the body. How these values are calculated and their relevance is covered in more detail in section 4.7.

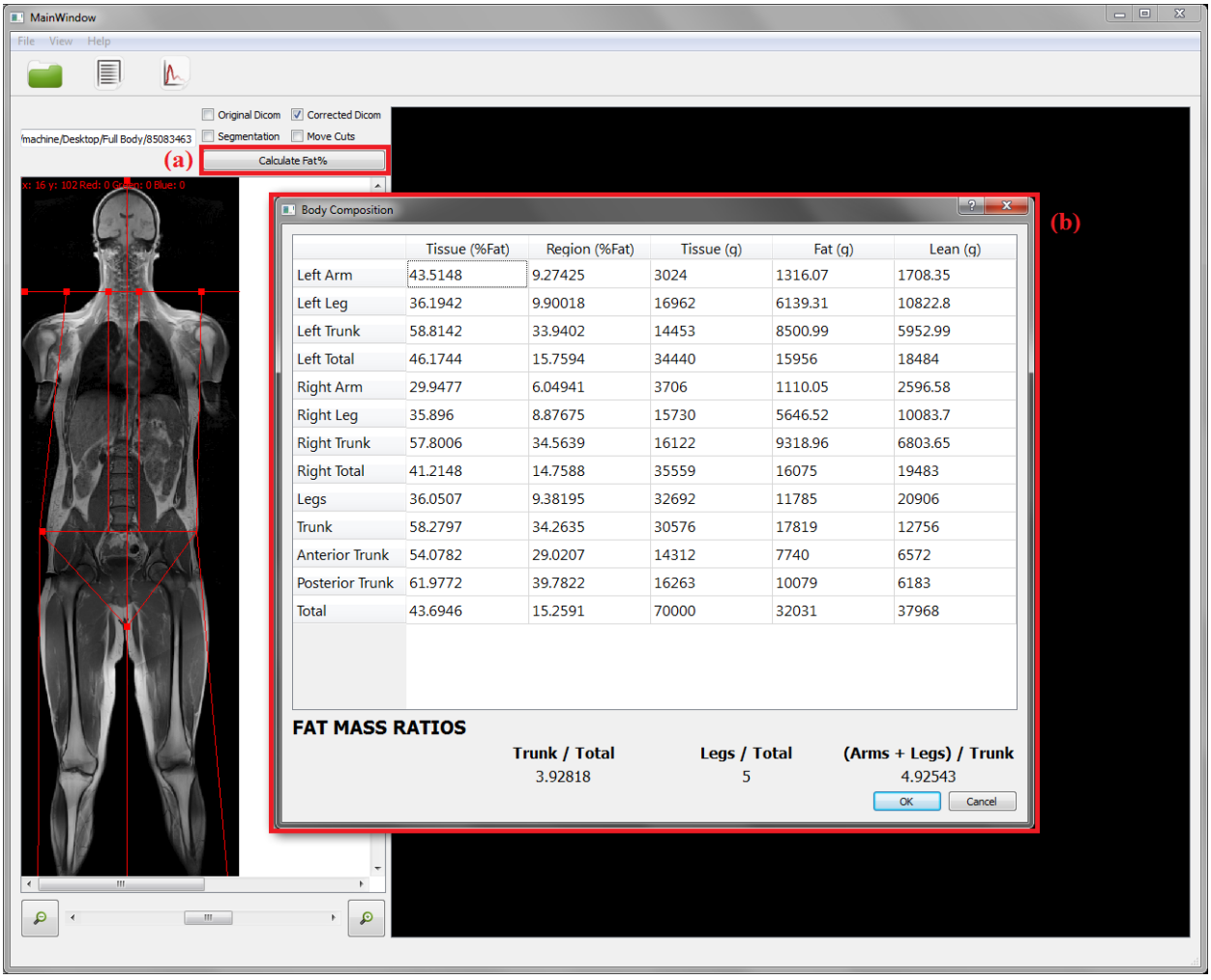

Figure 3-4 *GUI overview image 4; (a) the widget which allows users to display information regarding the distribution of adipose tissue throughout a DICOM series and (b) the dialog displaying said information.*

As stated, the GUI for this software tool has been implemented with the aim of presenting users with the data need for the task at hand in a manner that is both simple to use and intuitive. The techniques used to create the data presented to the user and the interpretation of said data is covered in detail in the following chapters.

3.3 Chapter Summary

This chapter describes the features of the graphical user interface developed for the software tool. The following chapter presents the image processing steps and algorithms implemented in

order to successfully load, segment and quantify HIV-associated lipodystrophy from full body MRI datasets.

4 Image Processing

A number of processing steps are taken before visualization or interpretation of the collected data can be performed. These include the initial processing stages such as noise reduction, contrast enhancement and intensity inhomogeneity correction. The next stages involve the application of a segmentation algorithm to said data and the gathering of results from the segmentation. The following sections describe the steps, tools and algorithms used to complete these stages.

4.1 DICOM Libraries

The medical data used in this piece of research are Digital Imaging and Communications in Medicine (DICOM) datasets. DICOM is the industry standard in medical imaging for transmitting image information. The standard was developed by the DICOM Standards Committee and is overseen by the National Electrical Manufacturers Association (NEMA) [47]. The standard defines a set of protocols to store, produce, display, process, retrieve, send, print or query medical images. DICOMs, while also providing access to pixel information regarding an image, store a number of important details relating to the image; scan time, patients details, the number of images in a dataset, details regarding the machine used, etc…

4.1.1 Insight Toolkit

The Insight Toolkit (ITK) is a segmentation and registration toolkit developed by the United States National Library of Medicine in 1999. ITK is an open-source and cross platform toolkit and was implemented in and supports C++. In the software tool developed for this research, ITK was primarily used to load DICOM files and extract relevant information from them. The reasoning for this is that a number of the more modern or complex segmentation techniques are either not yet available in ITK or are currently under patent. For example, advanced clustering methods such as the fuzzy c-means algorithms are not implemented in ITK nor is there an automatic intensity inhomogeneity correction algorithm in the library. More details as to the use of ITK can be found in section 4.4 and greater justification for not using ITK during the segmentation process can be found in section 4.6.1 [48].

4.2 Image Processing Libraries

4.2.1 OpenCV

The Open Source Computer Vision (OpenCV) library is a cross-platform programming library which focuses on real time computer vision. The library, which was originally developed by Intel and is now supported by Willow Garage, supports C and C++ and is fully open-source under the Berkeley Software Distribution (BSD) license. OpenCV functionality focuses primarily on image processing techniques and the functions available are highly optimized for both efficiency and speed. The OpenCV library is used in a number of areas in the developed software tool. Information regarding its use can be found in section 4.4 [49].

4.3 Multi-Threading

Multi-threading is a programming paradigm that is commonly employed in order to provide software developers with an abstraction of concurrent execution. In an operating system, the smallest unit of processing which can be scheduled is a thread of execution. As the name implies, multithreading allows an operating system to process multiple threads concurrently within the context of a single process. The threads are able to share the resources available but execute independently [50]. The advantage of using multithreading is an increase in speed on a computer system which has multiple cores (a common feature in modern computers). Another advantage of multithreading is that threads performing time-consume tasks can be made to work in the background allowing the main thread (the application) to handle user interaction user at the same time.

For the purposes of this piece of research multithreading was implemented for the image processing stages. Each image in a dataset was assigned a thread for the DICOM loading, intensity correction and segmentation stages of the software tool. This greatly decreased the time between a user selecting a dataset and being able to view said dataset. Multithreading was realised using QT's native threading modules (QRunnable, QThread and QThreadPool).

4.4 Loading DICOMs

The initial step of loading a DICOM series for display with the software tool developed, involves the user selecting a folder which contains a dataset. ITK is initially used to extract the header information from the DICOMs. This information is stored in order to allow the user to access it but certain specific details are extracted to be used in the loading, processing and visualizations stages. These include the image names, the dimensions of the dataset (width and height of each image and the number of slices within the dataset) and the slice gap (the space between each slice of data). The image names are used by ITK to then load each image into an itkImageFileReader object. Once loaded, ITK is then used to extract the pixel information for each slice of data.

Before any enhancement, correction or segmentation processes can be applied to the images a feature added by the MRI software must be removed. Four solid white bars are added at either edge of the images where the top sub-image is joined with the middle sub-image (see Figure 4-1, as mentioned in section 2.6.2 each image is made up of three sub-images joined together). These bars represent the highest possible intensity within the images (4095 for the datasets gathered for this research) and therefore must be removed as they were found to affect the intensity inhomogeneity correction method employed and the results of the segmentation algorithm used. Due to the fact that the general location of the bars within each image is known, they can easily be located and removed during the loading process for each individual image. As the pixel information for the images is extracted, the software checks the intensity of the first and last pixel in each row. If the intensity matches 4095 then the bar is set to the background colour (0).

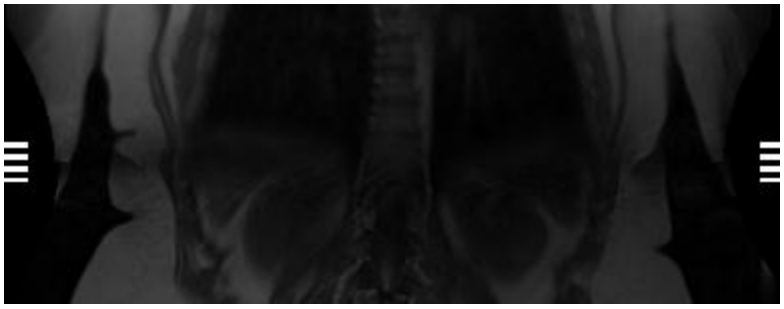

Figure 4-1 *Information added to images by MRI software; an example of an untouched MRI data slice showing the white bars applied to the MRI images by the MRI software.*

When working with most medical imaging modalities background noise is one of the most noticeable artefacts within the images. Noise in MRI images is generally modelled as having either a Rician distribution if there is a low signal-to-noise ratio (SNR) or a Gaussian distribution [25]. Rician noise is generally removed using wavelet-domain filtering while additive Gaussian noise can, in most cases, be easily detected and removed from the data using topological methods. If very little noise is present in an image, a common technique for removal is to set a low threshold when loading said image to remove the noise (for a 256 bit image this can mean setting all pixels with an intensity value of at most 15 back to zero for example). In relation to the MRI data gathered for this piece of research, it was noted that the dataset have little to no noise present and therefore more complex noise removal methods where not needed and a simple thresholding method was used in the off chance noise was present in certain images.

All of the pixel information extracted using ITK from the images is then stored in an IplImage object (a basic OpenCV storage structure) to be used in the following intensity inhomogeneity correction and segmentation steps.

4.5 Intensity Inhomogeneity

A number of methods for correcting intensity inhomogeneity, such as using 3D surfaces (for example, thin plate splines or Gaussian kernels, were tested on the datasets gathered for this study [51, 52]. It was found that methods which took into account all of the intensity information within an image in order to make a correction did not perform well on the data generated for this study. Due to the scan axis, the patient's head is included in in most of the images in a dataset and because the head is composed of primarily brain tissue and bone, it generally has much higher intensities then other areas of the body. This large area of very high intensities heavily affected a number of correction methods (especially surface based methods) in a negative manner. The fact that each image in a dataset is in actuality a composition of three separate images (as described in section 2.6.2) also affects the quality of a number of correction methods. At the two locations where the images are joined there is a significant drop in intensity values (sometimes to a point where a tissue becomes indistinguishable from the background). It was primarily due to these two reasons that an adaptive method was chosen in order to correct for intensity inhomogeneity. The follow section describes in detail the method chosen.

4.5.1 Contrast Limited Adaptive Histogram Equalization

The correction method used in this software tool is contrast limited adaptive histogram equalization (CLAHE). Ordinary histogram equalization methods take all the pixel intensity information within an image in order to transform the image histogram and thereby the intensity values within said image. By redistributing the most common intensities throughout the histogram, this method can lead to an increase in the contrast of certain objects within an image. As stated previously, one of the disadvantages of methods such as the standard histogram equalization technique is that how they affect the image can be indiscriminate due to the fact that they rely on all the intensity information within an image. This can lead to issues such as increasing the contrast of background noise or decreasing the contrast of objects of interest within an image. It is for this reason that an adaptive histogram equalization method was chosen.

Adaptive equalization methods differ from standard equalization methods by transforming each individual pixel within an image based on the histogram derived from a neighbourhood region. The neighbourhood is essentially a square surrounding the pixel in question (see Figure 4-2). The size of the square is defined before running the algorithm. Once the size of the regions is defined then the local histogram is transformed in the same method as normal histogram equalization is performed [53, 54] .

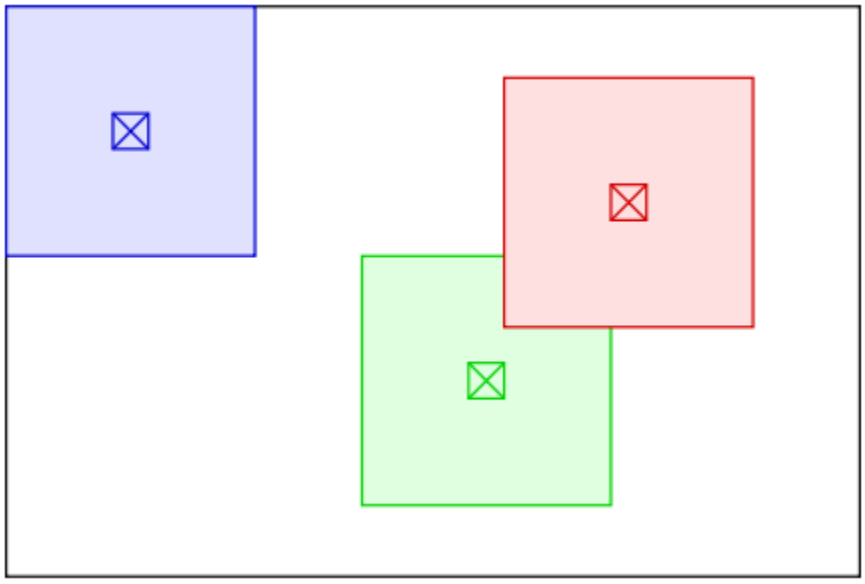

Figure 4-2 *Adaptive Histogram Equalization; example of creating neighbourhood regions within an image. [55]*

The local histogram equalization transformation is achieved by the following:

For every pixel within the region {x}, n_i is the total number of occurrences of the gray level intensity *i*. *L* is the max intensity within the region and *n* is the total number of pixels within the region.

$$P_x(i) = p(x = i) = \frac{n_i}{n}, 0 \leq i < L$$

$P_x(i)$ is the probabilty of an occurance of a pixel with the intensity *i* (normalized to [0,1]). The cumulative distribution function (CDF) is then calculated for each intensity within the region. The CDF results can also be used to create the accumulated normalized histogram.

$$cdf_x(i) = \sum_{j=0}^{i} P_x(j)$$

Once the CDFs for all the intensities within the region have been calculated, and the minimun CDF identified, the values can be used to transform the intensity values with the following formula.

$$h(i) = floor\left(\frac{cdf(i) - cdf_{min}}{(H \times W) - cdf_{min}} \times (L-1)\right)$$

Where *h(i)* is the new intensity value for all intensities n_i and H and W are the height and width of the current region [54].

The primary difference between CLAHE and other adaptive histogram methods is that it limits the contrast enhancement. A clip limit is defined and this limits the number of allowed pixels per bin within the histogram. All pixels above the clip limit are redistributed equally among the all the bins in the histogram (see Figure 4-3). This redistribution can lead to certain bins exceeding the clip limit and, depending on the parameters assigned when initializing the algorithm, the redistribution can be repeated until the level esceeding the clip limit is acceptable. For the purposes of this software tool, a clip limit of 3.0 was chosen as it increased the image quality without introducing noise. Clip limits of higher values were found to produce too much noise for any of the later image processing stages to be successfully employed.

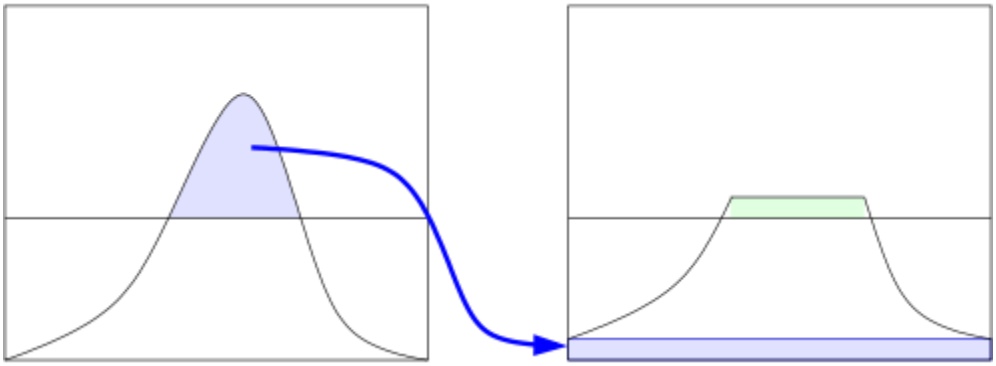

Figure 4-3 *Contrast Limiting; redistribution of intensity values through the use of a clip limit [56]*

The main of advantage of the contrast limiting feature of CLAHE is that it limits the increase in noise and over-amplification of contrast which can be caused by general adaptive histogram equalization techniques. As it can be seen in Figure 4-4 (b), a normal histogram equalization method applied to images gathered for this research does not give the best results. While the overall contrast of the image is increased, increasing the quality of the image and the definition between tissues and objects is greater, it can clearly be seen that in areas that already consist of high intensities in the original image (such as the head/neck and inner thigh) the intensities are

increased even more after equalization. This leads to tissues of the same type possibly having extreme differences in intensity values and therefore would negatively effect the results of any automatic or semi-automatic segmentation techniques. Image (c) shows the results of CLAHE applied to same image. It can be seen that the algorithm provides the necessary overall increase in contrast but without certain areas of the image becoming too bright. This leads to tissues of the same type having a more uniform distribution of intensity values. Both of these features, the increased contrast and increased uniformity, aid in increasing the accuracy of the results of the segmentation. In the following section the segmentation process applied to the gathered datasets is covered in detail.

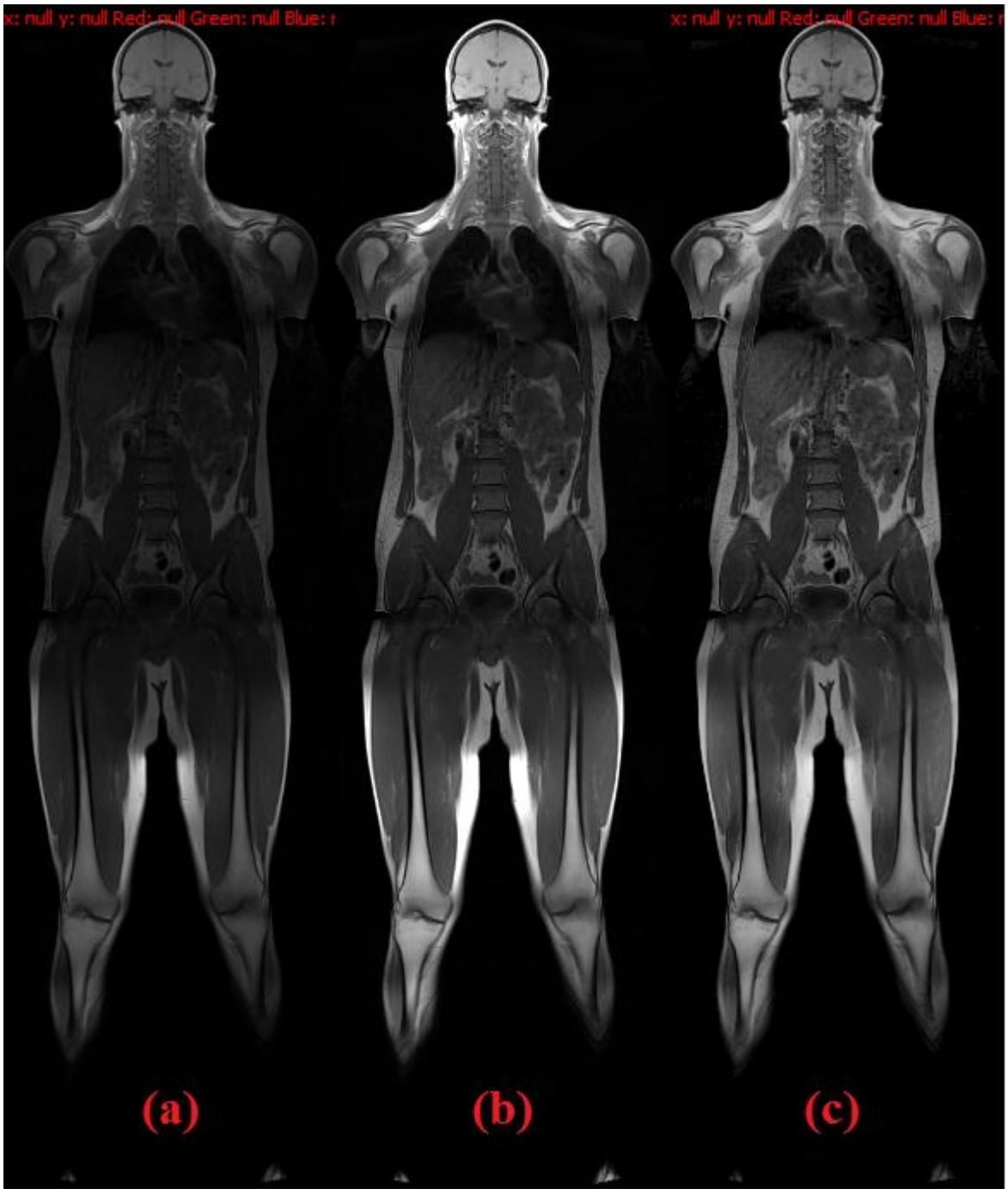

Figure 4-4 *Contrast Enhancement; (a) is the original image with no pre-processing, (b) is the image with a normal histogram equalization applied to it and (c) is the image with CLAHE applied to it.*

4.6 Adipose Segmentation

As stated in section 2.3.1, there are a number of segmentation techniques currently available which have been tested and validated on a number of image types and formats. Choosing the correct technique to apply to an image dataset can depend on the imaging modality used, the quality of the data and even the scan axis. One of the primary factors which determined which type of segmentation technique to use for this piece of research was the size of the datasets gathered. Due to the large size of the datasets (on average each slice has dimensions of 1380 * 390 with 39 slices per dataset) it was felt that any manual or semi-automatic segmentation techniques would be too time consuming, and therefore a fully automatic method was chosen. The second reason for choosing a fully automatic method (or unsupervised method) is to ensure that the segmentation results for the dataset are reproducible. The technique chosen was the fuzzy c-means clustering algorithm [57].

4.6.1 Fuzzy C-means

The central concept behind any clustering algorithm is to partition data into *k* number of clusters (or classes). This is no different with the fuzzy c-means clustering algorithm. Due to fact that the aim of this software tool is to segment one specific type of tissue, the fuzzy c-means algorithm was initialized to create two clusters; a cluster containing adipose tissue and another containing all other tissues. The first step of this initialization process is defining the centroids for each cluster before applying the algorithm to the data.

For each image within a dataset a minimum intensity representing tissue and the maximum intensity representing tissue are determined. Since it is known that adipose tissue will be the highest intensity tissue within the images the location of these pixels and their intensities are stored to be used as the initial cluster centroids for the algorithm.

Once the centroids have been chosen, the algorithm is then initiated. The central concept of the fuzzy c-means algorithm is the minimization of the following objective function.

$$J_m = \sum_{i=1}^{n}\sum_{j=1}^{c} U_{ij}^{m}\left\|x_i - c_j\right\|^2, 1 \le m \le \infty$$

Where m is any number greater then 1 (chosen before the algorithm is run), U_{ij} is the degree of membership that pixel x_i has in cluster j, c_j centroid of said cluster and $\left\|x_i - c_j\right\|^2$ expresses the similarity (or distance) between the measured pixel and the cluster centroid.

The fuzzy c-means algorithm partitions the data through iterative optiimization of the objective function. Updating the membership value U_{ij} and the cluster centroid c_j is achieved by:

$$U_{ij} = \frac{1}{\sum_{k=1}^{c}\left(\frac{\left\|x_i - c_j\right\|}{\left\|x_i - c_k\right\|}\right)^{\frac{2}{m-1}}}$$

$$c_j = \frac{\sum_{i=1}^{n} U_{ij}^{m} \times x_i}{\sum_{j-1}^{n} U_{ij}^{m}}$$

The algorithm has two stopping conditions. If $\left\|U_{ij}^{k+1} - U_{ij}^{k}\right\| < \varepsilon$, where ε is a predefined value (usually known as the accuracy) between zero and one and k is the current iteration, then the algorithm will stop. The algorithm is also assigned a maximum number of iterations it can perform in order to ensure the algorithm stops in the case where the objective function does not reach a point where it is lower then the predefined accuracy.

The following describes the steps of the algorithm:

1. Calculate Centroids for a slice of data (min and max pixel present in tissue).
2. Initialize a matrix $\left[U_{ij}\right]$.
3. For k iterations.
4. At step k, calculate the cluster centroids c_j.
5. Update the membership values for U_{ij}^{k} and U_{ij}^{k+1}.

6. Check if the objective function is less then the accuracy or if the maximum number of iterations has been reached, if then stop, If not then return to step 3.

The appropriate *m* value to choose before imitating the fuzzy c-means algorithm is a much discussed issue in regards to the quality of the output. Choosing an appropriate value for the accuracy value and the number of iterations that the algorithm can perform can greatly affect the segmentation results. By testing a number of different values, it was felt that an accuracy of 0.0001 and 40 iterations produced the best results in an acceptable amount of time. Similarly, based on testing the algorithm on a number of datasets and available literature, a *m* value of 2 was found to generate the best results [58].

The fuzzy c-means clustering algorithm has been used extensively for image segmentation and has proven itself to be a useful and accurate technique for performing automatic segmentation in numerous fields including medical imaging [59-61].

4.7 Adipose Quantification

Once segmentation has been successfully performed on a dataset, quantification of the segmented tissue takes place. As stated in section 2.4, for every slice in a dataset the amount of pixels which represent all parts of the body are summed as are the number of pixels representing the segmented tissue (all pixels with a value greater then 10, with all others considered to be background). The sum of the segmented tissue is then divided through by the sum of all tissues and the result multiplied by 100. This gives the total percentage of the segmented tissue for the entire dataset. While this information can be useful, in order to make a proper comparison to the current gold standard (DEXA) much more informative data needs to be presented to the user. The following section describes in detail how this was achieved.

4.7.1 Quantification Method

After consultation with the clinicians involved with this project, it was decided to quantify and present the results of the segmentation in as similar a method as DEXA. This would allow for a better comparison between the two methods and give the user much more information regarding the distribution of the segmented tissue throughout regions of the body.

In order to simulate how DEXA presents its results, it was necessary to implement cut lines which overlay the MRI DICOMs. The cut lines can be seen in Figure 4-5, they are represented as red lines with small squares located at specific points. The user can change the position of all of the cut lines by clicking the ‘Move Cuts’ radio button and dragging the red squares to the location they desire. In general, the vertical central and spinal cuts do not need to be moved, nor does the horizontal neck cut.

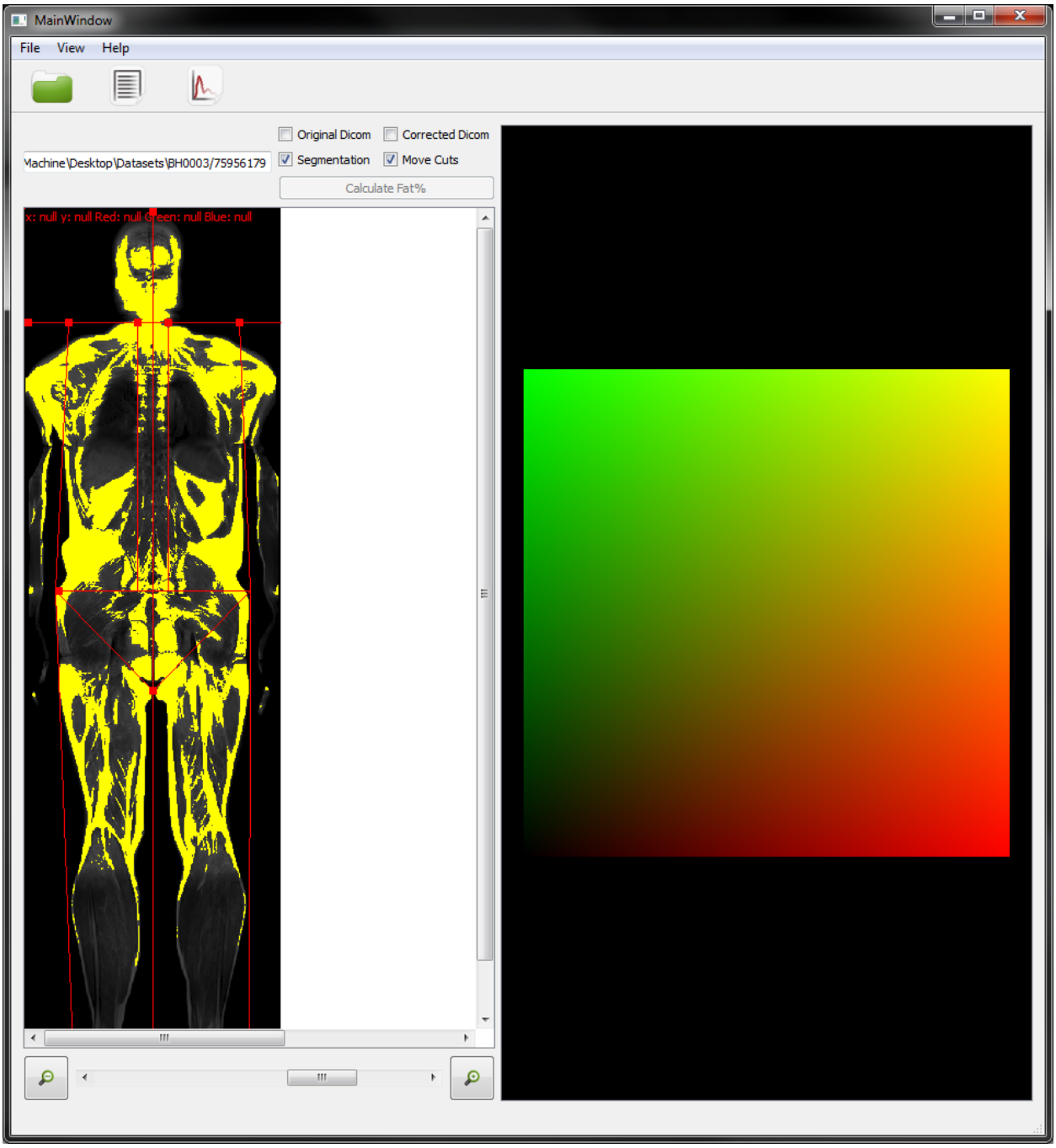

Figure 4-5 *Example of DEXA-style Cut Lines Applied to MRI DICOMs*

Once the user is satisfied with the position of the cut lines, they can then unclick the 'Move Cuts' radio button and click the 'Calculate Fat%' button in order to view the results (see Figure 4-6).

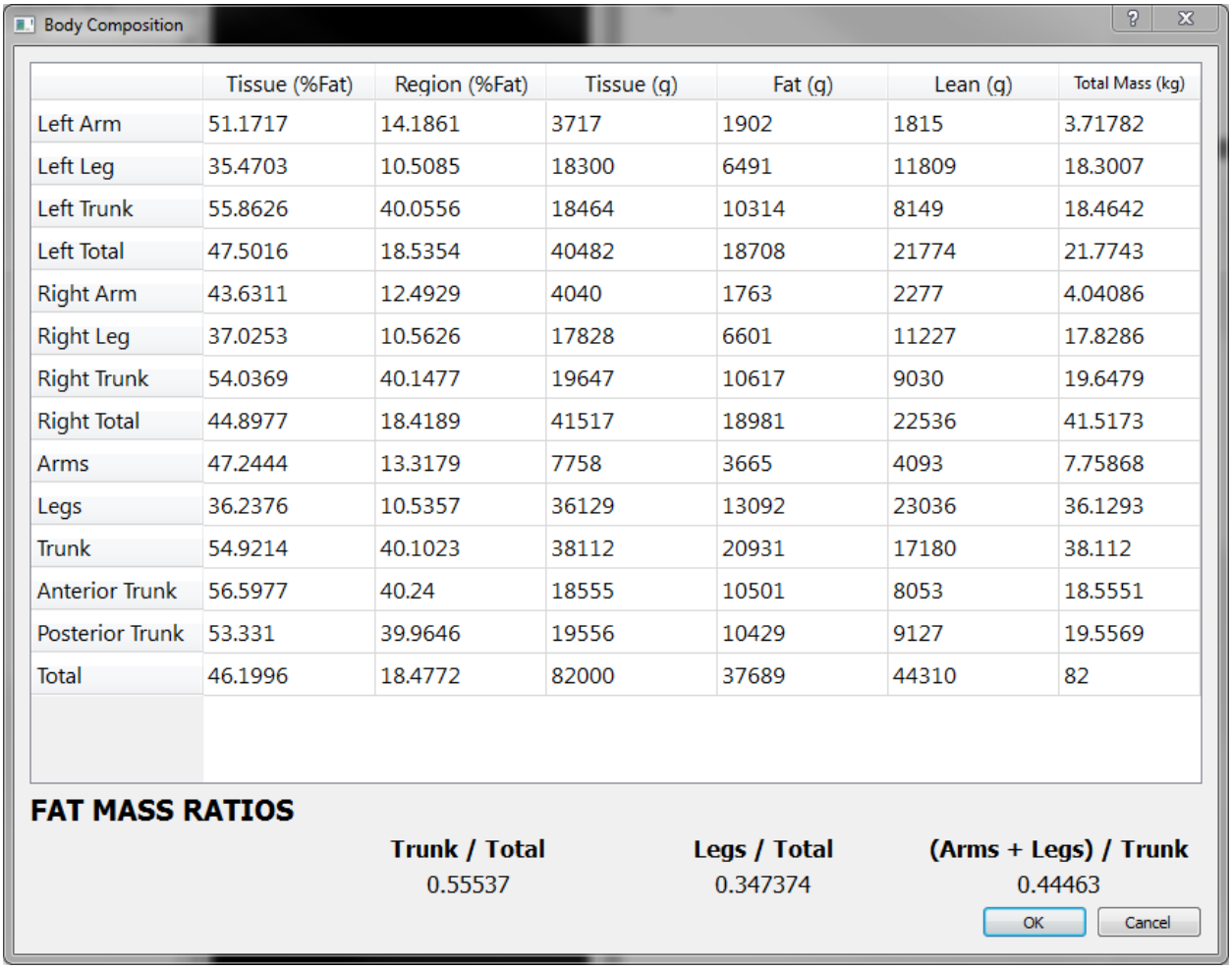

Figure 4-6 *Example of DEXA-style Results from a MRI Dataset*

With the application of the cut lines, the user can be presented with the percentage of fat present in each area of the body (similar to DEXA) but, in order to give more detailed results such as DEXA does, not only the percentage of fat needed to be presented but the amount of fat in grams also needed to be presented. For each pixel which represents part of a scanned patient's body, an estimation of the weight in grams each pixel represents must be calculated (all pixels with an intensity value above 10 were considered tissue and those below either background or noise). By extracting a patient's weight (which is stored in kilograms) from the MRI DICOM header information of a dataset and multiplying by 1000, the patients weight in grams is determined. Then, dividing through this number by the total number of pixels which represent the patient's body gives the estimation of weight in grams for each pixel.

$$(patient\_weight \times 1000) / \sum tissue\_pixels$$

Once the weight in grams for each pixel has been calculated, this can then be used to estimate the amount of grams of fat and non-fat in each area of the body.

One of the primary differences between the results from DEXA and those of the software tool developed for this project is the ability to display information regarding the distribution of fat in the anterior and posterior areas of the body. The software tool presents the user with the fat distribution of both the anterior and posterior trunk. Due to the increase in fat in the dorsocervical region and in the abdomen as the condition of HIV-associated lipodystrophy progresses, it was felt that displaying this information would be of interest to clinicians. More detail as to how this information would be beneficial can be found in section 8.5. Once the results of fat distribution have been calculated for a patient, the user can export them to a spread sheet to be used for further analysis. Detailed information regarding the performance of the software tool and statistical analysis of the results gathered for both DEXA and MRI can be found in chapter 7.

4.8 Chapter Summary

This chapter presents the image processing steps and algorithms implemented in order to successfully load, segments and quantify adipose tissue from full body MRI datasets. The following chapter covers the 3D visualization elements of the software tool.

5 Visualization

5.1.1 OpenGL

The library used to implement volume visualization for this project was OpenGL. OpenGL is currently the industry standard programming library for the creation of complex 3D graphics and is widely used in scientific visualization. The OpenGL API offers developers many functions that allow the rendering of complex three dimensional objects and scenes from simple geometric primitives. OpenGL is a cross platform library and is portable across a number of different graphics cards (GPUs). OpenGL is currently manage by the Khronos Group [62].

5.2 Volume Rendering

Ray casting volume rendering was implemented for this project but, due to a number of reasons, was not included in the final software tool. At the time of implementation volume rendering of an entire dataset was tested on a high-end laptop with the following specifications: a NVIDIA GeForce GTX 260m with 1024 MB of GDDR3 memory available, 4 GB of ram and an Intel Core i5 with a 2.8 GHz clock frequency. The time taken to render a full dataset was considered to be too slow in order to be used in a clinical setting. This was also reinforced by the frames per second (FPS) when rotating or moving the volume within the viewing pane. The average FPS were generally less then 20 FPS, which hampered the responsiveness of the rendering. It was also felt, by both the researcher and the clinicians involved in the project, that due to the physical characteristics associated with HIV-associated lipodystrophy (lipoatrophy of the limbs, increased size of the abdomen and increased fat in the dorsocervical region) that visualizing the external morphology of the patients would be of greater interest. It is for these reasons that surface rendering was chosen as then method of volume visualization for this piece of research.

5.3 Surface Rendering

The Marching Cubes algorithm was used for volume visualization in this project. After a number of different techniques were tested it was decided that applying a RGB heat map applied to the rendered surface would be an interesting and informative way of presenting the

distribution of adipose tissue throughout the body. The heat map ranges from blue (little or no adipose tissue) to red (almost completely adipose). The percentage of adipose tissue present at each level of the image height is converted into a RGB value (based on the heat map) and the polygons to be rendered for that part of the surface are subsequently set that RGB value. While also presenting the distribution of adipose tissue throughout the body in an intuitive manner, the full body renderings also allow the user to clearly see a patient's external morphology which could be useful for identifying changes in body shape due to the progression of HIV-associated lipodystrophy.

Examples from the software tool developed for this study of full body volume visualization with the heat map applied can be seen in Figure 5-1 and Figure 5-2.

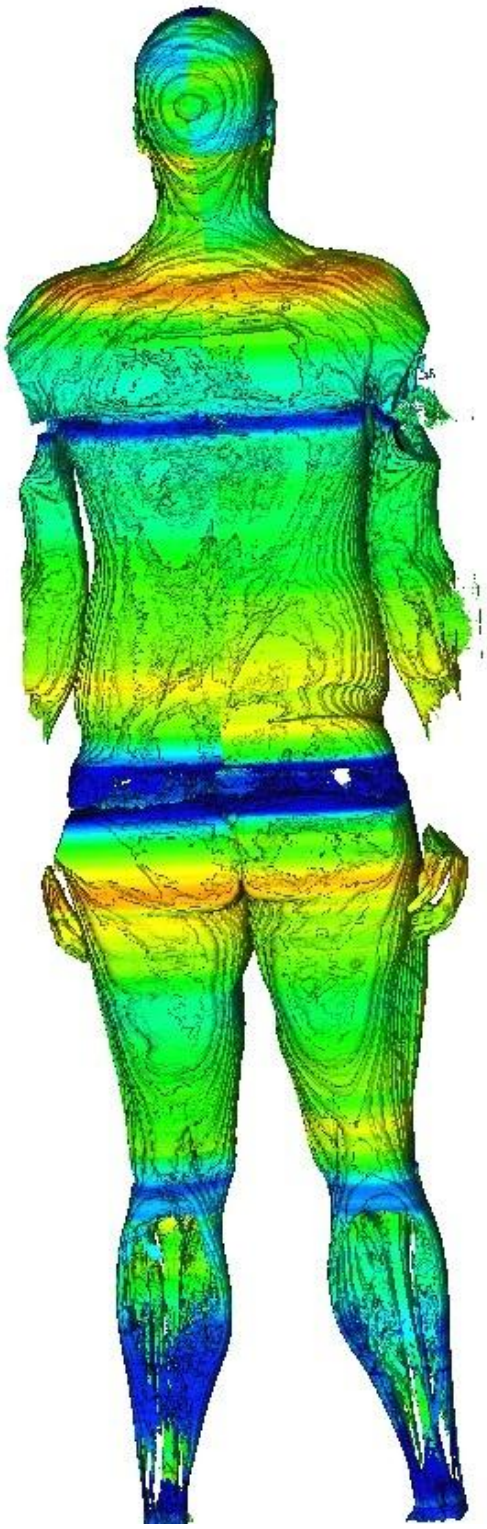

Figure 5-1 *Full Body Rendering with Heat Map*

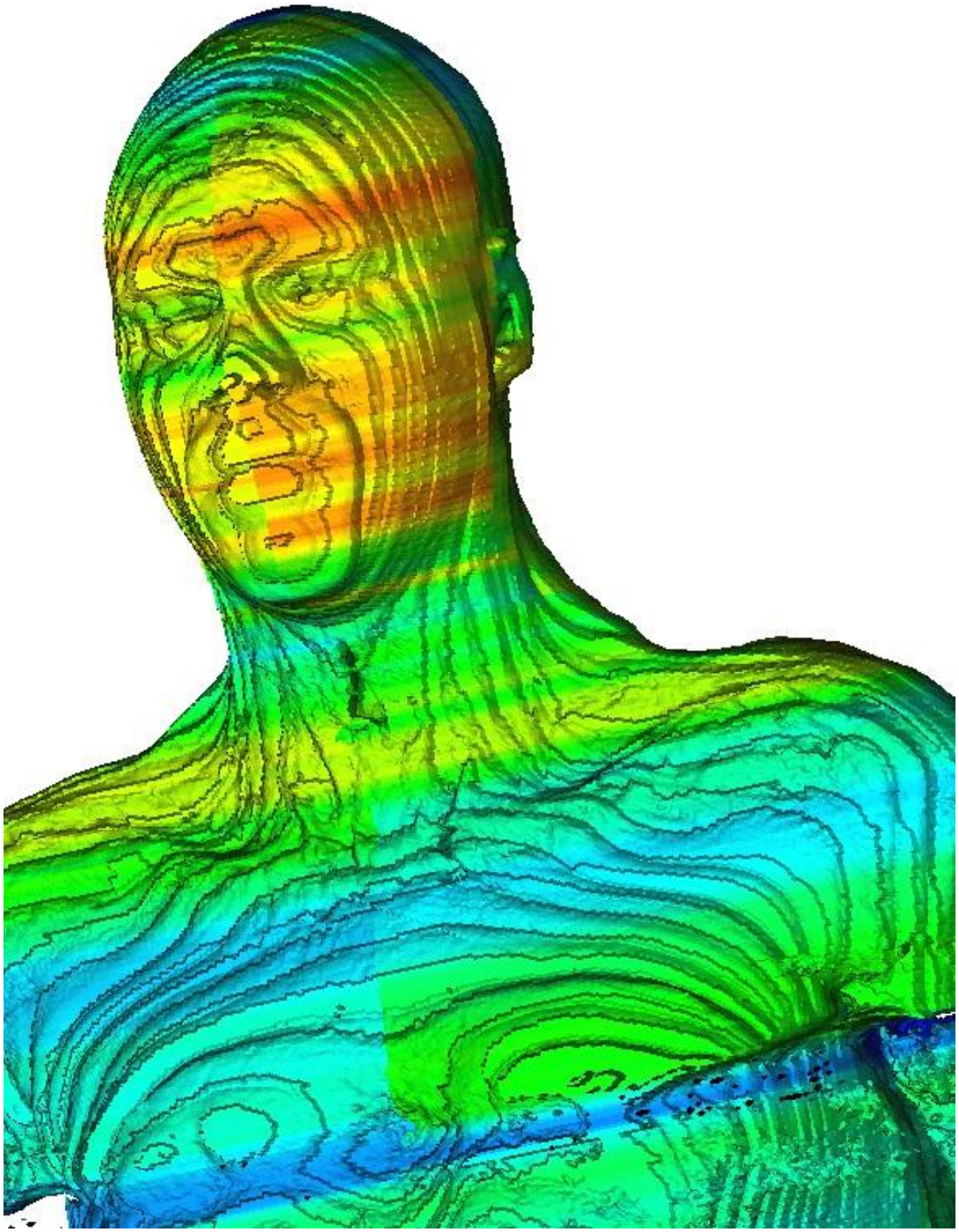

Figure 5-2 *Magnified Full Body Rendering with Heat Map*

In order to for the volume visualization to appear correct to a user, lighting must be applied to the scene to make the object visible and to create shadows. Each polygon rendered has normals calculated for it in order to ensure they are correctly lit and to give the object a smoother shading effect. Due to the large nature of the datasets gathered for this project, 'flat' shading was used rather then 'smooth' shading. Flat shading involves the calculation of normals for each triangle within the rendered surface and is done at runtime while the polygons themselves are being calculated. In order to achieve smooth, shading interpolation is used on the normals for each vertex of a triangle which is more computationally expensive. The object rendered must also be scaled along the *z* axis in order to represent the patient's body correctly. This is due to the slice gap between the MRI slices. By extracting the slice gap from the header information, the object can be scaled by the correct amount.

5.3.1 Interaction with the Volume

In order to allow users to fully interact with the 3D volume, the functionality to digitally zoom, pan and rotate the object have all been implemented. A user can magnify the object using the mouse wheel and pan the object by right-clicking it and dragging it to the desired location. 3D rotation is achieved through the use of an arcball. The arcball, first described by Shoemake, utilises quaternion-based rotation which prevents gimbal lock (the loss of one degree of freedom leading to the system being restricted to only two rotational axis) [63]. The user can rotate the object of interest by left-clicking it and dragging. It is important to note that the arcball is always centered around the object, even when magnified or panned, in order to insure correct rotation.

5.4 Chapter Summary

This chapter covers the 3D visualization elements of the software tool. The following chapter describes, in detail, the methodologies employed in order to evaluate and validate the software tool as a whole and the data gathered by said tool.

6 Evaluation Methodologies and Clinical Validation

The following chapter describes methods used to evaluate the software tool developed as a proof of concept for this research. An overview of ethical considerations and patient selection is also presented.

6.1 Quantitative Evaluation

In order to assess the results gathered from MRI datasets and how they compare to those of DEXA, a quantitative evaluation was performed on the data collected. As the primary concern of this research was the quantification of adipose tissue, the primary data used was the percentage of fat present in all areas of the body for all patients which took part in the study. The two statistical analysis techniques used to assess the two modalities were Pearson's correlation coefficient and the Bland Altman method. The statistical software tool MedCalc was used to analyse the gathered data. MedCalc was specifically developed for statistical analysis for biomedical research [64]. In-depth detail regarding the results of analysis can be found in chapter 7.

6.1.1 Pearson's Correlation Coefficient

In order to determine whether there is a statistical relation between the results collected from the two imaging modalities employed in this study, Pearson's correlation coefficient (PCC) was used. PCCs gives a measure of the correlation, or linear dependence, between two variables. The PCCs between said variables is defined as the covariance (how similarly the two variables change together) of the two variables divided by the product of their standard deviation. The result of PCCs, generally denoted by *r*, ranges from 1 to -1. A result of 1 suggests a perfect linear correlation between the two variables (as variable X increases so does variable Y). A value of -1 indicates the variables have a negative correlation (as values for X increase, Y decreases) and 0 indicates no correlation between the two variables. General guidelines for interpretation of the correlation coefficient have been put forward (see Table 6-1) [65].

Table 6-1 *Guidelines for the Interpretation of the Correlation Coefficient*

Correlation	Negative	Positive
None	−0.09 to 0.0	0.0 to 0.09
Small	−0.3 to −0.1	0.1 to 0.3
Medium	−0.5 to −0.3	0.3 to 0.5
Strong	−1.0 to −0.5	0.5 to 1.0

For the purposes of this research, Pearson's correlation coefficient was applied to the gathered data in order to determine whether a correlation existed between the MRI and DEXA imaging results. Greater detail on the results can be found in section 7.2.

6.1.2 Bland Altman Method

As stated in the previous section, a high positive correlation between two methods does not necessarily indicate that there is good agreement between said methods [66]. The Bland Altman method presents the data in a graphical style so that the range of absolute differences between measurements and the overall measurement variability (the system bias) can be easily observed. The difference between measurements for an individual case can be estimated by calculating the standard deviation of the differences across the sample and the system bias is calculated as the mean of the signed differences between two measurements for a specific subject. If the distribution of difference is reasonably symmetrical, then the difference between the measurements of the two methods will fall within the range of ± two standard deviations (specifically ±1.96) in 95% of cases. The standard deviation of the differences can be calculated as the square root of the sum of the squared differences divided by the sample size. The confidence limits above and below the mean (the system bias) demonstrate the influence of random variations between the ratings.

If the two methods tend to agree, then the mean will be near zero. If one method consistently gives higher results then the other then the mean will be far from zero and there will be a narrow confidence limit. Alternatively, if the methods do not appear to agree and there is no consistent pattern in the results (one method consistently higher than the other), then the mean will be near zero but the confidence limit will be very wide [66].

The Bland Altman method was used in order to assess the level of agreement between the two modalities being studied. The results of the Bland Altman method can be seen in section 7.3.

6.2 Qualitative Evaluation

In order to assess the accuracy of the segmentation technique used in this project an evaluation of the technique was performed where a panel of experts were asked to score the accuracy of adipose tissue segmentation. If the segmentation performed on the gathered datasets is not sufficiently accurate, then any quantitative evaluation of the segmentation results would be flawed.

In order to assess the quality of the segmentation a group of experts in the field, both radiologists and radiographers, were asked to take part in evaluating the segmentation results. In total, seven individuals took part in the evaluation. The participants were presented with 11 randomly selected slices from the MRI datasets. Images of the un-segmented slice and the segmented slice were presented side by side and participants were given instructions to score each image between one and five based on following criteria:

- False Negative Segmentation (FN), the amount of adipose tissue missed (not segmented). With one being no adipose tissue missed and five being all adipose tissue missed.

- False Positive Segmentation (FP), the amount of non-adipose tissue segmented. With one being no non-adipose tissue falsely segmented and five being all non-adipose tissue being segmented.

- True Positive Segmentation (TP), the amount of adipose tissue correctly segmented. With one being no adipose tissue segmented and five being all adipose tissue correctly segmented.

The results gathered from the evaluation and the analysis of said results can be found in chapter 7.

6.3 Ethical Considerations

In any research which involves patients directly or in which patient information is recorded and used, ethics permission is required. This study involved additional imaging in the form of a MRI examination. Patients required preparation for the examination, doctor consent and radiology reporting of the subsequent images. This was a change in patient management and therefore required full institutional ethical approval. An ethics committee reviews research ethics proposals and grants them permission if they are confident that the patient's best interests will be maintained and that the research parties involved will be competent in maintaining patient confidentiality. All necessary protocols for the MRI examination were formulated and included in the ethical approval application, this included detail of how patient data sets were to be managed. During the various stages of this research, all information was stored in one secure place on encrypted computer appliances. Throughout this project, the researcher was only supplied with information deemed relevant to the task at hand. At the beginning of the evaluation stage, an ethics application was submitted by the associated HIV clinician to the relevant hospital institutional ethics board and ethical approval was subsequently granted. Details of the ethics proposal can be found in Appendix A.

6.4 Patient Selection

The researcher worked with a clinical team from both a dedicated research unit involved in HIV research and a university teaching hospital both linked though an Irish Academic medical centre. Recruitment of patients was initiated through the research team in the research centre and MRI and DEXA imaging was performed in the clinical sites. Initial meetings with the clinical team facilitated the identification of the staff responsible for patient recruitment and DEXA and MRI imaging. Good communication systems were established between the clinical staff and the

researcher and a method of forwarding scans and related data to the researcher were agreed upon. In order to ascertain patient anonymity each patient was assigned a study code.

The recruitment of patients took place over a period of one year and in total nine patients underwent DEXA and MRI examinations. Both examinations were performed in a single day for each patient to ensure no changes in physiology between examinations. Patient demographics can be seen in Table 6-2.

Table 6-2 *Patient Demographics*

Code	Age	Sex	Ethnic Origin	Height (cm)	Weight (kg)	BMI
BHR007	56	M	Caucasian	174.7	81.1	26.6
BHC001A	37	F	African	172	72.3	24.4
BH0004	33	F	Caucasian	158	101.4	40.6
BH0001	35	F	African	166	99.4	36.1
BHR008	38	F	African	165	82.3	30.4
BHC002A	35	F	African	168	71.6	25.4
BH0003	51	M	Caucasian	173	92.5	30.9
BH0002	35	F	African	162	83.4	31.8
BHR009	57	M	Caucasian	170	80.1	27.7

A number of issues arose during the recruitment and imaging stages of the project which affected the overall size of the patient cohort (specifically the high weight of many of the patients was found to be a confounder with respect to suitability for MR imaging). A number of patients also declined from participating. To raise the number of recruits an initial proposal was made to extend the recruitment process to alternative clinical sites. However the time required to complete the ethical approval process in distal sites for this was deemed impractical and a decision made to recruit solely from the initial Clinical site.

It should be noted that during the evaluation stage it was discovered that MRI dataset BH007 was corrupted and therefore unusable. Due to this, the data from this dataset was not used chapter 7.

6.5 Chapter Summary

This chapter describes, in detail, the methodologies employed in order to evaluate and validate the software tool as a whole and the data gathered by said tool. The following chapter presents the results gathered from the evaluation of the software tool.

7 Results

This chapter reports in detail the data gathered during the clinical trial period for this research and provides the results emanating from the statistical analysis performed on said data to assess the features and results of the software tool developed over the current method (i.e. DEXA). The performance of the software tool, the accuracy of the segmentation results and a comparison of the results gathered from DEXA and MRI will be discussed in the following sections.

7.1 Overview of Data Gathered from DEXA and MRI Examinations

The mean DEXA and MRI results were gathered along with the standard deviation for each set of results (see Table 7-1, Table 7-2, Table 7-3, Table 7-4, Table 7-5 and Table 7-6). Individual results for each patient for DEXA can be seen in Appendix B and the individual results for MRI can be seen in Appendix C.

Table 7-1 *Overall Mean Results Gathered for all DEXA and MRI Cases*

	DEXA		MRI		DEXA		MRI	
Region	**Tissue (%Fat)**	**STDEV**	**Tissue (%Fat)**	**STDEV**	**Region (%Fat)**	**STDEV**	**Region (%Fat)**	**STDEV**
Left Arm	33.79	8.97	44.54	8.18	32.36	8.63	14.72	4.64
Left Leg	40.76	17.07	46.12	5.62	39.27	16.52	14.53	4.29
Left Trunk	45.88	8.00	52.89	3.88	44.71	7.82	35.17	4.85
Left Total	42.14	10.13	47.85	4.18	40.66	9.76	20.09	3.62
Right Arm	33.80	8.97	43.25	8.68	32.33	8.65	14.29	5.00
Right Leg	40.80	17.06	49.50	6.28	39.27	16.52	15.07	4.60
Right Trunk	45.81	8.08	54.83	4.20	44.69	7.82	37.09	4.54
Right Total	42.18	10.11	49.19	4.66	40.72	9.81	20.76	3.69
Arms	34.43	9.85	43.90	8.12	33.00	9.57	14.52	4.76
Legs	39.72	16.56	47.81	5.88	38.24	16.00	14.79	4.43
Trunk	46.12	8.28	53.87	3.49	44.92	7.96	36.22	4.48
Total	**43.39**	**11.09**	**48.52**	**4.30**	**41.78**	**10.72**	**20.43**	**3.63**

Table 7-2 *Overall Mean Results Gathered for all DEXA and MRI Cases Continued*

	DEXA		MRI	
Region	**Tissue (g)**	**STDEV**	**Tissue (g)**	**STDEV**
Left Arm	3864.89	549.17	3780.88	775.95
Left Leg	13694.67	2844.92	18893.88	2870.54
Left Trunk	21193.67	3516.84	18887.63	3526.33
Left Total	40957.44	5277.99	41563.38	5248.42
Right Arm	3901.89	532.80	4026.50	826.93
Right Leg	13639.67	2702.68	18821.38	2911.11
Right Trunk	20857.00	3562.48	19511.75	3986.01
Right Total	38059.11	6636.52	42360.63	5603.63
Arms	12253.22	13732.85	7808.13	1481.77
Legs	24480.22	7759.86	37715.88	5760.74
Trunk	40289.67	6807.34	38399.88	7466.42
Total	**62487.11**	**30792.07**	**83923.25**	**10766.93**

Table 7-3 *Overall Mean Results Gathered for all DEXA and MRI Cases Continued*

	DEXA		MRI	
Region	**Fat (g)**	**STDEV**	**Fat (g)**	**STDEV**
Left Arm	1295.67	349.65	1689.19	491.49
Left Leg	5869.22	3034.16	8775.42	2067.77
Left Trunk	9694.22	2165.96	10037.05	2205.67
Left Total	17310.00	4896.12	20456.55	3404.17
Right Arm	1312.56	370.55	1733.57	494.15
Right Leg	5840.33	2973.66	9382.17	2270.75
Right Trunk	9556.67	2215.97	10741.28	2501.53
Right Total	15949.00	4536.77	21703.00	3410.72
Arms	4871.56	7099.52	3422.89	932.23
Legs	10148.11	6081.20	18155.84	4325.52
Trunk	18478.67	3855.30	20779.10	4607.40
Total	**25757.78**	**14124.92**	**42160.44**	**6738.44**

Table 7-4 *Overall Mean Results Gathered for all DEXA and MRI Cases Continued*

	DEXA		MRI	
Region	**Lean (g)**	**STDEV**	**Lean (g)**	**STDEV**
Left Arm	2568.89	569.06	2091.31	478.21
Left Leg	7825.67	1591.40	10006.58	1372.97
Left Trunk	11499.11	2704.35	8850.08	1551.40
Left Total	23647.44	4906.55	21106.45	2191.44
Right Arm	2589.11	553.58	2292.68	579.91
Right Leg	7779.11	1514.33	9438.96	1409.88
Right Trunk	11300.22	2617.39	8769.85	1773.85
Right Total	22110.11	5879.70	20655.87	2695.37
Arms	7407.67	6711.33	4384.73	983.72
Legs	14332.89	4715.52	19559.53	2753.62
Trunk	21811.00	5635.35	17620.28	3187.39
Total	**36729.33**	**20535.72**	**41763.56**	**4835.86**

Table 7-5 *Overall Mean Results Gathered for all DEXA and MRI Cases Continued*

	DEXA		MRI	
Region	**Total Mass (kg)**	**STDEV**	**Total Mass (kg)**	**STDEV**
Left Arm	4.03	0.56	3.77	0.78
Left Leg	14.22	2.85	18.89	2.87
Left Trunk	21.71	3.48	18.88	3.53
Left Total	42.43	5.26	21.96	2.11
Right Arm	4.09	0.54	4.02	0.83
Right Leg	14.18	2.73	18.82	2.91
Right Trunk	21.34	3.54	19.51	3.99
Right Total	39.44	6.93	42.36	5.60
Arms	12.73	14.09	7.80	1.48
Legs	25.46	7.99	37.71	5.76
Trunk	41.32	6.77	38.40	7.47
Total	**64.80**	**31.92**	**83.93**	**10.77**

Table 7-6 *Mean Fat Mass Ratios for all Cases for DEXA and MRI*

DEXA		MRI	
Trunk / Total	**STDEV**	**Trunk / Total**	**STDEV**
0.57	0.11	0.49	0.08
Legs / Total	**STDEV**	**Legs / Total**	**STDEV**
0.32	0.12	0.43	0.07
(Arms + Legs) / Total	**STDEV**	**(Arms + Legs) / Total**	**STDEV**
0.75	0.30	0.51	0.07

From the DEXA results the total percentage of fat for each patient (see Figure 7-1) and the total amount of fat in grams alongside the total mass in grams for each patient (see Figure 7-3) have been graphed to give an overview of the distributions among cases. It is important to note that of the nine patients scanned, only one fell into the normal body mass index (BMI) range (between 18.5 and 24.9, see Table 6-2) while the majority of patients recorded BMI values categorised as obese. In regards to the MRI data gathered, the increased weight of many of the patients affected both the quality of the scans and the results calculated from the data. This is discussed in more detail in section **Error! Reference source not found.**.

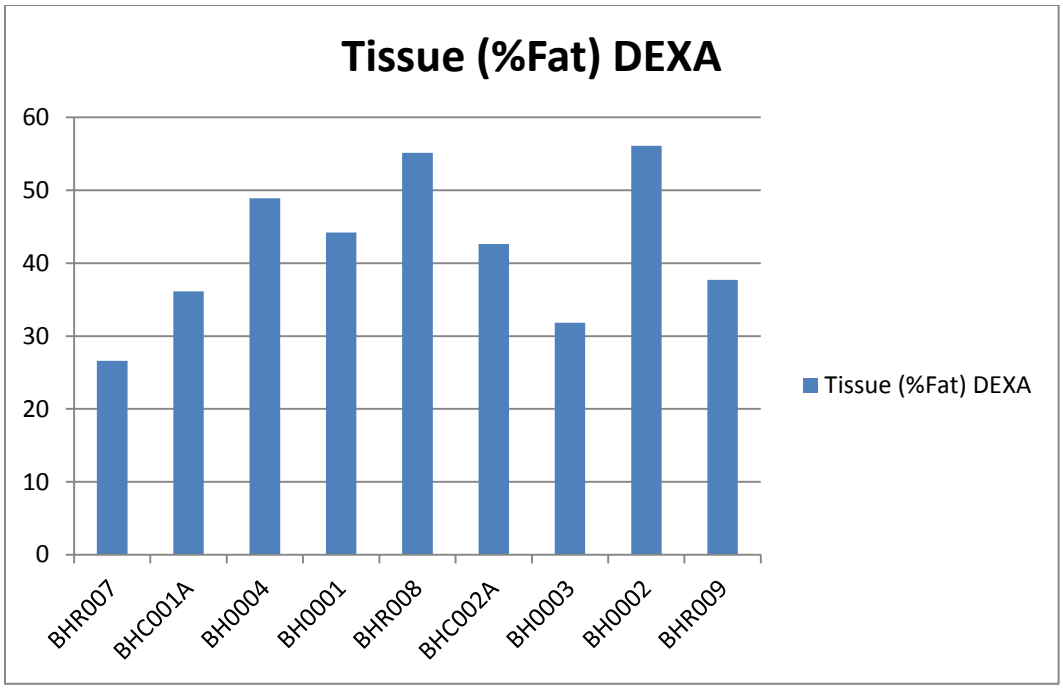

Figure 7-1 *DEXA, Total % of Fat for all Cases*

As with the DEXA data, Figure 7-2 and Figure 7-4 presents the total percentage of fat present and the total fat in grams versus total mass in grams for each patient.

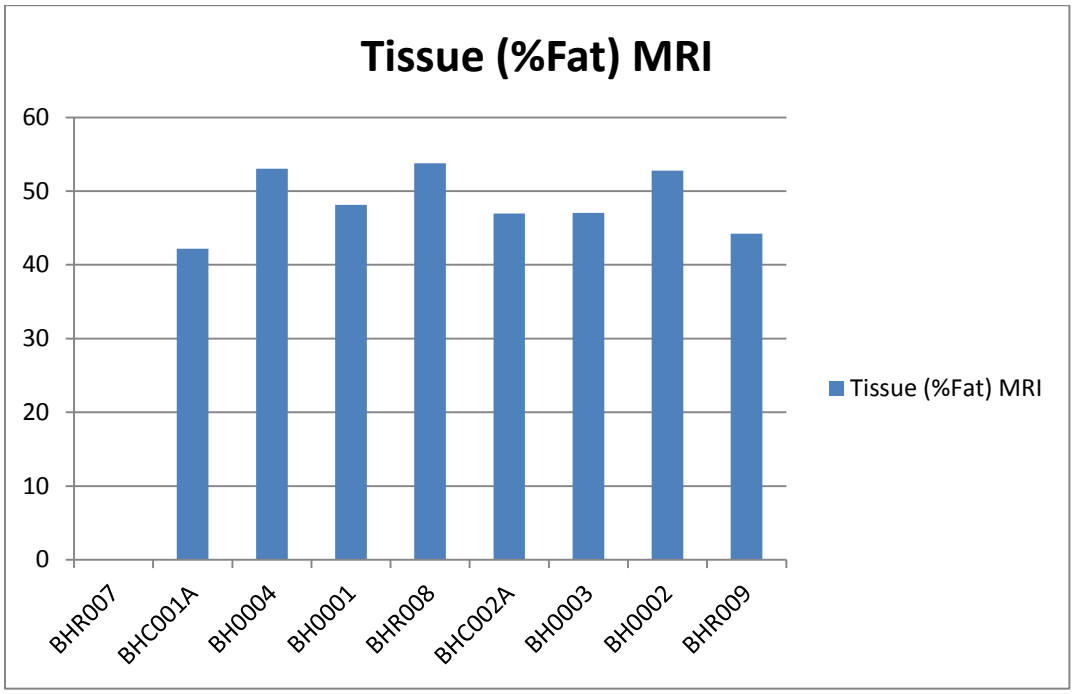

Figure 7-2 *MRI, Total % of Fat for all Cases*

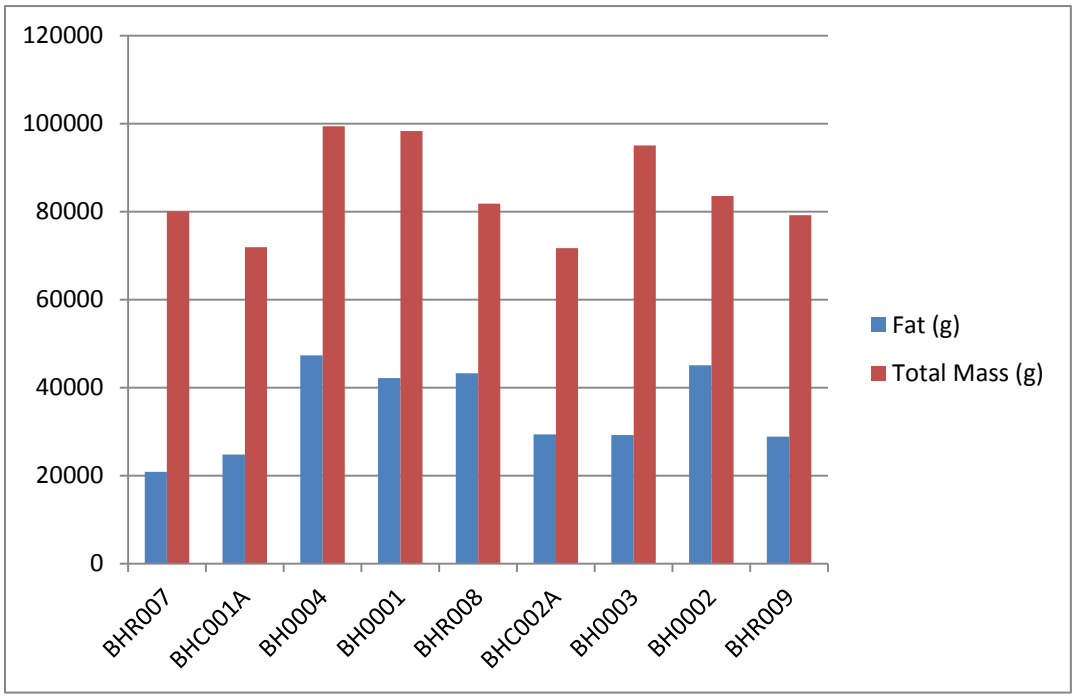

Figure 7-3 *DEXA, Total Fat and Total Mass (in grams) for all Cases*

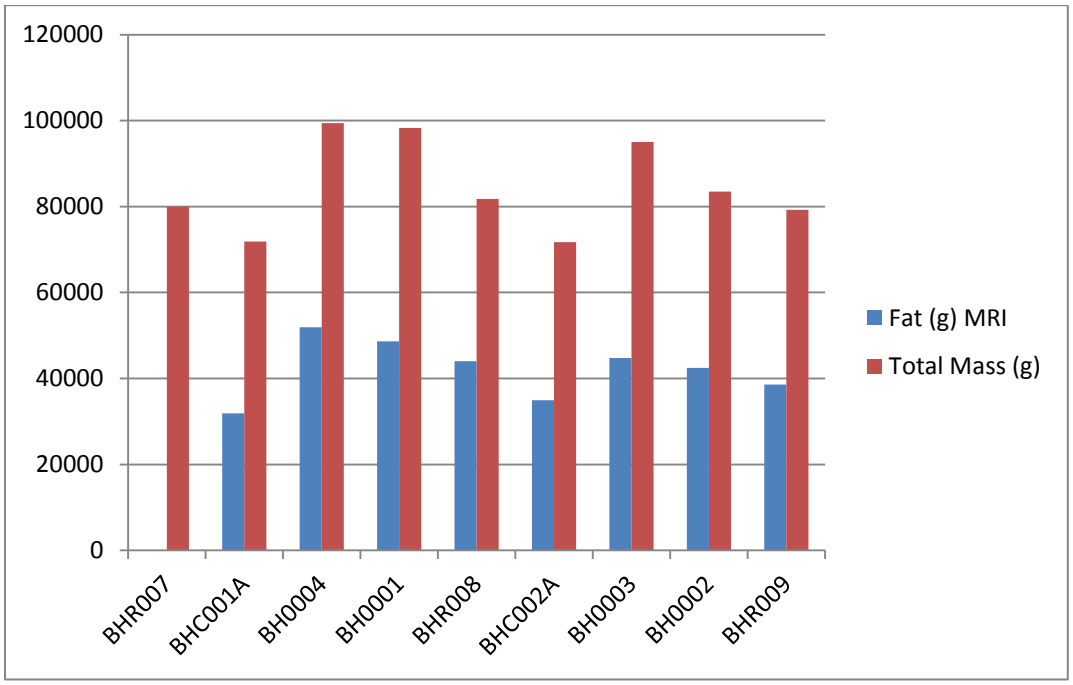

Figure 7-4 *MRI, Total Fat and Total Mass (in grams) for all Cases*

Before performing any statistical analysis on the data gathered visualisation of the raw data gathered can give a visual indication as to the differences/similarities of the results of the two methods being compared. In Figure 7-5 it can be seen that the total percentage of fat in each patient for both modalities. It can be clearly seen that in the majority of cases the MRI results are slightly higher than those from DEXA. The case of most interest is BH0003, where there is a significant difference between the DEXA and MRI results. The effect on statistical analysis and the possible cause of this will be examined in section 7.3. The mean difference between the results of the two modalities is 5.62%.

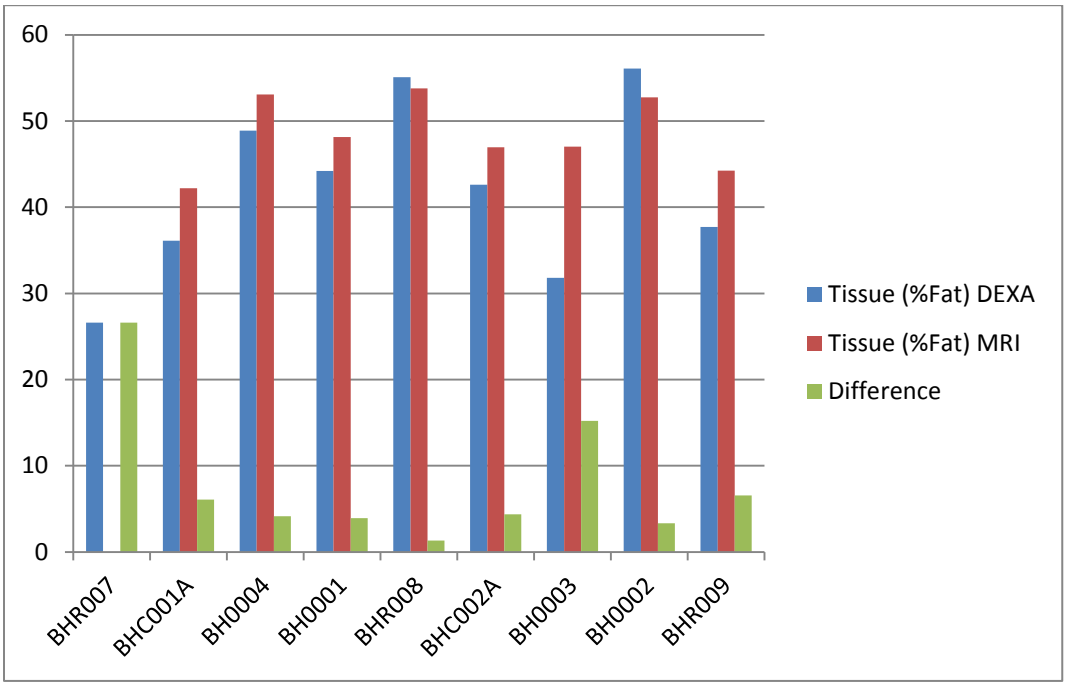

Figure 7-5 *Comparison of Total Fat (%) of DEXA and MRI for all Cases*

As with the previous figure, in Figure 7-6 it can be seen that the total results fat in grams for both modalities. As would be expected, the results match up very closely with the percentage results (MRI presenting higher results in the majority of the patients). The mean difference between the two modalities in this case is 6569.88 grams. The similarity in results of all cases (except BH0003 in which MRI gives substantially higher results then DEXA) suggests there is a reasonable level of agreement between the two modalities. This is examined in greater detail in section 7.3.

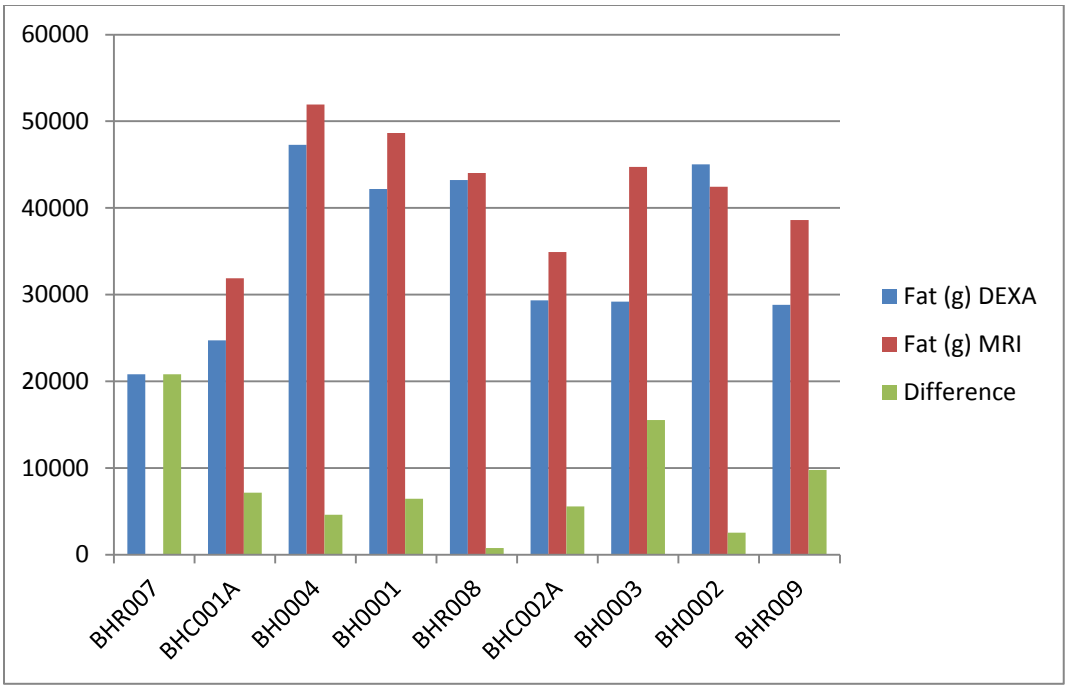

Figure 7-6 *Comparison of Total Fat (in grams) of DEXA and MRI for all Cases*

The following sections describe in detail the results of the statistical analysis techniques used to compare the data gathered from both DEXA and MRI in relation to adipose tissue quantification.

7.2 Pearson's Correlation Coefficient Results

A correlation coefficient was performed on the data gathered from the DEXA and MRI scans. As the primary interest for this piece of research is in the quantification of adipose tissue, the percentage of fat present in each part of the body was used in order to determine whether there was a correlation between the results of the two modalities. For each of the eight patients there were 14 different values gathered (arm fat percentage, trunk fat percentage, total fat percentage, etc.), leading to a total sample size of 112. In Figure 7-7 it can be seen that many of the cases lie along or near the line of equality suggesting a correlation between the two sets of results.

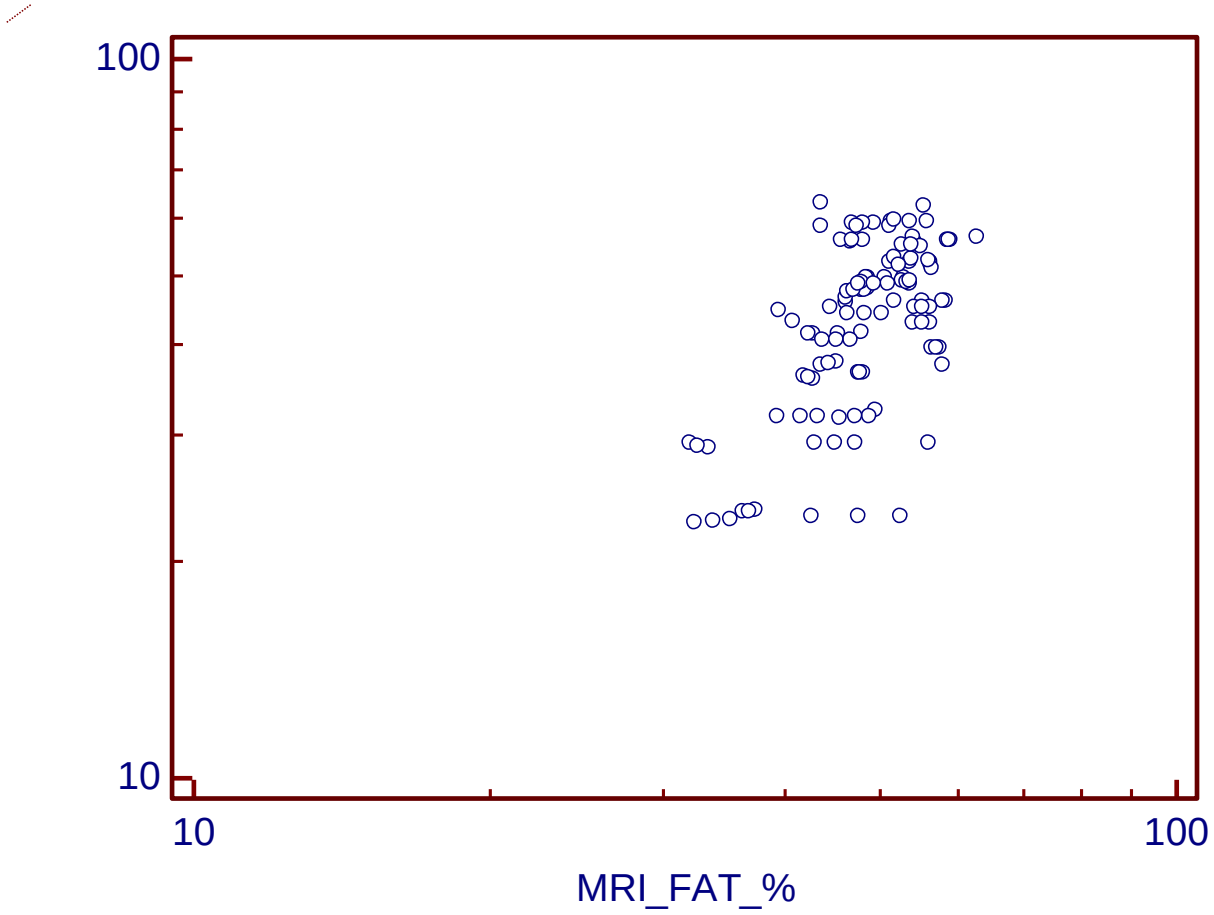

Figure 7-7 *Pearson's Correlation Coefficient for Fat % for all regions*

By looking at the numerical results of the correlation coefficient (see Table 7-7) it can be seen that the *r* value is 0.6968, suggesting a strong correlation between the sets of results. This is further strengthened by a *p* value of less then 0.0001 and a very small confidence interval. Both of these values suggest that the correlation coefficient result is highly statistically significant.

Table 7-7 *Pearson's Correlation Coefficient Results*

Sample size	112
Correlation coefficient r	0.6968
Significance level	P<0.0001
95% Confidence interval for r	0.5871 to 0.7813

While the use of the correlation coefficient has clearly demonstrated that there is a strong positive linear correlation between the results of the two modalities, this does not necessarily mean that there is good agreement between said modalities. In the following section the Bland Altman method is described in detail and is applied to the data in order to establish the level of agreement between the two modalities used.

7.3 Bland Altman Method Results

Through the visual representation of the Bland Altman method using a Bland Altman plot, agreement between two methods can be more easily understood (see Figure 7-8). Each coloured shape in the plot represents one dataset. The upper and lower confidence intervals (±1.96 standard deviations) are represented by red dotted lines. The 95% confidence interval indicates that 95% of the time, the difference between the two methods will fall into this range. The mean is the solid horizontal blue line. If the mean is non-zero then that indicates a systematic bias between the two methods: one method consistently giving higher (or lower) results then the other. The position of points on the y-axis of the plot indicates the amount of difference between

two methods. Points falling above the mean indicate one method would indicate one method scoring higher then the other and vice versa. Points which lie on or very near the mean suggest the two methods are giving similar results.

Figure 7-8 is a Bland Altman plot of the fat percentage for each area of the body. Each group of coloured shapes represents a specific dataset, with the individual shapes representing the result of the comparison of the two modalities for each area of the body. It can be clearly seen that most of the points fall above the mean and are generally quite closely clustered. This suggests that most of the results tend to be in agreement. The fact that the mean is far from zero suggests that one method is consistently scoring higher then the other. This is confirmed in Figure 7-5, where it can clearly be seen that MRI is giving higher results then DEXA in six out of 8 cases. While the confidence interval is quite large (between 11.25 and -21.29) this could be due to outliers and therefore each dataset needs to be examined independently. What is of great interest is the clearly noticeable outlier dataset, specifically the orange triangles in the lower left-hand corner of the plot. These represent dataset BH0003, which as stated in section 7.1 was the only dataset to have a significant difference in results between DEXA and MRI. In the following Bland Altman plots comparing specific areas of the body, the fact that this dataset is an outlier can be more clearly seen.

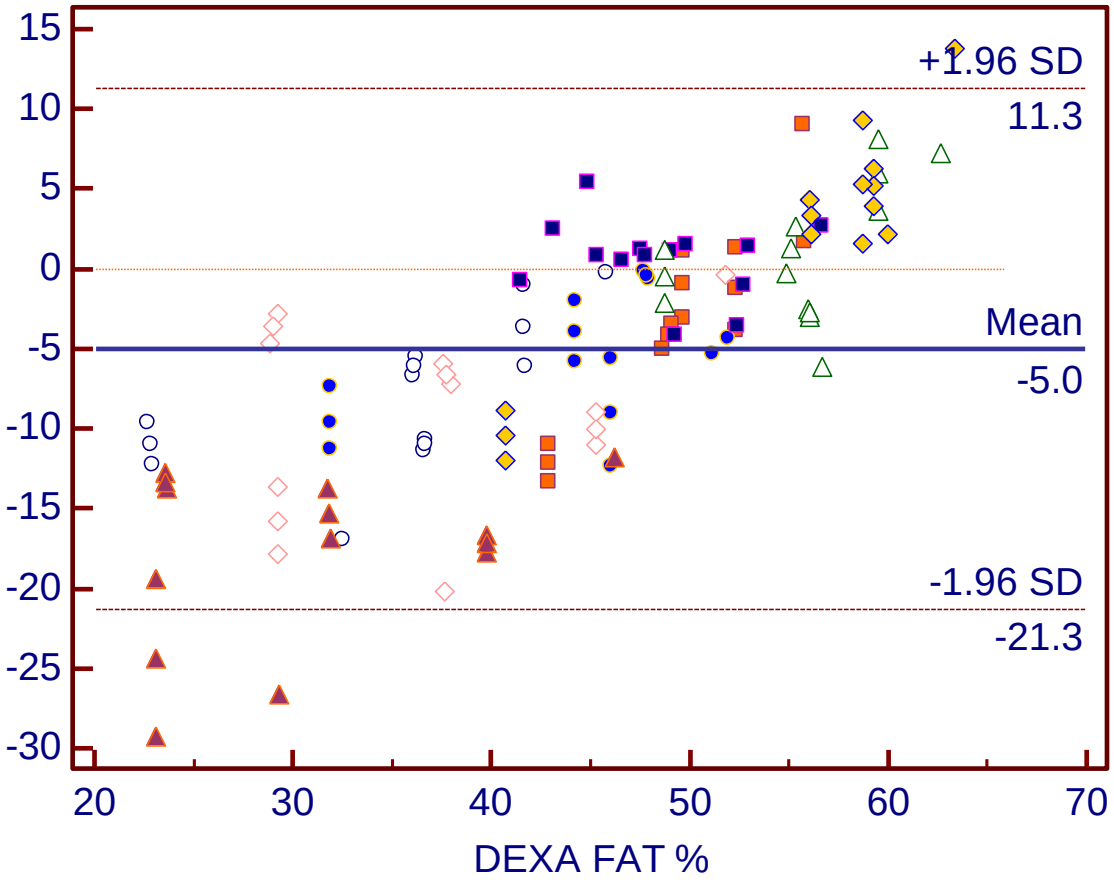

Figure 7-8 *Bland Altman Plot Percentage of Fat Present for all Cases*

Table 7-8 *Bland Altman Plot Results*

Sample size	112
Arithmetic mean	-5.0163
Standard deviation	8.3010
Lower limit	-21.2864
Upper limit	11.2537

When examining the level of agreement for the quantification of adipose tissue in the arm region (see Figure 7-9) it is made even clearer that the results gathered for dataset BH0003 are significantly different in there level of agreement to the other datasets. The majority of the datasets fall on or near the mean suggesting more consistent agreement between the methods.

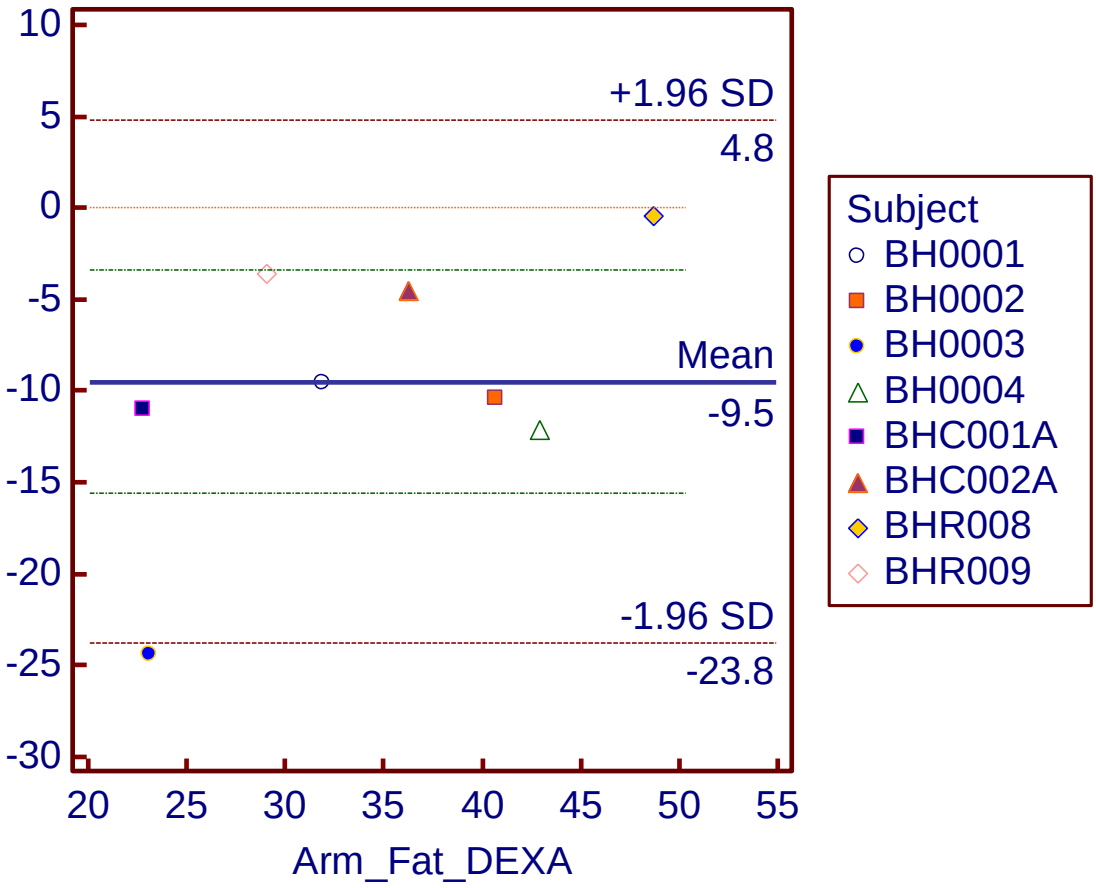

Figure 7-9 *Bland Altman Plot for Arm Fat Percentage for all Cases*

Table 7-9 *Bland Altman Plot Results for Arm Fat*

Sample size	8
Arithmetic mean	-9.4900
95% CI	-15.5873 to -3.3927
Standard deviation	7.2932
Lower limit	-23.7847
95% CI	-34.6836 to -12.8857
Upper limit	4.8047
95% CI	-6.0943 to 15.7036

A similar pattern as with the comparison of arm fat percentage can be seen in Figure 7-10, with dataset BH0003 being a clear outlier. In the case of leg fat percentage it appears there much less agreement between the two modalities. The confidence interval is much larger then the previous plot and only four of the cases are closely clustered near the mean.

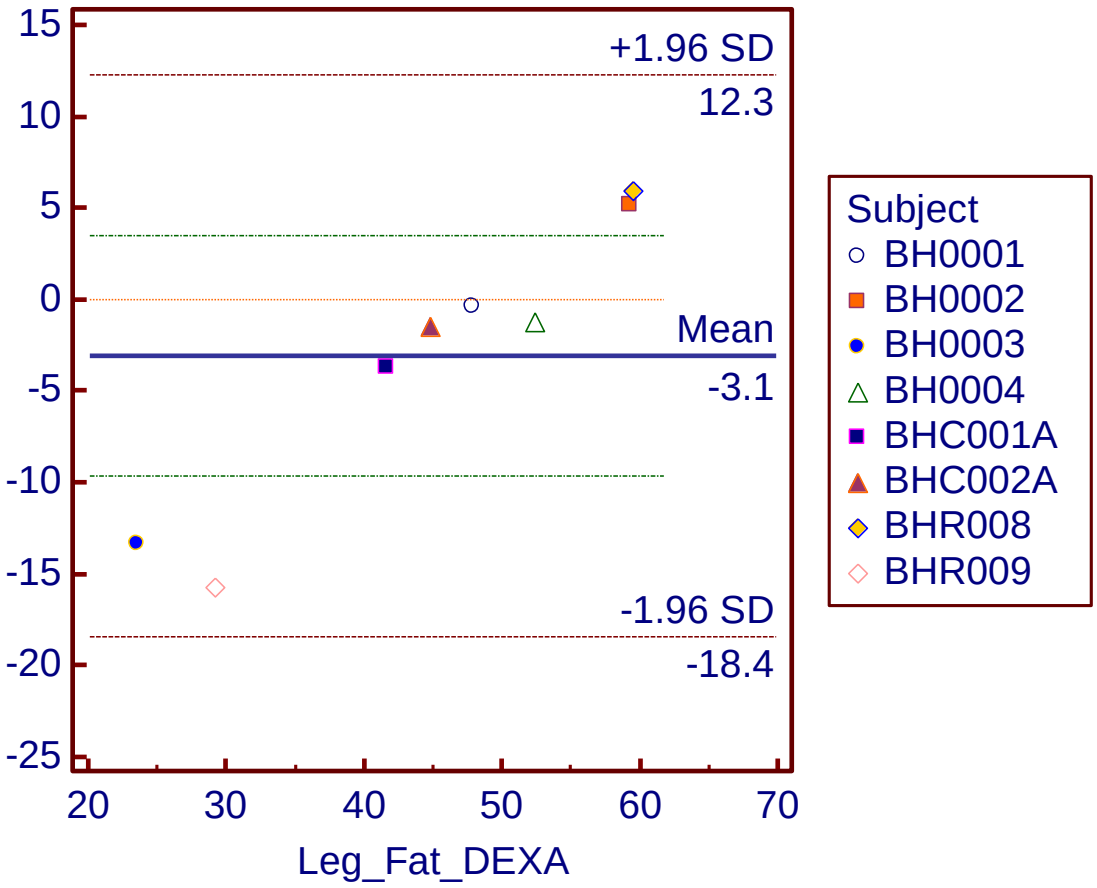

Figure 7-10 *Bland Altman Plot for Leg Fat Percentage for all Cases*

Table 7-10 *Bland Altman Plot Results for Leg Fat*

Sample size	8
Arithmetic mean	-3.0688
95% CI	-9.6145 to 3.4770
Standard deviation	7.8297
Lower limit	-18.4149
95% CI	-30.1155 to -6.7143
Upper limit	12.2774
95% CI	0.5768 to 23.9780

Figure 7-11 shows the Bland Altman plot for the trunk fat percentage. As with the plot of the arm fat percentage, most of the datasets fall near the mean suggesting decent agreement between the two methods. Two of the datasets are clear outliers in this plot, with BH0003 again being one of them and BH0001 being the other. This is the only case where there is more then one outlier. The plot shows that in both cases, MRI measurements for leg fat percentage are significantly higher then DEXA.

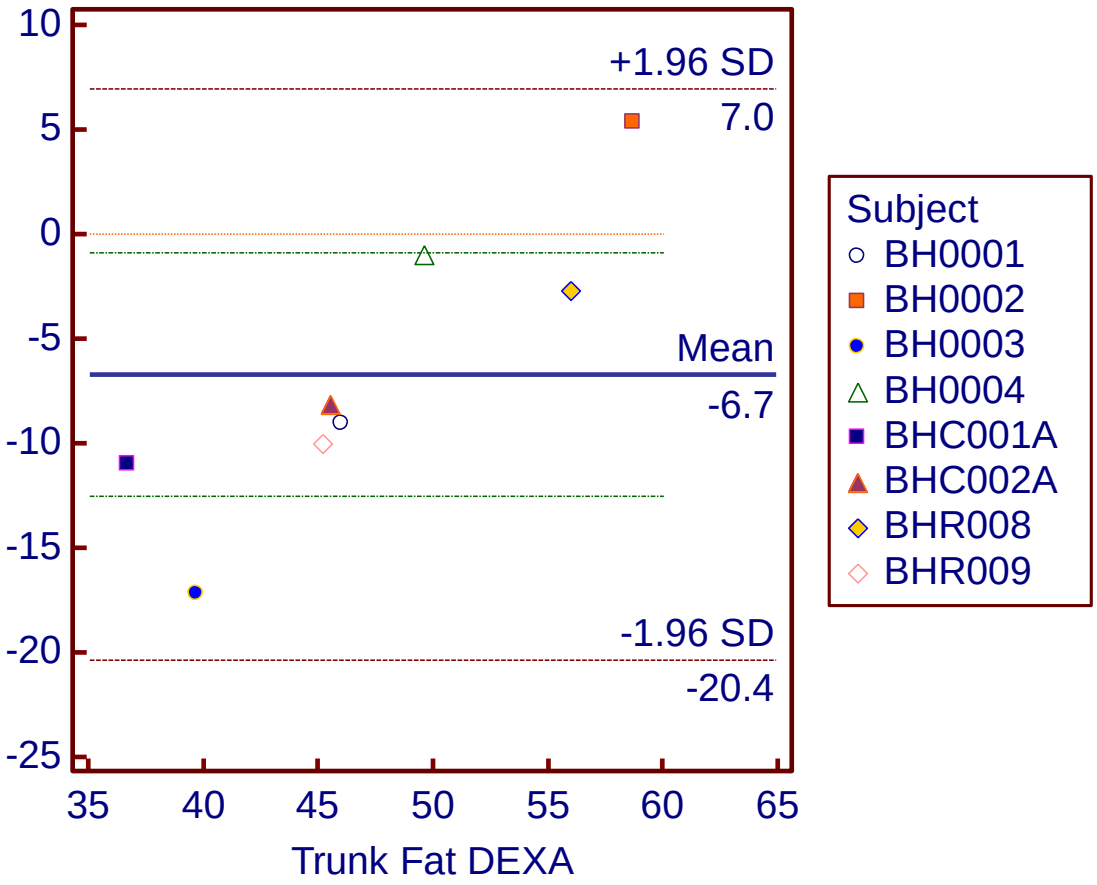

Figure 7-11 *Bland Altman Plot for Trunk Fat Percentage for all Cases*

Table 7-11 *Bland Altman Plot Results for Trunk Fat*

Sample size	8
Arithmetic mean	-6.6975
95% CI	-12.5268 to -0.8682
Standard deviation	6.9727
Lower limit	-20.3640
95% CI	-30.7840 to -9.9440
Upper limit	6.9690
95% CI	-3.4510 to 17.3890

A Bland Altman plot of the quantification of total fat percentage for each case can be seen in Figure 7-12. As with the previous plots, most of the cases fall near the mean with one case (BH0003) being a clear outlier. The outlier causes the size of the confidence interval in all plots to be quite high, ranging from ~20 to ~30 depending on which portion of the body is being investigated. This suggests that in 95% of the cases the difference between the two methods there is a significant difference between the two methods.

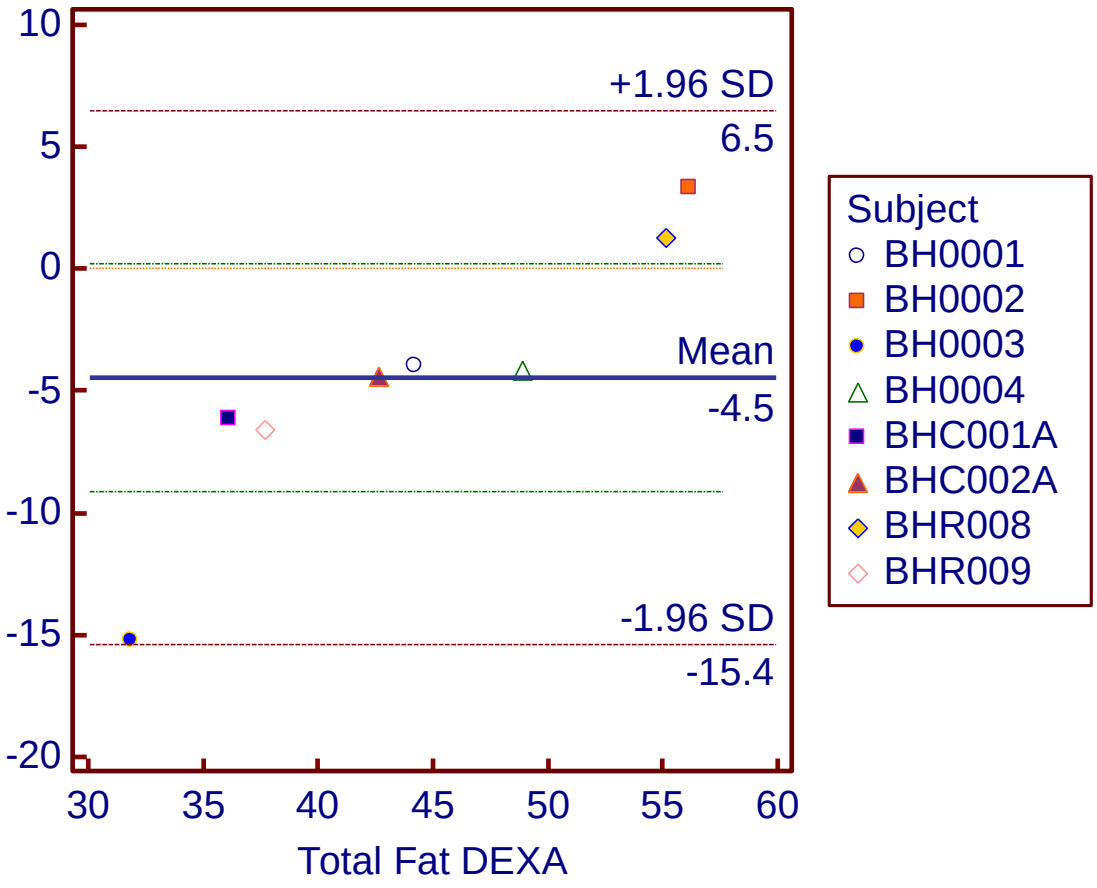

Figure 7-12 *Bland Altman Plot Total Fat Percentage for all Cases*

Table 7-12 *Bland Altman Plot Results Total Fat*

Sample size	8
Arithmetic mean	-4.4588
95% CI	-9.1204 to 0.2029
Standard deviation	5.5760
Lower limit	-15.3878
95% CI	-23.7206 to -7.0550
Upper limit	6.4703
95% CI	-1.8625 to 14.8031

In order to give a clearer picture of the agreement of the two methods and the effect the outlier has on calculating the agreement, a Bland Altman plot of the all cases except the outlier is presented in Figure 7-13. With the outlier removed, the size of the confidence interval reduces in size to ~15 suggesting there is a maximum difference of 15% in 95% if the cases. It can also be noted that five of the seven datasets lie below the mean, indicating they are giving consistently higher results then the gold standard (DEXA). This is confirmed by examining the graphs presented in section 7.1 comparing the gathered results for fat percentage and fat grams present in all cases.

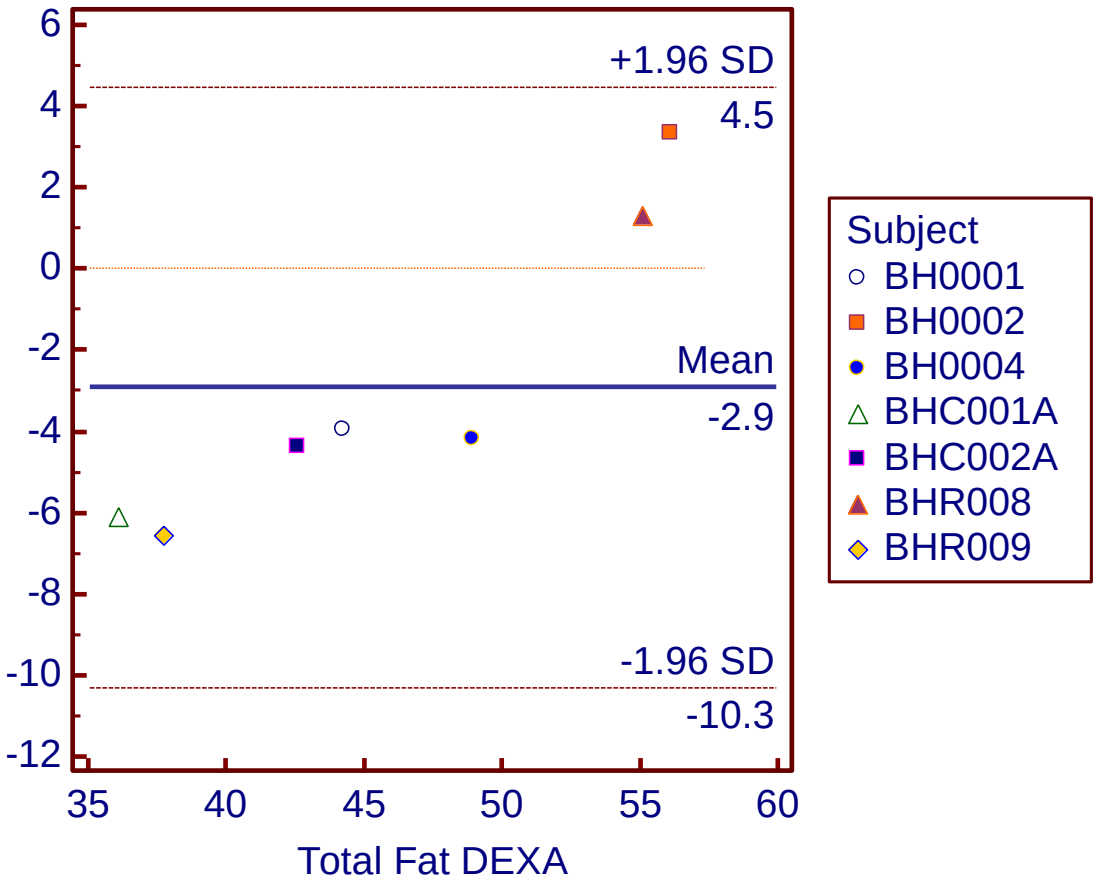

Figure 7-13 *Bland Altman Plot Results Total Fat without Outlier*

Table 7-13 *Bland Altman Plot Results Total Fat without Outlier*

Sample size	7
Arithmetic mean	-2.9200
95% CI	-6.4020 to 0.5620
Standard deviation	3.7650
Lower limit	-10.2994
95% CI	-16.5680 to -4.0308
Upper limit	4.4594
95% CI	-1.8092 to 10.7280

As to why case BH0003 is an outlier is not entirely clear. A visual inspection of the segmented dataset showed no issues such as excessive over or under segmentation when compared with other datasets. The fact that the patient is one of only three Caucasian males from the cohort and at least 10kg heavier then the other two may have had an effect on the results. Alternatively the patent may have been unknowingly incorrectly scanned with DEXA. The only way to determine whether an error has occurred by either modality (or quantification technique) would be to have the patient rescanned and compare the results. Due to the limitations of this study, that is not currently a possibility.

The results of the Bland Altman analysis indicate, with the exception of one outlier, that MRI compares well with DEXA in regards to quantifying adipose tissue through various regions of the body.

7.4 Segmentation

Once the datasets had been segmented, it was important to ensure that the segmentation was accurate. The following section describes in detail how the assessment of the automatic segmentation technique applied in this piece of research.

7.5 Qualitative Assessment of Segmentation

Figure 7-14 shows an example of the segmentation survey in which the participants took place. Each image was accompanied by instructions for grading (on the left-hand side of the images) and a box for inputting their grade (on the right-hand side of the images).

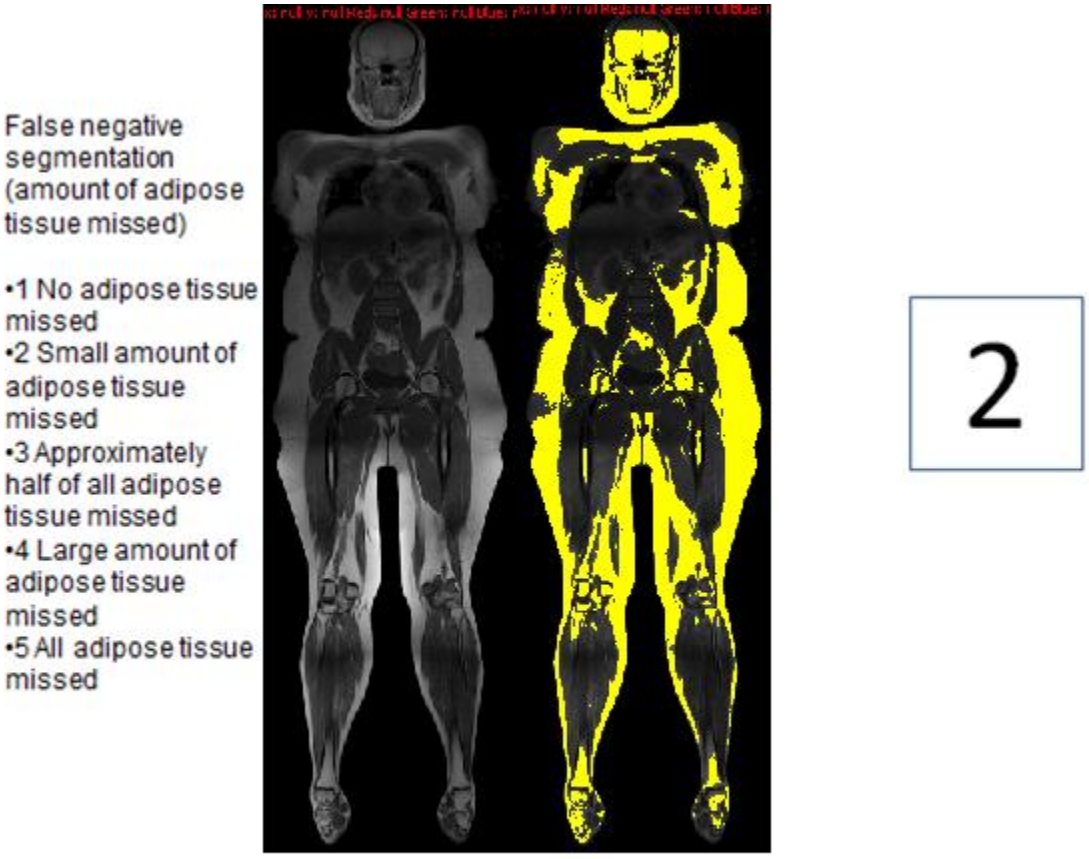

Figure 7-14 *Segmentation Evaluation Example*

Table 7-14 presents the mean rating each participant gave all 11 images for FN, FP and TP respectively. For FN the overall mean rating was 1.48, which indicates that in general the raters scored the images as either having missed no adipose tissue or a small amount of adipose tissue. For FP the overall mean rating was 1.52, indicating the raters scored the images as either having segmented no non-adipose tissue or a small amount of non-adipose tissue. Finally, the overall mean score given for TP was 4.5, indicating the raters scored the images as either having segmented all adipose tissue correctly or most of the adipose tissue correctly. The raters results indicate that the segmentation technique used in this piece of research was acceptable.

The following describes the raters which took part in the evaluation:

- Rater 1 - MSc MRI Radiography Specialist
- Rater 2 - Radiologist
- Rater 3 - PhD Medical Imaging MRI Specialists
- Rater 4 - Radiologist
- Rater 4 - MSc MRI Radiography Specialist
- Rater 6 - MSc MRI Radiography Specialist
- Rater 7 - PhD Medical Imaging MRI Specialist

Table 7-14 *Mean Score for Each Rater*

	Rater 1	Rater 2	Rater 3	Rater 4	Rater 5	Rater 6	Rater 7
FN	1.27	1.27	1.27	1.54	1.54	2	1.45
FP	1.27	1.54	1.81	1.63	1.72	1.45	1.18
TP	4.72	4.54	4.36	4	4.63	4.36	4.90

Table 7-15 presents the mean score all raters gave for each individual image. As with the mean score for each rater, the results for each image indicate that that raters found the segmentation technique to be accurate.

Table 7-15 *Mean Score for Each Image*

	FN	FP	TP
Image 1	1.57	1.42	4.14
Image 2	1.42	1.57	4.42
Image 3	1.71	1.28	4.28
Image 4	1.57	1.42	4.57
Image 5	1.57	1.57	4.42
Image 6	1.71	1.28	4.71
Image 7	1.42	1.42	4.57
Image 8	1.42	1.57	4.71
Image 9	1.42	1.57	4.71
Image 10	1.14	1.71	4.57
Image 11	1.28	1.85	4.42

Establishing that the method used for segmentation is accurate is important for justifying any analysis done on the results of said segmentation. All scores given by the raters can be found in Appendix D.

7.6 Visualization

At group meetings with the primary clinician involved with this study, the results of volume visualization were presented. While the clinician found the visualization techniques implemented in the software tool interesting, it was indicated that it was not necessarily clinically relevant at the time of evaluation. The visualization techniques used in this study had two aims; presenting the distribution of fat throughout the body in an intuitive and simple manner and the comparison of full body renderings of individual patients from MRI scans taken over an extended period of time (would be useful in identifying changes in external morphology related to the condition). The clinician indicated they were more interested in the numerical data gathered regarding fat distribution (as this is the way the current modality presents its data) and due to the time constraints associated with this study the second aim could not be realised. A great deal of time was initially spent implementing and testing a number of different methods of visualization but, based on clinical feedback, focus was shifted primarily to the quantification aspect of the study.

7.7 Software Tool Performance

As stated in previous chapters, due to the size of the datasets gathered for this study, manual or even semi-automatic segmentation techniques would be too time consuming and labour intensive to be effectively used in this type of study. In order for the software tool developed to be of any significant use in a clinical setting, it must be able to process and return results within a reasonable time. It was for this reason that a fully automatic segmentation technique was implemented and that all the processing steps were multithreaded. On average the time taken to load a one of the dataset gathered for this study (from selecting the folder containing a DICOM series, to having all images and results available for viewing) is around one minute. Due to the

size of the datasets, the numerous processing steps that need to be taken and the computational cost of visualizing such large datasets, this was felt to be an acceptable amount of time.

7.8 Chapter Summary

In this chapter the results gathered from the evaluation of the software tool were presented. The following chapter covers the findings of this research in relation to previous studies, the clinical limitations discovered during the period of research and the conclusions and future works regarding the research as a whole.

8 Discussion

8.1 Findings in Relation to Previous Studies

As discussed in section 2.1.1, a study published in 2008 compared the fat measurements of MRI and DEXA for HIV+ subjects. A number of significant differences between that study and this one were found. The scan axis used for the MRI dataset in the study was transverse while in this one the coronal axis was used. During the initial formulation of the imaging protocols for this study the project advisers in MRI felt it would be impractical and too time consuming to perform full body imaging with transverse slices. Patient weight was also significantly different. The average weight of patients from the 2008 was 75.35kg while the average for this study was 84.9kg with only two patients who were below 80kg. This could be due to a difference in ethnicity between the two cohorts. The segmentation of adipose tissue was also noted as a major difference between the two studies. Due to the fact that the previous study used semi-automatic segmentation with a third party software tool and there is no evaluation regarding the accuracy or repeatability of the segmentation results it would be problematic to compare the results against those collected using the fully automatic segmentation technique implemented for this study. With regards to DEXA, the fact that the two studies used different DEXA machines (with the previous study using multiple different machines) also makes a direct comparison of statistical results unfeasible.

Both studies did find a strong correlation between the two modalities but differ in the overall conclusion regarding the difference in measurements from DEXA and MRI. The previous study found that in most cases DEXA estimated higher levels of fat then MRI. In contrast, the findings of this study showed that MRI estimated higher then DEXA in the majority cases.

The differences in methodologies and cohort size would be the most likely causes for differing results between the two studies but it is still of interest that both studies indicate a good relationship between measurements taken by the two modalities of interest. This further indicates the potential clinical application of the developed software for the accurate quantification of adipose tissue.

8.2 Clinical Limitations

Patient weight proved to be issue in many areas of this study. As stated previously a number of the patients involved in the study had issues with the MRI scanning stage due to their increased weight but this increased weight also affected the quality of the datasets gathered. During the evaluation period of this study, it was found that the datasets of larger patients did not segment as well as others. It was noted that towards the centre of a dataset (near the middle slice) the segmentation algorithm failed to successfully segment adipose tissue in the abdomen and upper chest (see (a) in Figure 8-1). This was due to a substantial drop in intensity values in that region of the dataset. With patients with a high BMI (especially those in the obese range) this effect was clearly visible. In order to overcome this, a second iteration of the segmentation algorithm had to be performed specifically targeting the abdomen and chest. In the majority of cases this succeeded in successfully segmenting that part of the body but in some of the datasets where the subject was very large a proportion of the adipose tissue in this region was still not segmented (see (b) in Figure 8-1).

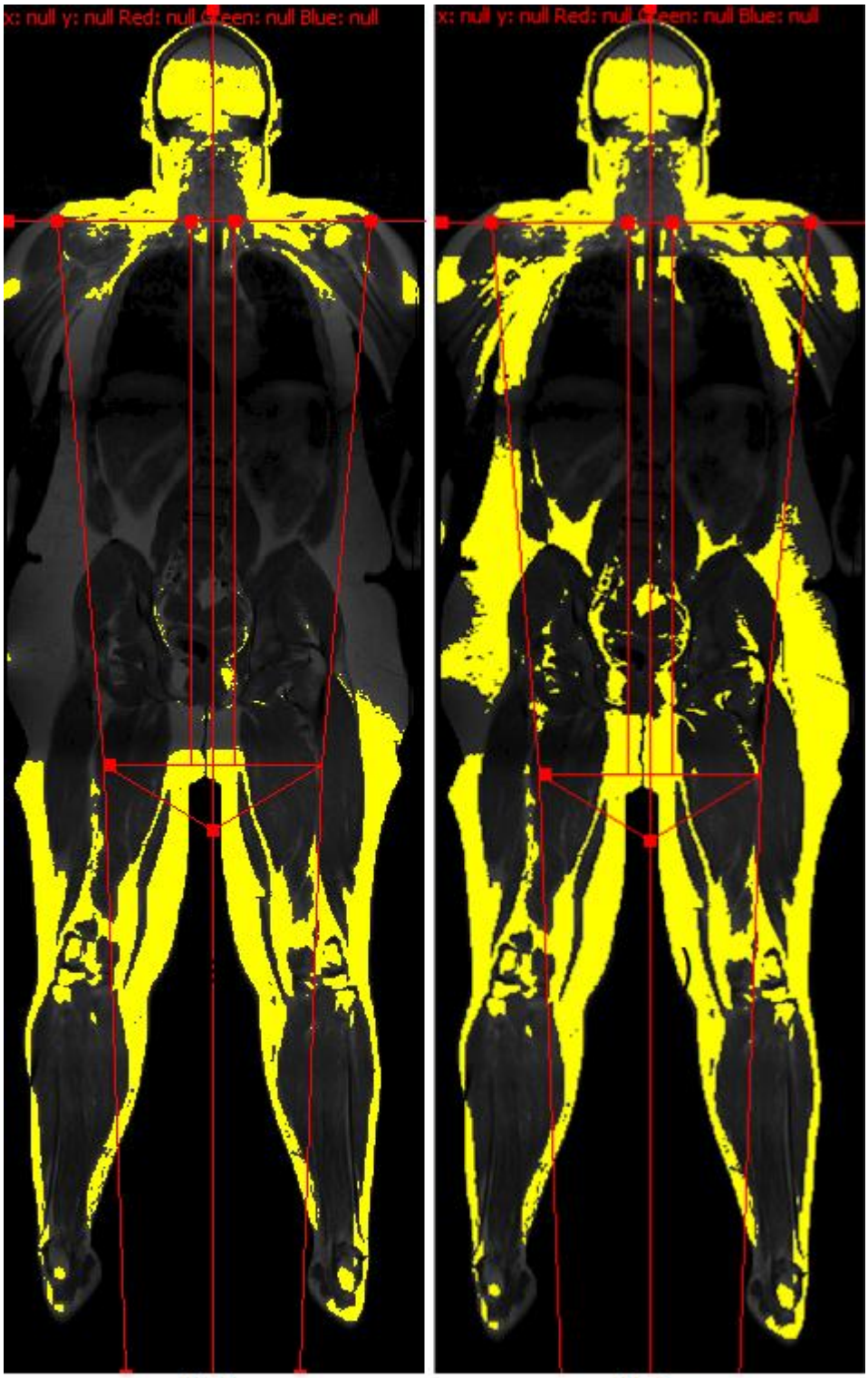
(a)
(b)

Figure 8-1 *Example of the Effects of Patient Weight on Segmentation; (a) segmented slice showing un-segmented areas in the abdomen and chest regions and (b) segmentation results after an extra iteration of the algorithm in those specific areas. Adipose Tissue highlighted in yellow*

Due to the time limitations associated with this study, only one MRI protocol was tested. Testing different protocols (such as changing the scan axis or slice thickness) may provide better imaging results with larger patients. Alternatively, the use an open MRI scanner may also overcome the difficulties associated with patient weight and scanning (it would allow for more obese patients to be scanned) and further investigation as to the cause of the drop in intensity values towards the centre of datasets for obese patients would be of interest. Despite the issues with weight and the quality of the MRI datasets the findings still correlated with DEXA.

8.3 Research Summary

This thesis described the development of a proof of concept software tool which could be used as an alternative to the current standard modality (DEXA) for the evaluation of HIV-associated lipodystrophy using full body MRI datasets. The primary features of the software tool are accurate and reproducible automatic adipose segmentation, presentation of fat distribution in a similar method to that of the currently used modality and volume visualization of both the external morphology of patients and the distribution of fat throughout a patient's body.

In chapter 2 a review of the pertinent literature relevant to this project is presented to primarily identify and review the methodologies relevant to the segmentation, quantification and visualization of adipose tissue. The key components of adipose segmentation were identified as accuracy and reproducibility. In order to achieve these aims a fully automatic segmentation method was implemented as part of the software tool. Based on clinician feedback, the quantification of adipose tissue and how the results of quantification were presented was based strongly on the techniques used by DEXA (implementation of DEXA-style cut lines and presentation of fat distribution in a similar method to DEXA). Finally, using volume visualization techniques, the software tool allows clinicians to view the external morphology of a patient and the fat distribution throughout the body in a volumetric manner.

Chapter 3 described in detail the graphical user interface developed as part of the software tool. The interface was developed with a number of aims. A simple to use and intuitive interface was identified as an important aspect in order to allow clinicians who may not be very technologically adept to use the software tool with ease. Similarly, the decision to use cross-platform languages, libraries and toolkits was made in order to insure the software could be used on various operating systems as there is no standardized operating system clinicians use.

In chapter 4 the methods and algorithms used during the image processing stages (from the initial stage of loading the DICOMs to finally viewing the segmented images) were covered in detail. A correction method for intensity inhomogeneity (contrast limited adaptive histogram equalization) was implemented as a necessary step for correcting an inherent MRI artefact. A fully automatic segmentation is presented as the next step in the processing stage and the process of quantifying the segmented tissue is also described in detail.

Chapter 5 described in detail the approach taken for volume visualization for the software tool.

In chapter 6, the findings of this project were presented. Evaluation of the segmentation technique used found that it was accurately segmenting the MRI datasets. Statistical evaluation of the results gathered from both MRI and DEXA with regards to fat distribution indicated a strong correlation between the two imaging modalities (as found in [16]) and showed that in most cases the two methods agree and give relatively similar results. Feedback from clinicians indicated that, while interesting, the volume visualization of patients was not necessarily clinically useful.

8.4 Conclusions

This thesis is the culmination of a translational medicine research project which involves the merging of computer science and clinical medicine in order to facilitate clinicians with a tool which could be used to assess HIV-associated lipodystrophy using MRI data.

For the completion of this project, the principle components of the five objectives outlined have been successfully achieved. A software tool has been developed which allows accurate

segmentation of adipose tissue from full body MRI datasets, volume visualization of both datasets and fat distribution and a clinically relevant metric for quantifying fat distribution.

A small patient cohort (n = 9) of HIV+ patients, predominantly females, was recruited to undergo DEXA and MRI imaging in order to evaluate the developed tool.

A number of validation strategies were undertaken in order to assess the software tool compared to the current method used to evaluate HIV-associated lipodystrophy. The principle findings which arose from the validation stages are:

- Based on expert opinion (n = 7) the segmentation technique implemented was found to be accurate and 100% reproducible. Due to the fact that it was fully automatic it did not require user interaction and was significantly less time consuming then manual or semi-automatic techniques.

- The quantification of fat distribution generated by the software demonstrated a strongly correlated statistical relationship with those of the existing disease evaluation technique. A correlation coefficient r of 0.68 and significance level of $p < 0.0001$. A mean difference in fat measurements between the two techniques was 5.62%.

- Evaluation of the software tool clearly demonstrated that MRI could be used in place of DEXA for measuring fat distribution to aid in the management and treatment of the condition.

The developed software tool has been evaluated in its current state and provides users with a set of tools to quantify and visualize the distribution of fat throughout the body of patients with HIV-associated lipodystrophy. The results of the evaluation are positive and justify the possibility of a larger and more in depth clinical trial to further strengthen the results of statistical analysis.

8.5 Limitations and Future Works

The development methodologies and the completed software tool have achieved the principal aims and objectives of this research. However a number of limitations were identified during the evaluation stage.

8.5.1 Limitations

The increased weight and body mass index of the patients available for recruitment for this study proved to be an issue with regards to MRI scanning. It was noted that as the weight of a patient increased the quality of images produced by MRI degraded in specific areas. Towards the centre of the datasets in the region of the upper chest it was found that tissue intensity values were much lower then in other areas of the within the same slice of data. In some cases this hampered the results of segmentation with thinner patients presenting with much better segmentation results. It was also noted by the clinicians involved that at least one patient could not physically enter the MRI scanner due to their weight (and were subsequently removed from the cohort) and that a number of other patients had difficulty entering and comfortably staying in the scanner also due to their weight.

Recruitment of cases was difficult as the overall patient numbers attending the HIV/AIDS unit are reasonably low and several patients declined to participate. Increased patient cohorts from other clinical sites would have involved ethical approval from the individual sites which was not feasible to complete in the time frame of this work. Ethics is currently being applied for to facilitate on-going recruitment for imaging purposes and longitudinal imaging along the patient pathway.

The large size of the datasets collected for this study hampered the volume visualization process. In order to render a full body dataset a reasonably high-end dedicated graphics card is required. It is unlikely a clinician would have access such hardware.

8.5.2 Future Work

Two of the main features identified with regards to the use of MRI for evaluating HIV-associated lipodystrophy as part of possible future work were the ability to quantify fat in the anterior and

posterior regions of the body and the volumetric visualization which can be achieved using MRI data. In a long term study in which patients would be scanned repeatedly over a set period of time, both of these features would be advantageous. The quantification of the anterior and posterior trunk fat could be used to evaluate the progression of the lipodystrophy (especially in relation to increased accumulation of fat in the abdomen dorsocervical region as the condition progresses). Similarly, volume visualization could be used to compare the external morphology of a patient over a period of time, to visually identify changes in fat distribution through the comparison of full body renderings.

Increasing the sensitivity and accuracy of the segmentation would yield even better fat measurements from MRI dataset. Implementation and testing of some of the various modified fuzzy c-means algorithms would be of interest in order to get the best segmentation results available [67, 68].

With regards to volume visualization, implementation of the surface based visualization using modern OpenGL features such as Vertex Buffer Objects (rather then display lists as used in this study) or the implementation of GPU based rendering could substantially increase the performance of the volume visualization.

At present there is the possibility to expand this study in order to further develop the software tool for the purposes of general obesity trails. The researcher will be meeting with a group of clinicians from this field to discuss this potential.

9 Appendices

9.1 Appendix A

Clinical, molecular and genetic characteristics of Buffalo-Hump in HIV-infected patients - a Case:Control Study

Running title: Buffalo Hump Study

Study Investigators:

Principal investigator: Dr. Patrick Mallon
School of Medicine and Medical Sciences,
Catherine McAuley Education & Research Centre
Mater Misericordiae University Hospital, Dublin.

Tel: 017166319
Fax: 017166335
Email: Paddy.mallon@ucd.ie

Co-investigators: Dr Tadhg O'Sullivan, SMMS, UCD
Dr Louise Rainford, SMMS, UCD
Dr John Ryan, University Sydney
Prof Steve Eustace, MMUH
Dr Tara McGinty (Project Leader), MMUH
Dr Colm Bergin, St. James' Hospital, Dublin
Prof. Sam McConkey, Beaumont Hospital, Dublin

Study sites:

Mater Misericordiae University Hospital
University College Dublin School of Medicine and Medical Sciences
Department of Infectious Diseases, Department of Radiology and Clinical Research Centre
Eccles Street
Dublin 7, Ireland.

Tel: +35317166319
Fax: +35317166335

Original protocol date: 5th Oct 2010 **Protocol version:** 1.0
Updated:. **Protocol version:** 1.0

Contents:

1 Protocol Synopsis

Title	**Clinical, molecular and genetic characteristics of buffalo-hump in HIV-infected patients – a case:control study.**
Protocol Number	Version 1.0
Objectives	**Primary Objective:** To compare clinical characteristics and adipose tissue distribution using DXA scan and whole body MRI in HIV-infected patients with and without BH phenotype, matched for age, gender and ethnicity. **Secondary Objectives:** ▪ To investigate mutations within the glucocorticoid receptor gene in HIV-infected patients with and without the BH phenotype using DNA sequencing of the glucocorticoid receptor gene to evaluate for presence of common polymorphisms or mutations that may be over-represented in those with BH. ▪ To investigate expression of glucocorticoid-responsive genes within peripheral blood mononuclear cells in HIV-infected patients with and without the BH phenotype using real-time quantitative PCR. ▪ To compare the reliability of volumetric estimation of adipose tissue distribution using whole-body MRI to that of conventional whole body DXA scanning. ▪ To validate a novel software methodology of adipose profiling and quantification. ▪ To evaluate a novel heat-map visualisation technique for adipose distribution estimation from MRI. ▪ To determine the reliability of whole-body MRI scanning in the volumetric assessment of adipose tissue accumulation over the dorsocervical spine in HIV-infected patients with BH.
Study Design	The study will be a prospective, case:control study. Study participants will be recruited to one of two groups; (a) Antiretroviral-treated, HIV-infected patients with the BH phenotype (b) Antiretroviral-treated, HIV-infected patients without the BH phenotype
Patient Population	HIV-infected subjects (groups A and B) will be recruited from the HIV outpatients clinics at the Mater Misericordiae University Hospital, St James' Hospital and Beaumont Hospital. As this is exploratory research, no prevalence estimates are available to guide sample size but these data will help inform power of any future, prospective studies.
Period of study	6 months

Study assessments	Initial clinical assessments will include history taking and recording of relevant patient demographics, HIV related information including HIV RNA levels (nadir and current) , CD4+ T-cell counts (nadir and current), full ARV exposure history, CDC category of HIV disease stage as well as a general medical history, non ARV related medication history and family history of related diseases of interest. Assessments will include BP, Height, Weight and BMI calculation and the presence or absence of a Buffalo Hump. Plasma and Whole blood EDTA samples will collected and stored for isolation of PBMCs and DNA extraction and analyses. Where not available, samples will be taken for fasting lipid profile, glucose and insulin (from which HOMA-IR will be calculated), cortisol. Body fat distribution will be assessed using whole body MRI and DXA.
Endpoints	Primary Endpoint : Comparison of clinical characteristics and adipose tissue distribution using DXA and MRI imaging techniques in HIV - infected population with and without the Buffalo Hump Phenotype Secondary Endpoints DNA sequencing of the glucocorticoid receptor gene to evaluate for presence of common polymorphisms or mutations that may be over-represented in those with BH. Investigation of expression of glucocorticoid-responsive genes within peripheral blood mononuclear cells in HIV-infected patients with and without the BH phenotype using real-time quantitative PCR. Investigate the reliability of volumetric estimation of adipose tissue distribution using whole body MRI to that of conventional whole body DXA scanning. Use of whole-body MRI scanning in the volumetric assessment of adipose tissue accumulation over the dorsocervical spine in HIV-infected patients with BH and attempt to assess its reliability in doing so.
Data analysis	Differences between groups in measured parameters (both clinical and molecular) will be assessed using appropriate non-parametrical analyses, with between group differences in continuous variables analysed using Wilcoxon Signed Rank and differences in categorical variables analysed using Mann-Whitney tests. $P<0.05$ is considered statistically significant and no correction will be made for multiple comparisons. The prevalence of polymorphisms within the glucocorticoid receptor gene will be estimated and prevalence of both heterozygosity and homozygosity estimated and compared between groups.

2 Introduction

The HIV-associated lipodystrophy Syndrome (HIVLD), well described over the past 15years, is characterised by the progressive selective loss of subcutaneous limb fat with persistent increases in central fat or visceral adipose tissue (VAT), maintained lean mass, insulin resistance, dyslipidaemia and hyperlactaemia (1-3). The prevalence of the HIVLD syndrome varies greatly between countries and treatment centres with prevalence between 14-40% reported. The accumulation of a dorsocervical fat pad known as the Buffalo Hump (BH) occurs in a small subgroup of those with HIVLD and is associated with increased insulin resistance and diabetes mellitus. Its pathogenesis is poorly understood, particularly as to why only certain individuals are susceptible to acquisition of a BH phenotype.

The prevalence of the BH phenotype also varies with studies finding prevalence rates of between 2-13%(1,4). It has largely been regarded as part of the spectrum of changes to adipose tissue distribution seen in those with HIVLD rather than a separate entity. However prior studies have shown that the presence of a BH in HIV positive population was strongly associated with hyperinsulinemia but not with the dyslipidaemia seen in HIVLD (1). This suggests that its pathogenesis may involve mechanisms that differ to those seen in HIVLD without BH, even if it does form part of an overall lipodystrophy syndrome.

HIVLD arises as a result of exposure to antiretroviral therapy (ART) and specifically with the duration of exposure to both protease inhibitors (PI) and the thymidine-analogue nucleoside reverse transcriptase inhibitors (tNRTI), with development of the BH phenotype associated with exposure to both the PI ritonavir and the tNRTI zidovudine (1,5,6).

Traditionally, changes in body composition have been assessed with the use of dual-energy X-ray absorptiometry scanning (DXA) to measure changes in total and regional body fat in response to ART exposure. DXA uses X-rays at 2 energies to determine the bone mineral content and soft tissue content (lean body mass / fat mass) of either the whole body or regions (such as limbs or central abdominal area). DXA has been extensively used in both the monitoring for and diagnosis of HIVLD (7) but it has the disadvantage of being unable to differentiate subcutaneous from visceral fat in those with central adiposity and cannot quantify or characterise BH.

New pilot MRI techniques are under development which may play an important role in monitoring of changes in body composition over time and may prove particularly useful in patients with the BH phenotype. MRI has also been shown to produce datasets with superior contrast between tissues in comparison with other imaging modalities. This increased contrast is particularly noticeable with visceral adipose tissue and subcutaneous adipose tissue (8,9), with new analytical techniques enabling accurate volumetric analysis of compartmental adipose tissue depots, such as that seen in patients with BH. In the last two years we have developed a novel software tool for volumetric quantification and visualisation of adipose tissue from MRI datasets (17-18). The software tool is currently undergoing further development to enable full-body quantification suitable for creating head-to-toe adipose profiles of our HIVLD patients. Figure 1 demonstrates a screen-capture of the current tool and figure 2 shows our novel heat-map method for demonstrating fat-distribution on the outer surface of the patient (MRI thigh section).

In HIV-negative subjects, the Buffalo Hump phenotype is associated with hypercortisolism; the so called Cushings syndrome or Cushings Disease. Similarly, dysregulation of cortisol metabolism has also been implicated in the Metabolic Syndrome, an increasingly common condition characterised by insulin resistance, obesity, visceral fat accumulation, dyslipidaemia, hyperglycaemia and hypertension (12,13). Metabolic syndrome shares clinical similarities with the BH phenotype in HIV-infected patients. However, hypercortisolaemia is not a feature of BH in HIV-infected patients (10-12) and studies in lipodystrophic, HIV-infected subjects have failed to demonstrate characteristics of Cushings disease such as impaired suppression of cortisol by dexamethasone or increased urinary free cortisol (10).

Glucocorticoid action is mediated by the glucocorticoid receptor which is a nuclear receptor that regulates physiological events through activation or regression of target genes involved in inflammation, gluconeogenesis and adipocyte differentiation. Although hypercortisolaemia is not a consistent feature of BH in HIV and patients with HIVLD have unaltered levels of glucorticoid receptors on peripheral blood mononuclear cells (10,14), whether HIV-infected patients with BH have altered cortisol responsiveness has not been determined.

Figure 1.

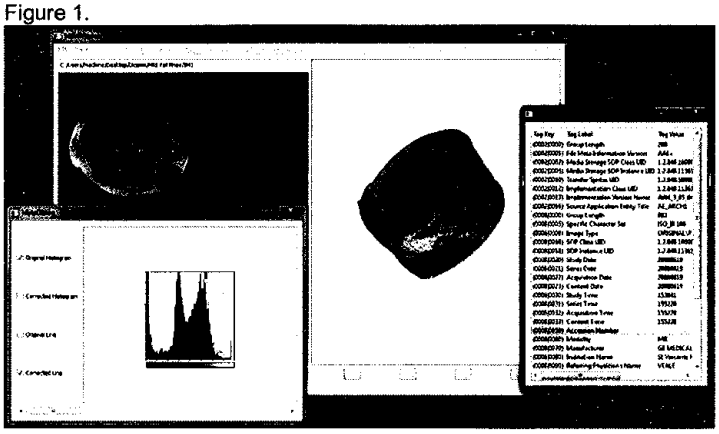

Figure 2.

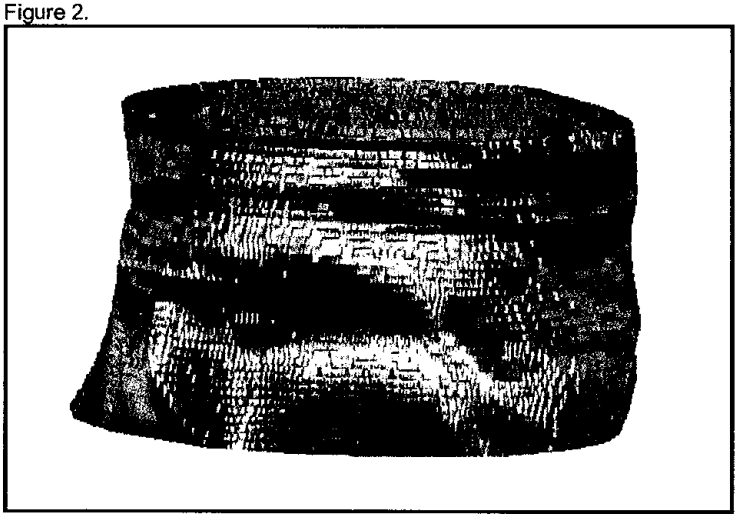

Hyper-responsiveness to cortisol has been observed in certain individuals bearing a mutation in the glucorticoid receptor, which would result in increased receptor/effector coupling and in effect increases the sensitivity of that individual to the effects of glucocorticoids even in the absence of hypercortisolism.

We propose to assess demographic, disease and treatment-related characteristics of patients with BH phenotype in a case:control study with a view to eliciting characteristics that are over-represented in those with a BH phenotype. Furthermore, we will sequence the glucocorticoid receptor to ascertain if mutations in the receptor are more prevalent in those with BH than those without BH and assess expression of glucocorticoid-responsive genes within peripheral blood mononuclear cells.

As the BH phenotype may also occur in the HIV-negative population, we will also compare characteristics of HIV-negative individuals with a BH phenotype to HIV-infected subjects with BH to explore potential different underlying mechanisms behind the pathogenesis of the phenotype between the two groups.

3 Study objectives

3.1 Primary Objective:

To compare clinical characteristics and adipose tissue distribution using DXA scan and whole body MRI in HIV-infected patients with and without BH Phenotype, matched for age, gender and ethnicity.

3.2 Secondary Objectives:

- To investigate mutations within the glucocorticoid receptor gene in HIV-infected patients with and without the BH phenotype using DNA sequencing of the glucocorticoid receptor gene to evaluate for presence of common polymorphisms or mutations that may be over-represented in those with BH.
- To investigate expression of glucocorticoid-responsive genes within peripheral blood mononuclear cells in HIV-infected patients with and without the BH phenotype using real-time quantitative PCR.
- To compare the reliability of volumetric estimation of adipose tissue distribution using whole body MRI to that of conventional whole body DXA scanning.
- To validate a novel software methodology of adipose profiling and quantification.
- To evaluate a novel heat-map visualisation technique for adipose distribution estimation from MRI.
- To determine the reliability of whole-body MRI scanning in the volumetric assessment of adipose tissue accumulation over the dorsocervical spine in HIV-infected patients with BH.

4. Trial Design

The study will be a prospective, case:control study.

Study participants will be recruited to one of two groups;

Group A Antiretroviral-treated, HIV-infected patients with the BH phenotype

Group B Antiretroviral-treated, HIV-infected patients without the BH phenotype

Participants in group B (reference group) will be matched 2:1 to participants in group A (investigational group) for age, gender and ethnicity. Additionally, subjects in group B will be matched to those in group A for CDC stage (A, B or C) and nadir CD4+ T cell count > or < 200 cells/mm3

4.1 Trial Plan

Recruitment will commence 14 November 2010 for a period not longer than 3 months. At this time point arrangement for the necessary imaging to be carried out will be in place. All clinical assessments will be carried out at a single time point following initial screening for eligibility and obtaining informed patient consent. Data will be available and ready for interpretation and analysis by 31/03/11.

4.2 Source of subjects

HIV-infected subjects (groups A and B) will be recruited from HIV outpatients clinics at the Mater Misericordiae University Hospital, St James' Hospital and Beaumont Hospital. HIV negative volunteers with BH will be recruited through affiliated Endocrinology or Obesity related disorders clinics

4.3 Number of Subjects

There will be no maximum enrolment number for the study. At least 2 controls in each of group B will be recruited to match cases (group A)

As the BH phenotype may also occur in the HIV-negative population, we will also compare characteristics of HIV-negative individuals with a BH phenotype to HIV-infected subjects with BH to explore potential different underlying mechanisms behind the pathogenesis of the phenotype between the two groups.

3 Study objectives

3.1 Primary Objective:

To compare clinical characteristics and adipose tissue distribution using DXA scan and whole body MRI in HIV-infected patients with and without BH Phenotype, matched for age, gender and ethnicity.

3.2 Secondary Objectives:

- To investigate mutations within the glucocorticoid receptor gene in HIV-infected patients with and without the BH phenotype using DNA sequencing of the glucocorticoid receptor gene to evaluate for presence of common polymorphisms or mutations that may be over-represented in those with BH.
- To investigate expression of glucocorticoid-responsive genes within peripheral blood mononuclear cells in HIV-infected patients with and without the BH phenotype using real-time quantitative PCR.
- To compare the reliability of volumetric estimation of adipose tissue distribution using whole body MRI to that of conventional whole body DXA scanning.
- To validate a novel software methodology of adipose profiling and quantification.
- To evaluate a novel heat-map visualisation technique for adipose distribution estimation from MRI.
- To determine the reliability of whole-body MRI scanning in the volumetric assessment of adipose tissue accumulation over the dorsocervical spine in HIV-infected patients with BH.

4. Trial Design

The study will be a prospective, case:control study.

Study participants will be recruited to one of two groups;

Group A Antiretroviral-treated, HIV-infected patients with the BH phenotype

Group B Antiretroviral-treated, HIV-infected patients without the BH phenotype

Participants in group B (reference group) will be matched 2:1 to participants in group A (investigational group) for age, gender and ethnicity. Additionally, subjects in group B will be matched to those in group A for CDC stage (A, B or C) and nadir CD4+ T cell count > or < 200 cells/mm3

4.1 Trial Plan

Recruitment will commence 14 November 2010 for a period not longer than 3 months. At this time point arrangement for the necessary imaging to be carried out will be in place. All clinical assessments will be carried out at a single time point following initial screening for eligibility and obtaining informed patient consent. Data will be available and ready for interpretation and analysis by 31/03/11.

4.2 Source of subjects

HIV-infected subjects (groups A and B) will be recruited from HIV outpatients clinics at the Mater Misericordiae University Hospital, St James' Hospital and Beaumont Hospital. HIV negative volunteers with BH will be recruited through affiliated Endocrinology or Obesity related disorders clinics

4.3 Number of Subjects

There will be no maximum enrolment number for the study. At least 2 controls in each of group B will be recruited to match cases (group A)

Where not available from routine testing within the previous 3 months, samples will be taken for fasting lipid profile, glucose and insulin (from which HOMA-IR will be calculated), cortisol.

EDTA blood samples for PBMC isolation and storage will be used for DNA extraction for genotypic analysis of genes involved in cortisol metabolism or lipid metabolism and RNA extraction for analysis of expression of glucocorticoid-responsive genes. Plasma will be stored for later testing for leptin and adiponectin.

5.4 Stored samples

EDTA blood samples for PBMC will be stored from which DNA extraction for genotypic analysis of the glucocorticoid receptor and RNA extraction for analysis of expression of glucocorticoid-responsive genes. Plasma will be stored for later testing for leptin and adiponectin.

All stored samples will be identified by a study code and data linkage to the subjects' medical record number (MRN) will be contained on a password-protected computer file located on a secure research computer network. Patients will not be re-consented prior to further research being performed on these stored samples although prior approval for genetic studies on stored cells will be sought from The Mater Misericordiae University Hospital and Mater Private Hospital Human Research Ethics Committee prior to these experiments taking place. Results from any genetic studies will not be made available to individual patients or their doctors and patient confidentiality will be maintained at all times except where required by regulatory authorities.

6 Assessment of safety

Data from all patients entering the study will be included in the analysis of safety. The number of adverse events (AEs) and serious adverse events (SAEs) will be tabulated by severity and treatment received.

6.1 AEs and SAEs

The investigator is responsible for the detection and documentation of events meeting the definition of AE or SAE as provided in this protocol (appendix F). The investigator will be responsible for detecting AEs and SAEs arising from each period of safety monitoring. The investigator should note an assessment of any SAEs resulting from study participation. The local Research Ethics Committee will be notified of any SAE or AE arising from the study without delay.

7 Data Management, Statistical plan and Interim analysis

All study subjects will be allocated a study number and data will be collected on de-identified case report forms (see appendices). Case report forms will be forwarded to and stored in a locked filing cabinet in the Department of Infectious Diseases, Catherine McAuley Education and Research Centre, Mater Misericordiae University Hospital. Data linkage will be between the subjects MRN and study number on a password-protected file located on a secure network drive in the Department of Infectious Diseases. All study materials will be kept for a minimum of 15 years.

There will be no interim analysis. Data will be transferred from case report forms to an electronic database for final analysis.
Final statistical analysis will take place once all consented patients have undergone all study assessments or withdrawn from the study.

7.1 Statisitical Analyses

Differences between groups in measured parameters (both clinical and molecular) will be assessed using appropriate non-parametrical analyses, with between group differences in continuous variables analysed using Wilcoxon Signed Rank and

differences in categorical variables analysed using Mann-Whitney tests. $P<0.05$ is considered statistically significant and no correction will be made for multiple comparisons.

The prevalence of polymorphisms within the glucocorticoid receptor gene will be estimated and prevalence of both heterozygosity and homozygosity estimated and compared between groups.

Multivariate regression analysis will be used to correct for potential compounding factors.

7.2 Primary Endpoints

To compare clinical characteristics and adipose tissue distribution using DXA scan and whole body MRI in HIV-infected patients with and without BH Phenotype, matched for age, gender and ethnicity.

7.3 Secondary Endpoints

Secondary Endpoints for evaluation will include but may not be limited to:

Investigation of mutations within the glucocorticoid receptor gene in HIV-infected patients with and without the BH phenotype using DNA sequencing of the glucocorticoid receptor gene to evaluate for presence of common polymorphisms or mutations that may be over-represented in those with BH.

Investigation of the expression of glucocorticoid-responsive genes within peripheral blood mononuclear cells in HIV-infected patients with and without the BH phenotype using real-time quantitative PCR.

Comparison of the reliability of volumetric estimation of adipose tissue distribution using whole body MRI to that of conventional whole body DXA scanning.

Determination of the reliability of whole-body MRI scanning in the volumetric assessment of adipose tissue accumulation over the dorsocervical spine in HIV-infected patients with BH.

Comparison of clinical characteristics and adipose tissue distribution using both whole-body DXA and MRI in HIV-infected patients with BH and HIV-negative volunteers with BH.

8 References

1. Mallon, PW. et al. Buffalo Hump seen in HIV associated Lipodystrophy is associated with hyperinsulinaemia but not dyslipidaemia; J. Acquir Immune Defic Syndr. 2005, 35(2) : p156-162

2. Carr, A. et al. A Syndrome of peripheral lipodystrophy, hyperlipidaemia and insulin resistance in patients recieving HIV protease inhibitors; AIDS. 1998, 12(supp): F51-58

3. Carr, A. et al. A syndrome of lipoatrophy, lactic acidaemia and liver dysfunction associated with nucleoside analogue therapy: contribution to protease inhibitor-related lipodystrophy syndrome. AIDS. 2000, 14(supp): F25-32

4. Carr, A. et al. HIV lipodystrophy Case Definition Study Group. An objective case definition of lipodystrophy in HIV-infected adults: a case-control study. Lancet. 2003: p2893-2899

5. Bernasconi, E. et al. Abnormalities of body fat distribution in HIV-infected persons treated with anti-retroviral drugs: the Swiss HIV Cohort Study. JAcquir Immune Defic Syndr. 2002, 35: p50-55

6. Mallon, PWG. et al. Prospective evaluation of the effects of antiretroviral therapy on body composition in HIV-1 infected men starting therapy. AIDS. 2003, 17: p971-979

7. Abale, N. et al. Estimation of adipose tissue mass by MRI: Validation against dissection in human cadavers. J. Lipid Res. 1994, 35(8): p1490-1496

8. Jin, Y. et al. Segmentation and Evaluation of adipose tissue from whole body MRI scans, Lecture notes in Computer Science. 2003, 287: p635-642

9. Ian, P. Martin. Absence of Hypersensitivity to Glucocorticoids in Antiretroviral Associated Lipodystrophy. Obesity Research. 2003, 11: p21-24

10. Lo, J. et al. Buffalo Hump in Men with HIV-1 Infection. Lancet. 1998, 351: p867-870

11. Wang, M. The role of glucocorticoid action in the pathophysiology of the Metabolic Syndrome. Nutrition and Metabolism. 2005, 2: 3

12. Grundy, SM. et al. Definition of the Metabolic Syndrome: Report of the National Heart, Lung and Blood Institute/American Heart Association conference on the scientific issues related to the issue. Circulation. 2004, 109(3): p433-438

13. Bamberger, CM. et al. Molecular Determinants of Glucocorticoid Receptor and tissue sensitivity to Glucocorticoids. Endocrine Rev. 1996, 17(3): p245-261

14. Shevitz. et al. Clinical perspectives in HIV associated Lipodystrophy Syndrome an update. AIDS. 2001, 15(15): p1917-1930

15. Wagenkacht, LE. et al. Insulin sensitivity, Insulin secretion and abdominal fat: The Insulin Resistance Atherosclerosis Study. Diabetes. 2003, 52: p2490-2496

- 17. T O'Sullivan, J Ryan, P Doran, P Mallon, S J Eustace, E Kavannagh, L Rainford, P Brennan (2010) An Application for the Visualization and Quantification of HIV-Associated Lipodystrophy from Magnetic Resonance Imaging Datasets. Mathematics and Visualization. Berlin: Springer
- 18. T O'Sullivan, J Ryan, P Doran; P Mallon, S J Eustace, E Kavannagh et al. (2009) Automatic Segmentation and Visualization of Adipose Tissue from Magnetic Resonance Imaging Datasets. Radiological Society of North America (RSNA) Chicago

Appendix A - Sample Patient Information Statement and Consent Form

Appendix B - Instructions for measuring height and weight.

General guidelines:

Height and weight should be measured at relevant study visits under the following conditions:

Weight:

Subjects should be fasting for at least ten hours (other than small amounts of water) for all measurements of weight and body composition.

Subjects should be weighed, wearing only a hospital gown, underwear and socks. All other clothing, including shoes, should be removed.

Subjects should be asked to void before weight and body composition are measured.

Whenever possible, weight and body composition should not be measured during bouts of severe diarrhoea or other obvious disturbances of hydration status.

Subjects should not engage in strenuous exercise for 8 hours preceding the measurements because of its potential effect on hydration status.

Height:

This measure should be carefully performed using a standiometer, a measuring rod often found attached to scales, or other device that is carefully mounted and maintained throughout the study. If no designated equipment is available for measuring height, a tape measure or series of yardsticks should be carefully attached to a wall, with a zero end just touching the floor.

Shoes should be removed before height is measured.

For wall-mounted measuring devices, the subject should stand facing away from the device. They should be aligned so that the device runs up the middle of the body and standing with heels together and heels, buttocks and shoulders touching the wall. The subject should stand as straight as possible with chin resting on chest. Any horizontal measuring bar should be raised above the subject's head and lowered until it just touches the head (the skull, not just the hair). It is important to make certain that the bar is completely horizontal. If the bar is at an

angle greater or less than 90 degrees to the wall, the measurement of the height will be inaccurate.

Appendix C - Adverse Events and Serious Adverse Events.

Definition of an adverse event (AE).

An AE is any untoward medical occurrence in a patient or investigation subject administered a pharmaceutical product and which does not necessarily have a causal relationship with this treatment or investigations occurring as part of the study protocol.

An AE includes:

Exacerbation or increase in frequency or severity of a pre-existing illness.

Diagnosis of a condition occurring after administration of study drug, even if the subject may have experienced an episode in the past, occurring prior to the start of the study.

Persistent symptoms, present at baseline, that intensify after the start of the study.

An AE does not include:

Medical or surgical procedure (although a condition leading to surgical intervention may be an AE).

Pre-existing conditions that do not worsen after the start of the study.

Hospital admissions not related to an untoward medical occurrence (eg cosmetic surgery).

Definition of a Serious Adverse Event (SAE).

A SAE is any adverse event occurring at any dose that results in any of the following outcomes:

Death.

A life threatening adverse event.

Inpatient hospitalisation or prolongation of existing hospitalisation.

A disability/incapacity.

A congenital anomaly in the offspring of a subject who received drug.

Important medical events that may not result in death, be life threatening, or require hospitalisation may be considered a SAE when, based upon appropriate medical judgement, they may jeopardise the patient or subject and may require medical or surgical intervention to prevent one of the outcomes listed in this definition.

Abnormal Laboratory Assessments:

Abnormal laboratory assessments (including all scanning procedures) determined by the investigator as clinically significant, must be recorded as AEs or SAEs as defined in the above definitions. The investigator should exercise his/her medical and scientific judgement in deciding whether an abnormal laboratory finding or other abnormal assessment is clinically significant.

Appendix D - Declaration of Helsinki

52nd WMA General Assembly, Edinburgh, Scotland, October 2000

Ethical Principles for Medical Research Involving Human Subjects

HUMAN EXPERIMENTATION

In 1964, the World Medical Association drew up a code of ethics on human experimentation. This code, known as the Declaration of Helsinki, adopted by the 18th WMA General Assembly, Helsinki, Finland, June 1964 and amended by the 29th WMA General Assembly, Tokyo, Japan, October 1975, the 35th WMA General Assembly, Venice, Italy, October 1983, the 41st WMA General Assembly, Hong Kong, September 1989, the 48th WMA General Assembly, Somerset West, Republic of South Africa, October 1996 and the 52nd WMA General Assembly, Edinburgh, Scotland, October 2000 reads:

A. Introduction

(1) The World Medical Association has developed the Declaration of Helsinki as a statement of ethical principles to provide guidance to physicians and other participants in medical research involving human subjects. Medical research involving human subjects includes research on identifiable human material or identifiable data.

(2) It is the duty of the physician to promote and safeguard the health of the people. The physician's knowledge and conscience are dedicated to the fulfillment of this duty.

(3) The Declaration of Geneva of the World Medical Association binds the physician with the words, "The health of my patient will be my first consideration," and the International Code of Medical Ethics declares that, "A physician shall act only in the patient's interest when providing medical care which might have the effect of weakening the physical and mental condition of the patient."

(4) Medical progress is based on research which ultimately must rest in part on experimentation involving human subjects.

(5) In medical research on human subjects, considerations related to the well-being of the human subject should take precedence over the interests of science and society.

(6) The primary purpose of medical research involving human subjects is to improve prophylactic, diagnostic and therapeutic procedures and the understanding of the aetiology and pathogenesis of disease. Even the best proven prophylactic, diagnostic, and therapeutic methods must continuously be challenged through research for their effectiveness, efficiency, accessibility and quality.

(7) In current medical practice and in medical research, most prophylactic, diagnostic and therapeutic procedures involve risks and burdens.

(8) Medical research is subject to ethical standards that promote respect for all human beings and protect their health and rights. Some research populations are vulnerable and need special protection. The particular needs of the economically and medically disadvantaged must be recognized. Special attention is also required for those who cannot give or refuse consent for themselves, for those who may be subject to giving consent under duress, for those who will not benefit personally from the research and for those for whom the research is combined with care.

(9) Research Investigators should be aware of the ethical, legal and regulatory requirements for research on human subjects in their own countries as well as applicable international requirements. No national ethical, legal or regulatory requirement should be allowed to reduce or eliminate any of the protections for human subjects set forth in this Declaration.

B. Basic principles for all medical research

(10) It is the duty of the physician in medical research to protect the life, health, privacy, and dignity of the human subject.

(11) Medical research involving human subjects must conform to generally accepted scientific principles, be based on a thorough knowledge of the scientific

literature, other relevant sources of information, and on adequate laboratory and, where appropriate, animal experimentation.

(12) Appropriate caution must be exercised in the conduct of research which may affect the environment, and the welfare of animals used for research must be respected.

(13) The design and performance of each experimental procedure involving human subjects should be clearly formulated in an experimental protocol. This protocol should be submitted for consideration, comment, guidance, and where appropriate, approval to a specially appointed ethical review committee, which must be independent of the investigator, the sponsor or any other kind of undue influence. This independent committee should be in conformity with the laws and regulations of the country in which the research experiment is performed. The committee has the right to monitor ongoing trials. The researcher has the obligation to provide monitoring information to the committee, especially any serious adverse events. The researcher should also submit to the committee, for review, information regarding funding, sponsors, institutional affiliations, other potential conflicts of interest and incentives for subjects.

(14) The research protocol should always contain a statement of the ethical considerations involved and should indicate that there is compliance with the principles enunciated in this Declaration.

(15) Medical research involving human subjects should be conducted only by scientifically qualified persons and under the supervision of a clinically competent medical person. The responsibility for the human subject must always rest with a medically qualified person and never rest on the subject of the research, even though the subject has given consent.

(16) Every medical research project involving human subjects should be preceded by careful assessment of predictable risks and burdens in comparison with foreseeable benefits to the subject or to others. This does not preclude the participation of healthy volunteers in medical research. The design of all studies should be publicly available.

(17) Physicians should abstain from engaging in research projects involving human subjects unless they are confident that the risks involved have been adequately assessed and can be satisfactorily managed. Physicians should cease any investigation if the risks are found to outweigh the potential benefits or if there is conclusive proof of positive and beneficial results.

(18) Medical research involving human subjects should only be conducted if the importance of the objective outweighs the inherent risks and burdens to the subject. This is especially important when the human subjects are healthy volunteers.

(19) Medical research is only justified if there is a reasonable likelihood that the populations in which the research is carried out stand to benefit from the results of the research.

(20) The subjects must be volunteers and informed participants in the research project.

(21) The right of research subjects to safeguard their integrity must always be respected. Every precaution should be taken to respect the privacy of the subject, the confidentiality of the patient's information and to minimize the impact of the study on the subject's physical and mental integrity and on the personality of the subject.

(22) In any research on human beings, each potential subject must be adequately informed of the aims, methods, sources of funding, any possible conflicts of interest, institutional affiliations of the researcher, the anticipated benefits and potential risks of the study and the discomfort it may entail. The subject should be informed of the right to abstain from participation in the study or to withdraw consent to participate at any time without reprisal. After ensuring that the subject

has understood the information, the physician should then obtain the subject's freely-given informed consent, preferably in writing. If the consent cannot be obtained in writing, the non-written consent must be formally documented and witnessed.

(23) When obtaining informed consent for the research project the physician should be particularly cautious if the subject is in a dependent relationship with the physician or may consent under duress. In that case the informed consent should be obtained by a well-informed physician who is not engaged in the investigation and who is completely independent of this relationship.

(24) For a research subject who is legally incompetent, physically or mentally incapable of giving consent or is a legally incompetent minor, the investigator must obtain informed consent from the legally authorized representative in accordance with applicable law. These groups should not be included in research unless the research is necessary to promote the health of the population represented and this research cannot instead be performed on legally competent persons.

(25) When a subject deemed legally incompetent, such as a minor child, is able to give assent to decisions about participation in research, the investigator must obtain that assent in addition to the consent of the legally authorized representative.

(26) Research on individuals from whom it is not possible to obtain consent, including proxy or advance consent, should be done only if the physical/mental condition that prevents obtaining informed consent is a necessary characteristic of the research population. The specific reasons for involving research subjects with a condition that renders them unable to give informed consent should be stated in the experimental protocol for consideration and approval of the review committee. The protocol should state that consent to remain in the research should be obtained as soon as possible from the individual or a legally authorized surrogate.

(27) Both authors and publishers have ethical obligations. In publication of the results of research, the investigators are obliged to preserve the accuracy of the results. Negative as well as positive results should be published or otherwise publicly available. Sources of funding, institutional affiliations and any possible conflicts of interest should be declared in the publication. Reports of experimentation not in accordance with the principles laid down in this Declaration should not be accepted for publication.

C. Medical research combined with professional care (clinical research)

(28) The physician may combine medical research with medical care, only to the extent that the research is justified by its potential prophylactic, diagnostic or therapeutic value. When medical research is combined with medical care, additional standards apply to protect the patients who are research subjects.

(29) The benefits, risks, burdens and effectiveness of a new method should be tested against those of the best current prophylactic, diagnostic, and therapeutic methods. This does not exclude the use of placebo, or no treatment, in studies where no proven prophylactic, diagnostic or therapeutic method exists.

(30) At the conclusion of the study, every patient entered into the study should be assured of access to the best proven prophylactic, diagnostic and therapeutic methods identified by the study.

(31) The physician should fully inform the patient which aspects of the care are related to the research. The refusal of a patient to participate in a study must never interfere with the patient-physician relationship.

(32) In the treatment of a patient, where proven prophylactic, diagnostic and therapeutic methods do not exist or have been ineffective, the physician, with informed consent from the patient, must be free to use unproven or new prophylactic, diagnostic and therapeutic measures, if in the physician's judgement it offers hope of saving life, re-establishing health or alleviating suffering. Where possible, these measures should be made the object of research, designed to

evaluate their safety and efficacy. In all cases, new information should be recorded and, where appropriate, published. The other relevant guidelines of this Declaration should be followed.

9.2 Appendix B

Code	Region	Tissue (%Fat)	Region (%Fat)	Tissue (g)	Fat (g)	Lean (g)	BMC (g)	Total Mass (kg)
BH0001	Left Arm	31.9	30.6	3974	1267	2707	164	4.1
	Left Leg	47.7	46.4	18401	8785	9616	534	18.9
	Left Trunk	46	45.1	23383	10747	12636	428	23.8
	Left Total	44.2	42.9	48125	21278	26847	1457	49.6
	Right Arm	31.9	30.6	3974	1267	2707	164	4.1
	Right Leg	47.9	46.4	17156	8219	8937	551	17.7
	Right Trunk	46	45.2	23772	10940	12831	418	24.2
	Right Total	44.2	42.9	47245	20899	26345	1479	48.7
	Arms	31.9	30.6	7948	2534	5413	329	8.3
	Legs	47.8	46.4	35557	17004	18553	1085	36.6
	Trunk	46	45.2	47154	21688	25467	846	48
	Android	51.9	51.5	7784	4041	3743	61	7.8
	Gynoid	51.1	50.3	14763	7547	7216	253	15
	Total	44.2	42.9	95369	42177	53192	2936	98.3

Trunk / Total	Legs / Total	(Arms + Legs) / Total
0.51	0.4	0.9

Code	Region	Tissue (%Fat)	Region (%Fat)	Tissue (g)	Fat (g)	Lean (g)	BMC (g)	Total Mass (kg)
BH0002	Left Arm	40.7	39	3062	1245	1816	130	3.2
	Left Leg	59.2	57.1	15029	8904	6126	553	15.6
	Left Trunk	58.7	57	20081	11784	8297	601	20.7
	Left Total	56	53.9	40207	22515	17693	1598	41.8
	Right	40.7	39	3240	1317	1923	140	3.4

Arm								
Right Leg	59.2	57.1	15264	9041	6222	569	15.8	
Right Trunk	58.7	56.9	19876	11666	8210	614	20.5	
Right Total	56.1	54	40103	22516	17587	1617	41.7	
Arms	40.7	39	6402	2563	3739	279	6.6	
Legs	59.2	57.1	30293	17945	12348	1122	31.4	
Trunk	58.7	57	39957	23450	16507	1214	41.2	
Android	59.9	59.2	6298	3773	2525	75	6.4	
Gynoid	63.3	62.2	16282	10310	5972	295	16.6	
Total	56.1	53.9	80311	45031	35280	3214	83.5	

Trunk / Total	**Legs / Total**	**(Arms + Legs) / Total**	
0.52	0.4	0.87	

Code	Region	Tissue (%Fat)	Region (%Fat)	Tissue (g)	Fat (g)	Lean (g)	BMC (g)	Total Mass (kg)	
BH0003	**Left Arm**	23.1	22.2	4895	1130	3764	195	5.1	
	Left Leg	23.5	22.6	13501	3177	10324	537	14	
	Left Trunk	39.7	38.8	24905	9891	15014	577	25.5	
	Left Total	31.9	30.8	45919	14631	31288	1576	47.5	
	Right Arm	23.1	22.2	4895	1130	3764	195	5.1	
	Right Leg	23.6	22.6	13912	3279	10633	583	14.5	
	Right Trunk	39.7	38.7	24489	9728	14761	621	25.1	
	Right Total	31.7	30.6	45911	14568	31343	1639	47.6	
	Arms	23.1	22.2	9728	2261	7529	391	10.2	
	Legs	23.5	22.6	27413	6456	20957	1120	28.5	
	Trunk	39.7	38.8	49394	19619	29774	1198	50.6	
	Android	46.2	45.9	8037	3712	4325	55	8.1	
	Gynoid	29.3	28.6	13010	3815	9195	339	13.3	
	Total	31.8	30.7	91830	29199	62631	3215	95	

Trunk /	**Legs /**	**(Arms +**

							Total	Total	Legs) / Total
							0.67	0.22	0.44

Code	Region	Tissue (%Fat)	Region (%Fat)	Tissue (g)	Fat (g)	Lean (g)	BMC (g)	Total Mass (kg)	
BH0004	Left Arm	42.9	41.5	4220	1812	2408	142	4.4	
	Left Leg	52.3	50.7	17065	8929	8136	531	17.6	
	Left Trunk	49.6	48.9	25066	12443	12622	400	25.5	
	Left Total	49.1	47.8	48005	23576	24429	1271	49.3	
	Right Arm	42.9	41.5	4220	1812	2408	142	4.4	
	Right Leg	52.3	50.7	17065	8929	8136	531	17.6	
	Right Trunk	49.6	48.9	24911	12367	12544	361	25.3	
	Right Total	48.6	47.3	48781	23718	25063	1372	50.2	
	Arms	42.9	41.5	8441	3624	4816	284	8.7	
	Legs	52.3	50.7	34129	17858	16271	1061	35.2	
	Trunk	49.6	48.9	49977	24810	25167	760	50.7	
	Android	55.7	55.4	8891	4948	3943	39	8.9	
	Gynoid	55.8	54.7	15559	8681	6877	303	15.9	
	Total	48.9	47.6	96785	47294	49492	2643	99.4	

							Trunk / Total	Legs / Total	(Arms + Legs) / Total
							0.52	0.38	0.87

Code	Region	Tissue (%Fat)	Region (%Fat)	Tissue (g)	Fat (g)	Lean (g)	BMC (g)	Total Mass (kg)	
BHR007	Left Arm	28.9	27.7	3666	1058	2608	159	3.8	
	Left Leg	9	8.6	9776	878	8898	495	10.3	
	Left Trunk	35.5	34.5	23789	8337	15451	400	24.2	

	Left Total	26.6	25.8	39854	10602	29252	1301	41.2
	Right Arm	28.9	27.7	4199	1212	2987	179	4.4
	Right Leg	9	8.6	9330	841	8489	495	9.8
	Right Trunk	35	34.4	22540	7892	14648	381	22.9
	Right Total	26.7	25.8	38356	10236	28120	1266	39.6
	Arms	28.9	27.7	7865	2270	5595	338	8.2
	Legs	9	8.6	19106	1719	17397	990	20.1
	Trunk	35	34.5	46328	16229	30099	781	47.1
	Android	44.3	43.9	7865	3211	4039	57	7.3
	Gynoid	13.9	13.5	10037	1399	8639	287	10.3
	Total	26.6	25.8	78210	20838	57373	2567	80

Trunk / Total	**Legs / Total**	**(Arms + Legs) / Total**
0.78	0.08	0.25

Code	**Region**	**Tissue (%Fat)**	**Region (%Fat)**	**Tissue (g)**	**Fat (g)**	**Lean (g)**	**BMC (g)**	**Total Mass (kg)**
BHR008	**Left Arm**	48.7	46.4	3632	1768	1864	175	3.8
	Left Leg	59.5	57.2	14025	8349	5677	577	14.6
	Left Trunk	56	54.3	19695	11026	8669	619	20.3
	Left Total	55.3	53.1	39092	21626	17466	1597	40.7
	Right Arm	48.7	46.4	3961	1928	2033	194	4.2
	Right Leg	59.5	57.2	14150	8242	5726	573	14.7
	Right Trunk	55.9	54.3	18956	10602	8354	560	19.5
	Right Total	54.8	52.5	39460	21620	17840	1685	41.1
	Arms	48.7	46.4	7593	3969	3897	369	8
	Legs	59.5	57.2	28176	16773	11402	1150	29.3
	Trunk	56	54.3	38652	21629	17023	1179	39.8
	Android	56.6	55.9	5183	2935	2248	70	5.3
	Gynoid	62.6	61.3	14238	8915	5323	314	14.6

	Total	55.1	52.8	78552	43246	35306	3283	81.8	
						Trunk / Total	**Legs / Total**	**(Arms + Legs) / Total**	
						0.5	0.39	0.95	

Code	Region	Tissue (%Fat)	Region (%Fat)	Tissue (g)	Fat (g)	Lean (g)	BMC (g)	Total Mass (kg)	
BHR009	**Left Arm**	28.8	27.4	3528	1016	2512	177	3.7	
	Left Leg	29.2	27.9	10615	3096	7519	476	11.1	
	Left Trunk	45.2	44.2	21887	9890	11997	498	22.4	
	Left Total	37.5	36.2	38668	14516	24151	1399	40.1	
	Right Arm	29.2	27.7	3216	938	2278	171	3.4	
	Right Leg	29.2	27.9	10523	3072	7452	480	11	
	Right Trunk	45.2	44.2	21845	9872	11972	504	22.3	
	Right Total	37.9	36.6	37786	14311	23476	1357	39.1	
	Arms	29	27.6	6744	1954	4790	348	7.1	
	Legs	29.2	27.9	21138	6167	14971	956	22.1	
	Trunk	45.2	44.2	43732	19762	23970	1003	44.7	
	Android	51.8	51.4	6959	3606	3353	54	7	
	Gynoid	37.6	36.6	10799	4062	6737	304	11.1	
	Total	37.7	36.4	76454	28827	47627	2756	79.2	
						Trunk / Total	**Legs / Total**	**(Arms + Legs) / Total**	
						0.69	0.21	0.41	

Code	Region	Tissue (%Fat)	Region (%Fat)	Tissue (g)	Fat (g)	Lean (g)	BMC (g)	Total Mass (kg)	
BHC001A	**Left Arm**	22.9	21.7	3480	797	2682	199	3.7	
	Left Leg	41.6	39.9	13202	5495	7707	583	13.8	

	Left Trunk	36.7	35.3	15771	5783	9988	628	16.4
	Left Total	36.2	34.5	34375	12431	21944	1665	36
	Right Arm	22.7	21.4	3481	790	2691	203	3.7
	Right Leg	41.7	39.9	13463	5610	7853	604	14.1
	Right Trunk	36.6	35.3	14939	5473	9467	566	15.5
	Right Total	36	34.3	34197	12301	21896	1660	35.9
	Arms	22.8	21.6	6961	1588	5373	402	7.4
	Legs	41.6	39.9	26665	11105	15560	1187	27.9
	Trunk	36.7	35.3	30711	11256	19455	1194	31.9
	Android	32.5	31.9	4052	1316	2735	81	4.1
	Gynoid	45.8	44.6	10316	4725	5591	285	10.6
	Total	36.1	34.4	68572	24732	43840	3325	71.9

Trunk / Total	**Legs / Total**	**(Arms + Legs) / Total**
0.46	0.45	1.13

Code	**Region**	**Tissue (%Fat)**	**Region (%Fat)**	**Tissue (g)**	**Fat (g)**	**Lean (g)**	**BMC (g)**	**Total Mass (kg)**
BHC002A	**Left Arm**	36.2	34.7	4327	1568	2759	190	4.5
	Left Leg	44.8	43	11638	5210	6428	487	12.1
	Left Trunk	45.5	44.3	16166	7347	8818	416	16.6
	Left Total	42.5	40.9	34372	14615	19757	1339	35.7
	Right Arm	36.1	34.5	3931	1419	2511	187	4.1
	Right Leg	44.8	43	11894	5330	6564	514	12.4
	Right Trunk	45.6	44.3	16385	7470	8915	458	16.8
	Right Total	42.6	40.9	34563	14723	19840	1421	36
	Arms	36.2	34.6	8257	2987	5270	377	8.6
	Legs	44.8	43	23533	10540	12992	1001	24.5
	Trunk	45.5	44.3	32550	14817	17733	874	33.4

	Android	49.7	49.1	5142	2554	2588	58	5.2	
	Gynoid	48.8	47.6	9564	4664	4900	225	9.8	
	Total	42.6	40.9	68935	29338	39597	2760	71.7	
						Trunk / Total	**Legs / Total**	**(Arms + Legs) / Total**	
						0.51	0.36	0.91	

9.3 Appendix C

Code	Region	Tissue (%Fat)	Region (%Fat)	Tissue (g)	Fat (g)	Lean (g)	Total Mass (kg)	
BH0001	**Left Arm**	39.3	12.33	3332	1309	2021	3.3	
	Left Leg	47.8	13.582	20524	9815	9815	20.52	
	Left Trunk	51.6	34.75	22669	11692	10976	22.66	
	Left Total	46.2	19.57	46526	22817	23708	23.7	
	Right Arm	43.2	12.97	4169	1802	2368	4.17	
	Right Leg	48.5	13.28	21071	10228	10842	21.07	
	Right Trunk	58.3	41.33	23632	13795	9836	23.63	
	Right Total	50.03	20.78	48873	25825	23048	48.87	
	Arms	41.46	12.7	7502	3110	4391	7.5	
	Legs	48.18	13.4	41596	20044	21551	41.59	
	Trunk	55.04	38.02	46301	25487	20813	46.3	
	Anterior Trunk	56.2	30.73	19353	10299	9054	19.35	
	Posterior Trunk	56.4	45.31	26947	15188	11759	26.94	
	Total	48.13	20.18	95399	48642	46757	95.4	
						Trunk / Total	**Legs / Total**	**(Arms + Legs) / Total**
						0.523	0.412	0.476

Code	Region	Tissue	Region	Tissue	Fat (g)	Lean (g)	Total

		(%Fat)	(%Fat)	(g)			Mass (kg)	
BH0002	**Left Arm**	52.61	21.1	2766	1455.193	1310.807	2.76	
	Left Leg	52.84	22.27	17731	9369.06	8361.94	17.73	
	Left Trunk	49.4	32.79	19114	9442.316	9671.684	19.115	
	Left Total	51.62	25.23	39612	20447.71	19164.29	24.097	
	Right Arm	49.56	20.07	2696	1336.138	1359.862	2.69	
	Right Leg	55.2	22.62	17994	9932.688	8061.312	17.99	
	Right Trunk	57.08	37.98	20196	11527.88	8668.123	20.196	
	Right Total	53.91	26.82	40887	22042.18	18844.82	40.887	
	Arms	51.11	20.61	5463	2792.139	2670.861	5.46	
	Legs	53.98	22.45	35725	19284.36	16440.65	35.72	
	Trunk	53.35	35.377	39311	20972.42	18338.58	39.311	
	Anterior Trunk	57.66	35.91	18671	10765.7	7905.301	18.67	
	Posterior Trunk	49.44	34.81	20639	10203.92	10435.08	20.63	
	Total	52.76	26.02	80499	42471.27	38027.73	80.5	
						Trunk / Total	**Legs / Total**	**(Arms + Legs) / Total**
						0.49	0.45	0.52

Code	Region	Tissue (%Fat)	Region (%Fat)	Tissue (g)	Fat (g)	Lean (g)	Total Mass (kg)	
BH0003	**Left Arm**	52.36	14.9	4164	2180	1983	4.16	
	Left Leg	36.26	11.24	18494	6707	11787	18.49	
	Left Trunk	57.44	40.28	23334	13405	9928	23.33	
	Left Total	48.69	20.83	45993	22293	23699	23.69	
	Right Arm	42.46	11.75	4129	1753	2375	4.12	
	Right Leg	37.32	9.98	18150	6774	11376	18.15	
	Right Trunk	56.3	41.5	24726	13922	10803	24.72	

	Right Total	45.36	19.3	47006	22450	24555	47	
	Arms	47.43	13.31	8294	3934	4359	8.29	
	Legs	36.79	10.57	36645	13481	23163	36.64	
	Trunk	56.86	41.24	48060	27328	20732	48.06	
	Anterior Trunk	57.9	40.66	23267	13472	9795	23.36	
	Posterior Trunk	55.88	41.84	24792	13855	10936	24.79	
	Total	47.03	20.07	93000	44744	48255	93	
						Trunk / Total	**Legs / Total**	**(Arms + Legs) / Total**
						0.61	0.301	0.39

Code	**Region**	**Tissue (%Fat)**	**Region (%Fat)**	**Tissue (g)**	**Fat (g)**	**Lean (g)**	**Total Mass (kg)**	
BH0004	**Left Arm**	53.9	15.38	3653	1969	1684	3.65	
	Left Leg	50.95	15.32	24848	12662	12186	24.84	
	Left Trunk	52.7	34.69	20952	11043	9908	20.95	
	Left Total	52.52	20.17	49454	25675	23779	23.77	
	Right Arm	56.22	14.61	3399	1911	1487	3.39	
	Right Leg	56.13	17.58	24578	13797	10780	24.57	
	Right Trunk	48.45	31.53	21767	10547	11220	21.76	
	Right Total	53.6	21	49745	26256	23488	49.74	
	Arms	55.02	14.99	7052	3880	3171	7.05	
	Legs	53.53	16.42	49427	26460	22967	49.42	
	Trunk	50.54	33.076	42720	21590	21129	42.72	
	Anterior Trunk	46.67	28.43	20392	9517	10875	20.39	
	Posterior Trunk	54.07	37.96	22327	12073	10253	22.32	
	Total	53.06	20.59	99200	51931	47268	99.2	
						Trunk / Total	**Legs / Total**	**(Arms + Legs) /**

								Total
						0.41	0.5	0.58

Code	Region	Tissue (%Fat)	Region (%Fat)	Tissue (g)	Fat (g)	Lean (g)	Total Mass (kg)	
BHR008	**Left Arm**	47.447	21.67	5333	2530.349	2802.651	5.33	
	Left Leg	51.29	19.31	19439	9970.263	9468.737	19.43	
	Left Trunk	58.95	43	16699	9844.061	6854.94	16.69	
	Left Total	52.56	25.07	41472	21797.68	19674.32	21.61	
	Right Arm	50.81	23.49	5421	2754.41	2666.59	5.42	
	Right Leg	55.78	20.15	18800	10486.64	8313.36	18.8	
	Right Trunk	58.41	41.55	16205	9465.341	6739.66	16.2	
	Right Total	55	25.51	40427	22234.85	18192.15	40.42	
	Arms	49.14	22.58	10755	5285.007	5469.993	10.75	
	Legs	53.5	19.73	38240	20458.4	17781.6	38.24	
	Trunk	58.69	42.29	32904	19311.36	13592.64	32.9	
	Anterior Trunk	62.64	42.18	15258	9557.611	5700.389	15.25	
	Posterior Trunk	55.27	42.39	17646	9752.944	7893.056	17.64	
	Total	53.78	25.29	81899	44045.28	37853.72	81.9	
						Trunk / Total	**Legs / Total**	**(Arms + Legs) / Total**
						0.43	0.45	0.57

Code	Region	Tissue (%Fat)	Region (%Fat)	Tissue (g)	Fat (g)	Lean (g)	Total Mass (kg)	
BHR009	**Left Arm**	33.39	8.63	3207	1071	2136	3.2	
	Left Leg	42.82	9.46	15809	6770	9039	15.8	
	Left Trunk	54.09	32.64	19144	10356	8788	19.14	
	Left	43.43	15.73	38161	18197	19964	19.96	

	Total							
	Right Arm	31.99	9.3	4399	1407	2991	4.39	
	Right Leg	47.02	10.14	16013	7530	8483	16.01	
	Right Trunk	56.2	35.87	20425	11479	8945	20.42	
	Right Total	45.07	16.82	40838	20417	20420	40.83	
	Arms	32.58	9	7606	2478	5128	7.6	
	Legs	44.93	9.81	31822	14300	17522	31.82	
	Trunk	55.18	34.26	39570	21835	17734	39.57	
	Anterior Trunk	52.1	29.52	18054	9407	8647	18.05	
	Posterior Trunk	57.76	39.01	21515	12428	9087	21.51	
	Total	44.25	16.27	78990	38615	40384	79	
						Trunk / Total	**Legs / Total**	**(Arms + Legs) / Total**
						0.57	0.37	0.43

Code	**Region**	**Tissue (%Fat)**	**Region (%Fat)**	**Tissue (g)**	**Fat (g)**	**Lean (g)**	**Total Mass (kg)**	
BHC001A	**Left Arm**	35.11	10.9	4062	1426	2636	4.06	
	Left Leg	42.6	12.88	18198	7752	10445	18.19	
	Left Trunk	47.36	27.19	12731	6030	6701	12.73	
	Left Total	41.69	15.94	34992	15209	19782	19.78	
	Right Arm	32.31	9.8	3496	1130	2366	3.49	
	Right Leg	47.81	13.61	18616	8902	9714	18.61	
	Right Trunk	47.92	29.76	13894	6659	7234	13.89	
	Right Total	42.68	16.84	36007	16681	19315	36	
	Arms	33.81	10.41	7559	2556	5003	7.55	
	Legs	45.24	13.26	36814	16654	20159	36.81	
	Trunk	47.65	28.48	26626	12689	13936	26.62	
	Anterior Trunk	49.39	28.35	12788	6316	6472	12.78	

	Posterior Trunk	46.05	28.61	13837	6373	7464	13.83	
	Total	42.19	16.38	70999	31901	39098	71	
						Trunk / Total	**Legs / Total**	**(Arms + Legs) / Total**
						0.4	0.52	0.6
Code	**Region**	**Tissue (%Fat)**	**Region (%Fat)**	**Tissue (g)**	**Fat (g)**	**Lean (g)**	**Total Mass (kg)**	
BHC002A	**Left Arm**	42.17	12.81	3730	1573	2157	3.73	
	Left Leg	44.43	12.19	16108	7158	8950	16.1	
	Left Trunk	51.55	36.05	16458	8484	7973	16.45	
	Left Total	46.05	18.21	36297	17216	19081	19.08	
	Right Arm	39.42	12.32	4503	1775	2728	4.5	
	Right Leg	48.25	13.16	15349	7407	7942	15.34	
	Right Trunk	55.97	37.16	15249	8535	6713	15.24	
	Right Total	47.88	19.02	35102	17718	17384	35.1	
	Arms	40.67	12.55	8234	3348	4885	8.23	
	Legs	46.3	12.67	31458	14565	16892	31.45	
	Trunk	53.67	36.99	31707	17020	14687	31.7	
	Anterior Trunk	53.93	33.41	14245	7685	6560	14.24	
	Posterior Trunk	53.45	40.57	17461	9334	8127	17.46	
	Total	46.97	18.62	71400	34934	36465	71.4	
						Trunk / Total	**Legs / Total**	**(Arms + Legs) / Total**
						0.49	0.42	0.51

9.4 Appendix D

FN	Rater 1	Rater 2	Rater 3	Rater 4	Rater 5	Rater 6	Rater 7

Image 1	1	1	1	2	2	2	2
Image 2	1	1	2	2	1	2	1
Image 3	2	2	1	2	2	2	1
Image 4	2	1	1	2	1	2	2
Image 5	1	1	1	2	2	2	2
Image 6	1	2	1	2	2	2	2
Image 7	1	1	2	1	1	2	2
Image 8	1	1	2	1	2	2	1
Image 9	2	2	1	1	1	2	1
Image 10	1	1	1	1	1	2	1
Image 11	1	1	1	1	2	2	1

FP	**Rater 1**	**Rater 2**	**Rater 3**	**Rater 4**	**Rater 5**	**Rater 6**	**Rater 7**
Image 1	2	1	2	1	2	1	1
Image 2	2	2	2	1	1	2	1
Image 3	1	2	1	1	2	1	1

Image 4	1	2	2	1	1	2	1
Image 5	1	1	2	2	2	2	1
Image 6	1	1	2	2	1	1	1
Image 7	1	1	2	2	2	1	1
Image 8	1	2	2	2	2	1	1
Image 9	1	2	1	2	2	2	1
Image 10	1	2	2	2	2	1	2
Image 11	2	1	2	2	2	2	2

TP	Rater 1	Rater 2	Rater 3	Rater 4	Rater 5	Rater 6	Rater 7
Image 1	4	4	4	4	5	4	4
Image 2	4	5	4	4	4	5	5
Image 3	4	4	5	4	4	4	5
Image 4	5	5	4	4	4	5	5
Image 5	5	4	4	4	5	4	5
Image 6	5	5	4	4	5	5	5

Image 7	5	5	4	4	4	5	5
Image 8	5	5	5	4	5	4	5
Image 9	5	5	5	4	5	4	5
Image 10	5	4	5	4	5	4	5
Image 11	5	4	4	4	5	4	5

10 References

1. Mauss, S., et al., *Risk factors for the HIV-associated lipodystrophy syndrome in a closed cohort of patients after 3 years of antiretroviral treatment.* HIV Medicine, 2002. **3**(1): p. 49-55.
2. Duran, S., et al., *Failure to maintain long-term adherence to highly active antiretroviral therapy: the role of lipodystrophy.* AIDS, 2001. **15**(18): p. 2441-2444.
3. DeVita, M.V. and S.H. Stall, *Dual-energy X-ray absorptiometry: A review.* Journal of Renal Nutrition, 1999. **9**(4): p. 178-181.
4. UNAIDS, *Report on the global HIV/AIDS epidemic*, 2008, Joint United Nations Programme on HIV/AIDS
5. Martínez, E., et al., *Incidence and causes of death in HIV-infected persons receiving highly active antiretroviral therapy compared with estimates for the general population of similar age and from the same geographical area.* HIV Medicine, 2007. **8**(4): p. 251-258.
6. Montaner, J.S.G., et al., *Antiretroviral treatment in 1998.* The Lancet, 1998. **352**(9144): p. 1919-1922.
7. Carpenter, C.C.J., et al., *Antiretroviral Therapy for HIV Infection in 1998.* JAMA: The Journal of the American Medical Association, 1998. **280**(1): p. 78-86.
8. Palmer, C., *HIV treatments and highly active antiretroviral therapy.* Australian Prescriber, 2003. **26**(3): p. 59-61.
9. Administration, F.a.D., *Protease inhibitors may increase blood glucose in HIV patients.* FDA, 1997. **27**(2).
10. Mallon, P.W.G., D.A. Cooper, and A. Carr, *HIV-associated lipodystrophy.* HIV Medicine, 2001. **2**(3): p. 166-173.
11. Carr, A., *Toxicity of antiretroviral therapy and implications for drug development.* Nature Reviews Drug Discovery, 2003. **2**(8): p. 624-634.
12. Shevitz, A., et al., *Clinical perspectives on HIV-associated lipodystrophy syndrome: an update.* AIDS, 2001. **15**(15): p. 1917-1930.
13. Walli, R., et al., *Treatment with protease inhibitors associated with peripheral insulin resistance and impaired oral glucose tolerance in HIV-1-infected patients.* AIDS, 1998. **12**(15): p. F167-F173.
14. Lindegaard, B., et al., *Adipose tissue expression of IL-18 and HIV-associated lipodystrophy.* AIDS, 2004. **18**(14): p. 1956-1958.
15. NCBI. *PubMed Central*. 2011 [cited 2011 21/11/2011]; Available from: http://www.ncbi.nlm.nih.gov/pubmed/.
16. Scherzer, R., et al., *Comparison of dual-energy X-ray absorptiometry and magnetic resonance imaging–measured adipose tissue depots in HIV-infected and control subjects.* The American Journal of Clinical Nutrition, 2008. **88**(4): p. 1088-1096.
17. Blake, G.M., M. Naeem, and M. Boutros, *Comparison of effective dose to children and adults from dual X-ray absorptiometry examinations.* Bone, 2006. **38**(6): p. 935-942.

18. Bezakova, E., P. Collins, and A. Beddoe, *Absorbed dose measurements in dual energy X-ray absorptiometry (DXA).* Br J Radiol, 1997. **70**(830): p. 172-179.

19. TOTHIL, P., *Dual-energy X-ray absorptiometry for the measurement of bone and soft tissue compositio*. Clinical Nutrition, 1995. **14**: p. 263-268.

20. Bernhard Preim, D.B., *Visualization in Medicine, Theory, Algorithms, and Applications*2007, Amsterdam: Morgan Kaufman Publishers. 677.

21. Mudry, K.M., *The Biomedical Engineering Handbook*. 2 ed, ed. J.D. Bronzino. Vol. 1. 2000: CRC Press LLC.

22. Friman, O., *Adaptive Analysis of Functional MRI Data*, in *Department of Biomedical Engineering*2003, Linköpings universitet: Linköping. p. 13-16.

23. Abate, N., et al., *Estimation of adipose tissue mass by magnetic resonance imaging: validation against dissection in human cadavers.* J. Lipid Res., 1994. **35**(8): p. 1490-1496.

24. Jin, Y., et al., *Segmentation and Evaluation of Adipose Tissue from Whole Body MRI Scans* Lecture Notes in Computer Science, 2003. **287**: p. 635-642.

25. Nowak, R.D., *Wavelet-based rician noise removal for magnetic resonance imaging Image Processing.* IEEE Transactions on, 1999. **8**(10): p. 1408-1419.

26. Vovk, U., F. Pernus, and B. Likar, *A Review of Methods for Correction of Intensity Inhomogeneity in MRI.* Medical Imaging, IEEE Transactions on, 2007. **26**(3): p. 405-421.

27. Hou, Z., *A Review on MR Image Intensity Inhomogeneity Correction.* International Journal of Biomedical Imaging, 2006. **2006**.

28. González Ballester, M.Á., A.P. Zisserman, and M. Brady, *Estimation of the partial volume effect in MRI.* Medical Image Analysis, 2002. **6**(4): p. 389-405.

29. Mark A. Brown, R.C.S., *MRI: Basic Principles and Applications*. 4 ed2010, New Jersey: Wiley-Blackwell.

30. Ross, R., *Magnetic resonance imaging provides new insights into the characterization of adipose and lean tissue distribution.* Canadian Journal of Physiology and Pharmacology, 1996. **74**(6): p. 778-785.

31. Ross, R., et al., *Quantification of adipose tissue by MRI: relationship with anthropometric variables.* Journal of Applied Physiology, 1992. **72**(2): p. 787-795.

32. Abate, N., et al., *Estimation of adipose tissue mass by magnetic resonance imaging: validation against dissection in human cadavers.* Journal of Lipid Research, 1994. **35**(8): p. 1490-6.

33. Pal, N.R. and S.K. Pal, *A review on image segmentation techniques.* Pattern Recognition, 1993. **26**(9): p. 1277-1294.

34. PK, S., S. S, and W. AKC, *A survey of thresholding techniques.* Comput. Vis. Graph. Image Proc., 1988. **41**: p. 233.

35. Pham, D.L., C. Xu, and J.L. Prince, *CURRENT METHODS IN MEDICAL IMAGE SEGMENTATION1.* Annual Review of Biomedical Engineering, 2000. **2**(1): p. 315-337.

36. Freixenet, J., et al., *Yet Another Survey on Image Segmentation: Region and Boundary Information Integration*

Computer Vision — ECCV 2002, A. Heyden, et al., Editors. 2002, Springer Berlin / Heidelberg. p. 21-25.

37. HR, S. and P. GM, *Automatic cardiac MR image segmentation using edge detection by tissue classification in pixel neighborhoods.* Magn. Reson. Med., 1997. **37**: p. 418.

38. GB, C. and A. HC, *Image segmentation by clustering.* Proc. IEEE, 1979. **5**: p. 773.

39. Saha, P.K., J.K. Udupa, and D. Odhner, *Scale-Based Fuzzy Connected Image Segmentation: Theory, Algorithms, and Validation.* Computer Vision and Image Understanding, 2000. **77**(2): p. 145-174.

40. William E. Lorensen, H.E.C., *Marching Cubes: A high resolution 3D surface construction algorithm.* Computer Graphics, 1987. **21**(4).

41. Gunnar Johansson, H.C., *Accelerating Marching Cubes with Graphics Hardware.* CASCON, 2006. **ix**(18).

42. Kaufman, A.M., K., ed. *Overview of Volume Rendering*. Visualization Handbook, ed. D.D.J. Hansen, C. R.2005, Butterworth-Heinemann: Burlington.

43. He, F.L., X., *A Rendering Method for Visualization of Medical Data*. Modern Applied Science, 2010. **4**(12): p. 126.

44. Wikipedia. *Volume Ray Casting*. 2006 [cited 2011 22/09/2011]; Available from: http://en.wikipedia.org/wiki/File:Volume_ray_casting.png.

45. Siemens. [cited 2011 19/11/2011]; Available from: http://www.medical.siemens.com/siemens/it_IT/gg_mr_FBAs/files/brochures/Symphony_with_Tim/MAGNETOM_Symphony_Tim_Coils.pdf.

46. Nokia. *QT*. [cited 2011 19/11/2011]; Available from: http://qt.nokia.com/.

47. NEMA. *DICOM*. 2011 [cited 2011 14/10/2011]; Available from: http://medical.nema.org/.

48. Medicine, U.N.L.o. *Insight Toolkit*. [cited 2011 14/11/2011]; Available from: http://www.itk.org/.

49. Garage, W. *OpenCV*. [cited 2011 10/11/2011]; Available from: http://opencv.willowgarage.com/wiki/Welcome.

50. Raju, R., et al. *File transfer speed-up by automatic thread assignment in FTP engine*. in *International Conference on Communication and Computational Intelligence*. 2010. Kongu Engineering College, Erode, India: IEEE.

51. Gispert, J.D., et al., *Method for bias field correction of brain T1-weighted magnetic resonance images minimizing segmentation error.* Human Brain Mapping, 2004. **22**(2): p. 133-144.

52. Lai, S.-H. and M. Fang, *A dual image approach for bias field correction in magnetic resonance imaging.* Magnetic Resonance Imaging, 2003. **21**(2): p. 121-125.

53. Zuiderveld, K., *Contrast limited adaptive histogram equalization*, in *Graphics gems IV*1994, Academic Press Professional, Inc. p. 474-485.

54. Reza, A.M., *Realization of the Contrast Limited Adaptive Histogram Equalization (CLAHE) for Real-Time Image Enhancement.* The Journal of VLSI Signal Processing, 2004. **38**(1): p. 35-44.

55. Wikipedia. *AHE Neighbourhoods*. 2011 [cited 2012 12/02/2012]; Available from: http://en.wikipedia.org/wiki/File:AHE-neighbourhoods.svg.

56. Wikipedia. *Clahe Redistribution*. 2011 [cited 2012 12/02/2012]; Available from: http://en.wikipedia.org/wiki/File:Clahe-redist.svg.

57. Peizhuang, W., *Pattern Recognition with Fuzzy Objective Function Algorithms (James C. Bezdek).* SIAM Review, 1983. **25**(3): p. 442.

58. Pal, N.R. and J.C. Bezdek, *On cluster validity for the fuzzy c-means model.* Fuzzy Systems, IEEE Transactions on, 1995. **3**(3): p. 370-379.

59. Chen, W., M.L. Giger, and U. Bick, *A Fuzzy C-Means (FCM)-Based Approach for Computerized Segmentation of Breast Lesions in Dynamic Contrast-Enhanced MR Images1*. Academic Radiology, 2006. **13**(1): p. 63-72.

60. Phillips Ii, W.E., et al., *Application of fuzzy c-means segmentation technique for tissue differentiation in MR images of a hemorrhagic glioblastoma multiforme.* Magnetic Resonance Imaging, 1995. **13**(2): p. 277-290.

61. Chuang, K.-S., et al., *Fuzzy c-means clustering with spatial information for image segmentation.* Computerized Medical Imaging and Graphics, 2006. **30**(1): p. 9-15.

62. Group, K. *OpenGL*. 2011 [cited 2011 22/12/2011]; Available from: http://www.opengl.org/.

63. Shoemake, K., *ARCBALL: a user interface for specifying three-dimensional orientation using a mouse*, in *Proceedings of the conference on Graphics interface '92*1992, Morgan Kaufmann Publishers Inc.: Vancouver, British Columbia, Canada. p. 151-156.

64. MedCalc. *MedCalc*. 2011 [cited 2011 21/11/2011]; Available from: http://www.medcalc.org/index.php.

65. Cohen, J., *Statistical power analysis for the behavioral sciences : Jacob Cohen*1988: Lawrence Erlbaum.

66. Bland, M.J. and D.G. Altman, *Statistical methods for assessing agreement between two methods of clinical measurement.* The Lancet, 1986. **327**(8476): p. 307-310.

67. Zhang, D.-Q. and S.-C. Chen, *A novel kernelized fuzzy C-means algorithm with application in medical image segmentation.* Artificial intelligence in medicine, 2004. **32**(1): p. 37-50.

68. Chuang, K.-S., et al., *Fuzzy c-means clustering with spatial information for image segmentation.* Computerized medical imaging and graphics : the official journal of the Computerized Medical Imaging Society, 2006. **30**(1): p. 9-15.